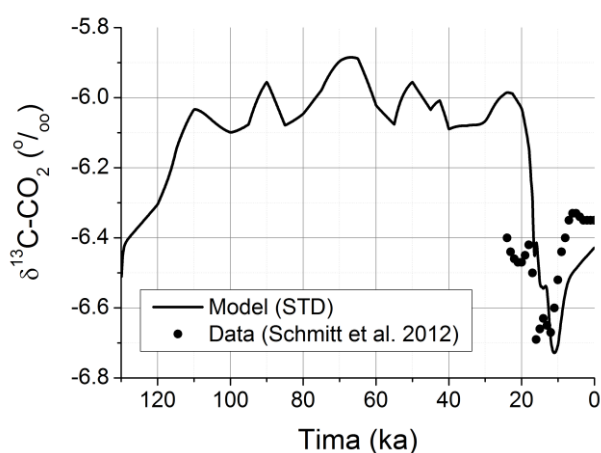


1 **Reply to the editor's comments**

2 We like to thank the editor for his very helpful and constructive comments. Our replies to
3 these comments are listed below.

4 **Atmospheric $\delta^{13}\text{C-CO}_2$**

5 The figure below, now added to our manuscript as Fig. A3, shows the atmospheric $\delta^{13}\text{C-CO}_2$
6 record as calculated in our standard simulation. According to this simulation and our previous
7 studies (Sarnthein et al., 2013), the strong negative $\delta^{13}\text{C}$ -excursion observed in the ice-core
8 record was largely caused by deglacial upwelling pulses in the Southern Ocean, though the
9 amplitude of the simulated $\delta^{13}\text{C-CO}_2$ decline is much larger than that observed in the dataset
10 (Schmitt et al., 2012).



11

12 *Stable carbon isotopic composition of atmospheric CO₂. Model results versus ice-core data*
13 *(Schmitt et al., 2012). The model results were obtained in the standard simulation STD*
14 *without any tuning of the ¹³C-CO₂ fluxes across the seawater-atmosphere interface.*

15 The trends of our results and the empiric data are similar. The different extent of shift of the
16 two records is probably related to the poor representation of the ¹³C-DIC turnover in the
17 Southern Ocean in our coarse-resolution model. We were not able to reproduce more closely
18 the observed $\delta^{13}\text{C-DIC}$ distribution in our model calibration even though a good fit was
19 attained for all other tracers (salinity, DIC, ¹⁴C-DIC, alkalinity, phosphate, nitrate, oxygen,
20 Fig. A1). Hence, we do not conclude that this deviation for $\delta^{13}\text{C-CO}_2$ implies erroneous
21 model results for all remaining model variables. It rather reflects a specific weakness in the
22 model set-up with respect to the simulation of $\delta^{13}\text{C-DIC}$ in the Southern Ocean. Our model
23 predicts a negative value for intermediate waters in the modern Southern Ocean ($\delta^{13}\text{C-DIC} = -$
24 0.05 ‰) while observations yield a positive value of $+0.72$ ‰ for this ocean box (SO₁ in
25 Tab. A2). Due to this deviation the vertical gradient in the model exceeds the observed $\delta^{13}\text{C}$
26 gradient between surface and intermediate waters by more than a factor of two. The glacial
27 rise and deglacial drop in $\delta^{13}\text{C-CO}_2$ are amplified by this model artefact. The deglacial
28 intermediate water, overly depleted in ¹³C, upwells into the surface ocean where it induces a

1 far too strong atmospheric $\delta^{13}\text{C-CO}_2$ decline. Since the biased vertical $\delta^{13}\text{C-DIC}$ gradient in
2 the Southern Ocean impedes a meaningful simulation of atmospheric $\delta^{13}\text{C-CO}_2$, we tuned the
3 $^{13}\text{C-CO}_2$ fluxes between the surface ocean and the atmosphere such that the resulting
4 atmospheric $\delta^{13}\text{C-CO}_2$ values were consistent with the ice-core record. By this way we
5 effectively employed the ice-core data to force the $\delta^{13}\text{C-DIC}$ model (Fig. 4f).

6 **Atmospheric radiocarbon**

7 It is largely unknown how the production rate of radiocarbon in the atmosphere has evolved
8 over the last glacial cycle (Fig. 12d). There are numerous conflicting proxy records (Frank et
9 al., 1997; Laj et al., 2002; Lal and Charles, 2007; Muscheler et al., 2005). None of them is
10 generally accepted (Köhler et al., 2006). In contrast, the proxy record of the standing stock of
11 ^{14}C in the atmosphere ($\Delta^{14}\text{C-CO}_2$, Fig. 12a) is relatively well constrained (Reimer et al.,
12 2013) even though some ambiguities remain (Sarnthein et al., 2015). Therefore, we employed
13 the $\Delta^{14}\text{C-CO}_2$ record to derive a record of the ^{14}C - production rate in the atmosphere. We
14 varied the production rate so long until the $\Delta^{14}\text{C-CO}_2$ values estimated by the model were
15 consistent with the proxy record. The resulting record of the ^{14}C production rate (Fig. 12c) can
16 be used to validate the model without invoking any form of circular reasoning. Our Holocene
17 record resembles the rates derived from the ^{10}Be ice-core record while the glacial part is
18 closer to the stacked sedimentary ^{10}Be record and one of the records derived from
19 geomagnetic data (compare Figs. 12c and 12d). New and more reliable proxy records of ^{14}C
20 production may become available over the coming years. They may be employed to
21 verify/falsify our model.

22 Alternatively, we might use the numerous and conflicting proxy records of ^{14}C production to
23 force our model. With this forward approach the $\Delta^{14}\text{C-CO}_2$ record would not serve as model
24 forcing (Fig. 4g) but as model output that could be used to validate the model performance as
25 proposed by the editor. However, the latter approach would yield a multitude of model
26 versions. None of them would fit the $\Delta^{14}\text{C-CO}_2$ record, since our analysis has shown that the
27 model needs the Holocene portion of the ice-core ^{10}Be and the glacial part of the sedimentary
28 ^{10}Be record to produce $\Delta^{14}\text{C-CO}_2$ results consistent with IntCal13 data. This misfit would also
29 strongly affect the calculation of marine $\Delta^{14}\text{C-DIC}$ and $\Delta\Delta^{14}\text{C-DIC}$ values since these depend
30 on atmospheric $\Delta^{14}\text{C-CO}_2$. In summary, we prefer to stick to our more compact inverse
31 approach in order to avoid erroneous $\Delta\Delta^{14}\text{C-DIC}$ results and a further inflation of the
32 manuscript.

33 **Minor comments**

- 34 1. We changed the title accordingly by adding ": a model study" at the end.
- 35 2. We have shortened the paragraph to: "In our model about equal portions of the extreme
36 deglacial carbon flux are triggered by changes in circulation and nutrient utilization in the
37 Southern Ocean (Fig. 7). However, this model outcome is not well constrained because the
38 lack of both proxy data and physical process understanding impedes an unequivocal
39 determination of the magnitude of nutrient utilization and stratification change in the Southern
40 Ocean."

1 3. We added: “The biological pump needed about 2 kyr to reestablish the vertical DIC
2 gradient due to the large inventory of DIC in the deep ocean.”

3 4. These processes are removing CO₃²⁻ from the *global* ocean. Since the deep ocean forms a
4 major part of the global ocean the decline is also reflected in the model results for the deep
5 ocean. We now replaced “deep ocean” by “global ocean” to avoid confusion.

6

7 **References**

8 Frank, M., Schwarz, B., Baumann, S., Kubik, P.W., Suter, M. and Mangini, A. (1997) A 200
9 kyr record of cosmogenic radionuclide production rate and geomagnetic field intensity
10 from ¹⁰Be in globally stacked deep-sea sediments. *Earth and Planetary Science*
11 *Letters* 149, 121-129.

12 Köhler, P., Muscheler, R. and Schmitt, J. (2006) A model-based interpretation of low-
13 frequency changes in the carbon cycle during the last 120,000 years and its
14 implications for the reconstruction of atmospheric D¹⁴C. *Geochemistry, Geophysics,*
15 *Geosystems* 7, doi:10.1029/2008PA001703.

16 Laj, C., Kissel, C., Mazaud, A., Michel, E., Muscheler, R. and Beer, J. (2002) Geomagnetic
17 field intensity, North Atlantic Deep Water circulation and atmospheric D¹⁴C during
18 the last 50 kyr. *Earth and Planetary Science Letters* 200, 177-190.

19 Lal, D. and Charles, C. (2007) Deconvolution of the atmospheric radiocarbon record in the
20 last 50,000 years. *Earth and Planetary Science Letters* 258, 550-560.

21 Muscheler, R., Beer, J., Kubik, P.W. and Synal, H.-A. (2005) Geomagnetic field intensity
22 during the last 60,000 years based on ¹⁰Be and ³⁶Cl from the Summit ice cores and ¹⁴C.
23 *Quaternary Science Reviews* 24, 1849-1860.

24 Reimer, P.J., Bard, E., Bayliss, A., Beck, J.W., Blackwell, P.G., Ramsey, C.B., Buck, C.E.,
25 Cheng, H., Edwards, R.L., Friedrich, M., Grootes, P.M., Guilderson, T.P., Haflidason,
26 H., Hajdas, I., Hatté, C., Heaton, T.J., Hoffmann, D.L., Hogg, A.G., Hughen, K.A.,
27 Kaiser, K.F., Kromer, B., Manning, S.W., Niu, M., Reimer, R.W., Richards, D.A.,
28 Scott, E.M., Southon, J.R., Staff, R.A., Turney, C.S.M. and Plicht, J.v.d. (2013)
29 IntCal13 and marine13 radiocarbon age calibration curves 0 - 50,000 years Cal BP.
30 *Radiocarbon* 55, 1869-1887.

31 Sarinthein, M., Balmer, S., Grootes, P.M. and Mudelsee, M. (2015) Planktic and benthic ¹⁴C
32 reservoir ages for three ocean basins, calibrated by a suite of ¹⁴C plateaus in the
33 glacial-to-deglacial Suigetsu atmospheric ¹⁴C record. *Radiocarbon* 57, 129-151.

1 Sarnthein, M., Schneider, B. and Grootes, P.M. (2013) Peak glacial ^{14}C ventilation ages
2 suggest major draw-down of carbon into the abyssal ocean. *Clim. Past* 9, 2595-2614.

3 Schmitt, J., Schneider, R., Elsig, J., Leuenberger, D., Laurantou, A., Chappellaz, J., Köhler,
4 P., Joos, F., Stocker, T.F., Leuenberger, M. and Fischer, H. (2012) Carbon isotope
5 constraints on the deglacial CO_2 rise from ice cores. *Science* 336, 711-714.

6

7

1 **Effects of eustatic sea-level change, ocean dynamics, and**
2 **nutrient utilization on atmospheric pCO₂ and seawater**
3 **composition over the last 130,000 years: a model study**

4
5 **K. Wallmann¹, B. Schneider², M. Sarnthein^{2,3}**

6
7 [1] GEOMAR Helmholtz Centre for Ocean Research Kiel, Wischhofstr. 1-3, D-24148 Kiel,
8 Germany

9 [2] Institut für Geowissenschaften, University of Kiel, Olshausenstr. 40, 24098 Kiel, Germany

10 [3] Institut für Geologie, University of Innsbruck, Innrain 50, 6020 Innsbruck, Austria

11 Correspondence to: K. Wallmann (kwallmann@geomar.de)

12
13 **Abstract**

14 We developed and employed an earth system model to explore the forcings of atmospheric
15 pCO₂ change and the chemical and isotopic evolution of seawater over the last glacial cycle.
16 Concentrations of dissolved phosphorus (DP), reactive nitrogen, molecular oxygen, dissolved
17 inorganic carbon (DIC), total alkalinity (TA), ¹³C-DIC and ¹⁴C-DIC were calculated for 24
18 ocean boxes. The bi-directional water fluxes between these model boxes were derived from a
19 3-D circulation field of the modern ocean (Opa 8.2, NEMO) and tuned such that tracer
20 distributions calculated by the box model were consistent with observational data from the
21 modern ocean. To model the last 130 kyr, we employed records of past changes in sea-level,
22 ocean circulation, and dust deposition. According to the model, about half of the glacial pCO₂
23 drawdown may be attributed to marine regressions. The glacial sea-level low-stands implied
24 steepened ocean margins, a reduced burial of particulate organic carbon, phosphorus, and
25 neritic carbonate at the margin seafloor, a decline in benthic denitrification, and enhanced
26 weathering of emerged shelf sediments. In turn, low-stands led to a distinct rise in the
27 standing stocks of DIC, TA, and nutrients in the global ocean, promoted the glacial
28 sequestration of atmospheric CO₂ in the ocean, and added ¹³C- and ¹⁴C-depleted DIC to the
29 ocean as recorded in benthic foraminifera signals. The other half of the glacial drop in pCO₂
30 was linked to inferred shoaling of Atlantic meridional overturning circulation and more
31 efficient utilization of nutrients in the Southern Ocean. The diminished ventilation of deep

1 water in the glacial Atlantic and Southern Ocean led to significant ^{14}C depletions with respect
2 to the atmosphere. According to our model, the deglacial rapid and stepwise rise in
3 atmospheric pCO_2 was induced by upwelling both in the Southern Ocean and subarctic North
4 Pacific and promoted by a drop in nutrient utilization in the Southern Ocean. The deglacial
5 sea-level rise led to a gradual decline in nutrient, DIC, and TA stocks, a slow change due to
6 the large size and extended residence times of dissolved chemical species in the ocean. Thus,
7 the rapid deglacial rise in pCO_2 can be explained by fast changes in ocean dynamics and
8 nutrient utilization whereas the gradual pCO_2 rise over the Holocene may be linked to the
9 slow drop in nutrient and TA stocks that continued to promote an ongoing CO_2 transfer from
10 the ocean into the atmosphere.

11

12 **1 Introduction**

13 The discussion of mechanisms that might be responsible for the glacial to interglacial change
14 in the atmosphere's CO_2 content is focused on the ocean (Broecker, 1982a). Ever increasing
15 evidence suggests that CO_2 sequestered in the glacial ocean was rapidly released into the
16 atmosphere at glacial terminations (Schmitt et al., 2012). The fast decline in dust-bound iron
17 deposition in the Southern Ocean (Martin, 1990; Martinez-Garcia et al., 2014) and upwelling
18 pulses in the Southern Ocean (Anderson et al., 2009) and North Pacific (Rae et al., 2014) may
19 have induced the stepwise pCO_2 rise documented in the deglacial ice-core record (Marcott et
20 al., 2014). The preceding CO_2 uptake in the glacial ocean may be attributed to enhanced
21 export production, elevated seawater alkalinity, and changes in ocean dynamics. The
22 biological pump probably was intensified by iron fertilization (Martin, 1990) and the coeval
23 expansion of nitrate (Deutsch et al., 2004) and phosphate (Broecker, 1982a) stocks in the
24 glacial ocean while seawater alkalinity may have been enhanced by the demise of neritic
25 carbonate formation (Berger, 1982; Opdyke and Walker, 1992; Kleypas, 1997). The
26 sequestration of atmospheric pCO_2 in the glacial ocean may have been further promoted by
27 the glacial shoaling of the Meridional Overturning Circulation (MOC) in the Atlantic
28 (Duplessy et al., 1988; Sarnthein et al., 1994), a possible increase in Southern Ocean
29 stratification (Toggweiler, 1999), a prolonged residence time of surface waters in the
30 Southern Ocean providing more time for the biota to draw down nutrients and CO_2 (Watson et
31 al., 2015) and a global decline in MOC intensity and deep ocean ventilation (Sarnthein et al.,
32 2013).

1 In part, a glacial rise in nitrate, phosphate, and alkalinity concentrations, which may have
2 contributed significantly to the drawdown of atmospheric pCO₂, can be explained by eustatic
3 sea-level fall (Wallmann, 2014). It led to a retreat of ocean margins to steeper terrains that
4 reduced the seafloor area located in shallow waters (Fig. 1). The standing stocks of carbon
5 and nutrients in the glacial ocean may have been significantly enhanced by the marine
6 regression and the decrease in shallow margin area since major removal fluxes, that is
7 accumulation of neritic carbonate, benthic denitrification, burial of particulate organic carbon
8 (POC) and phosphorus (P), depend on the extent of seafloor located in shallow waters.
9 Various authors and earth system models considered the glacial decrease in shelf carbonate
10 burial as a major driver of ocean chemistry and atmospheric pCO₂ change (Berger, 1982;
11 Opdyke and Walker, 1992; Brovkin et al., 2012; Ganopolski et al., 1998), since neritic
12 carbonates contribute ≥50 % to the carbonate accumulation at the global seafloor (Milliman
13 and Droxler, 1996; Kleypas, 1997; Berelson et al., 2007). However, the effects of sea-level
14 change on POC and nutrient cycling are largely ignored in these state-of-the-art models even
15 though >50 % of the global benthic denitrification and burial of marine POC and P occur in
16 shelf and upper slope environments (Bernier, 1982; Bohlen et al., 2012; Wallmann, 2010).

17 Against this background, our contribution aims to explore and quantify the effects of sea-level
18 change, ocean dynamics and nutrient utilization on seawater composition and atmospheric
19 pCO₂ over the last glacial cycle. We use a simple earth system box model to simulate both
20 chemical and isotopic changes in seawater composition and employ isotope data (δ¹³C) to
21 constrain changes in ocean dynamics and deep ocean ventilation. Atmospheric pCO₂ and the
22 distributions of dissolved oxygen, carbonate, and radiocarbon in the glacial ocean serve as key
23 prognostic model variables. They are compared with independent proxy data to address the
24 following specific questions: What fraction of the glacial pCO₂ draw-down can be ascribed to
25 eustatic sea-level fall (Wallmann, 2014)? To which degree do global ¹⁴C data sets assembled
26 by (Sarnthein et al., 2013; Sarnthein et al., 2015) actually reflect our concepts and ideas on
27 glacial and deglacial ocean circulation and carbon cycling? Do marine ¹⁴C data really form a
28 quantitative proxy of DIC in the glacial deep ocean as proposed by (Sarnthein et al., 2013)?
29 To avoid circular reasoning dissolved oxygen, carbonate, and radiocarbon distributions
30 calculated for the glacial ocean were not used to parameterize our model. These distribution
31 patterns and the atmospheric pCO₂ values calculated in the model are non-trivial
32 consequences of interactions between the various model components and thus are employed
33 to validate the model performance.

1 **2 Model set-up**

2 The atmospheric partial pressure of CO₂ (pCO₂) serves as the key prognostic variable of the
3 new multi-box earth system model presented in this paper. It was calculated considering
4 continental weathering and degassing processes and gas exchange with the surface ocean
5 (Wallmann, 2014). The oceans were represented by 24 boxes (Fig. 2). The major ocean
6 basins North Atlantic (NA, 30°- 60°N), Tropical Atlantic (TA, 30°N – 30°S), Southern
7 Ocean (SO, >30°S), Tropical Indo-Pacific (TIP, 30°N – 30°S), North Pacific (NP, 30°- 60°N),
8 and Arctic Ocean (AR, >60°N; including the Greenland-Norwegian Sea) each were divided
9 into surface, intermediate, deep and bottom water boxes extending from 0 – 100 m, 100 –
10 2000 m, 2000 – 4000 m to >4000 m water depth, respectively. The following tracer
11 concentrations were calculated as prognostic variables for each of the water boxes: Salinity
12 (Sal), dissolved phosphorus (DP), dissolved reactive nitrogen (DN), dissolved oxygen (DO),
13 total alkalinity (TA), dissolved inorganic carbon (DIC), dissolved inorganic ¹³C (¹³C-DIC),
14 and dissolved inorganic radiocarbon (¹⁴C-DIC). Details of the model set-up are given in
15 Appendix A.

16 Eustatic sea-level change was applied as major model forcing (Fig. 3). Changes in global
17 ocean volume, salinity, depositional area at continental margins and exposed shelf area were
18 derived from the sea-level record (Stanford et al., 2011; Waelbroeck et al., 2002) and the
19 hypsographic curve (Eakins and Sharman, 2012). The burial rate of neritic carbonates was
20 reduced during marine regressions in proportion to the decrease in seafloor area available for
21 the growth of tropical reefs and carbonate platforms (Appendix B). We tested the degree to
22 which the decrease in seafloor area at 0 - 100 m and 100 – 2000 m water depth during glacial
23 sea-level low-stands affected benthic denitrification and the burial of organic carbon and
24 marine phosphorus on the continental shelf and slope (Appendix B) while we assumed that
25 carbonate, P, and POC weathering were promoted by the exposure of shelf sediments
26 (Appendix A).

27 The comprehensive geological data base on benthic foraminiferal δ¹³C (Oliver et al., 2010;
28 Sarnthein et al., 1994) was employed to constrain water fluxes for the Last Glacial Maximum
29 (LGM). Mean δ¹³C-DIC values were calculated for those ocean boxes where sufficient δ¹³C
30 data were available and compared to model results. Water fluxes were varied until the
31 Holocene-LGM differences in δ¹³C generated by the model were consistent with the
32 differences recorded in foraminifera (Tab. A5). The tuning was done using full transient runs
33 with all forcings applied. The resulting fluxes are shown in Fig. 2. The southward water flux

1 from the Atlantic into the Southern Ocean was relocated from deep (2000 – 4000 m) to
2 intermediate waters (100 – 2000 m) to mimic the shoaling of the Atlantic Meridional
3 Overturning Circulation (AMOC) which is inferred not only from $\delta^{13}\text{C}$ data but also from
4 various other proxy records (Curry and Oppo, 2005; Piotrowski et al., 2005; Roberts et al.,
5 2010). Bottom water fluxes from the Southern Ocean into the Atlantic were enhanced during
6 the LGM while the northward flow of surface water was reduced. The overall water exchange
7 between Atlantic and Southern Ocean was maintained constant at 15.4 Sv. The bottom and
8 deep water exchange between the Southern Ocean and the Indo-Pacific was reduced by 5 Sv
9 to reproduce the $\delta^{13}\text{C}$ data (Tab. A5).

10 The eustatic sea-level curve (Fig. 3a) was applied to change ocean dynamics continuously
11 over time that is to define water fluxes over the full model period (Fig. 4a-c). Thus we
12 assumed that AMOC shoaled gradually during the transition from interglacial to full glacial
13 conditions (130 – 21 ka) while the horizontal exchange flux of intermediate waters between
14 Southern Ocean and Tropical Indo-Pacific was enhanced over the glacial to mimic the
15 ventilation of tropical oxygen minimum zones (OMZs) observed in various proxy records
16 (Altabet et al., 1995; Jaccard and Galbraith, 2012). Additional rapid changes were
17 implemented for the deglacial period (Figs. 4a and 4d). NADW formation was strongly
18 reduced during Heinrich Event 1 (H1) and the Younger Dryas (McManus et al., 2004) while
19 upwelling pulses were prescribed in the Southern Ocean during H1 and the Bølling-Allerød
20 (Anderson et al., 2009; Skinner et al., 2010) and in the North Pacific during H1 (Rae et al.,
21 2014). Timing and intensity of these deglacial upwelling/ventilation events were varied until
22 $\Delta^{14}\text{C}$ -DIC values calculated for deep and surface water boxes were consistent with $\Delta^{14}\text{C}$
23 values recorded in benthic and pelagic foraminifera (Fig. A2). In addition, the deglacial ice-
24 core record of $p\text{CO}_2$ (Marcott et al., 2014) and biogenic opal accumulation rates (Anderson et
25 al., 2009) were employed to constrain the timing and intensity of upwelling pulses in the
26 Southern Ocean. The iron accumulation record from site ODP 1090 was used to constrain
27 changes in nutrient utilization in the Southern Ocean (Martinez-Garcia et al., 2014) assuming
28 that the increase in iron accumulation observed at this site directly translates into an increase
29 in the efficiency of nutrient utilization (Fig. 4e). To calculate realistic marine isotope trends
30 the changing isotopic compositions of atmospheric CO_2 were set to the values documented in
31 the geological record (Fig. 4f-g). Atmospheric $\delta^{13}\text{C}$ - CO_2 was not calculated as a prognostic
32 model variable because a biased vertical $\delta^{13}\text{C}$ -DIC gradient in the Southern Ocean impeded
33 the simulation of ^{13}C - CO_2 fluxes across the ocean/atmosphere interface (Appendix A, section
34 A8, Fig. A3).

1 The major limitations of our simple box model are i) very low spatial resolution, ii) water
2 fluxes between model boxes that are not derived from internal model dynamics, iii) terrestrial
3 inventories of POC in vegetation and soil that are kept constant over the model period.

4 As a consequence of low resolution, OMZs are not resolved by our model since the entire
5 Indo-Pacific intermediate water at 100 - 2000 m water depth is pooled in a single ocean box.
6 In our model, we prescribe a constant rate of pelagic denitrification since we are not able to
7 resolve OMZs. Rates of benthic denitrification and P burial are only moderately affected by
8 the lack of OMZs since the area where OMZs impinge the seafloor only amounts to 1 % of
9 the global seafloor (Bohlen et al., 2012).

10 The modern water fluxes applied to our box model are based on a dynamically consistent
11 circulation field. As explained in Appendix A, these fluxes were modified to obtain tracer
12 distributions that are consistent with observations in the pre-industrial modern ocean (Fig.
13 A1). Glacial and deglacial changes in ocean circulation were not derived from ocean models
14 but from $\delta^{13}\text{C}$ records (Tab. A5) and additional geochemical observations (Fig. A2). Models
15 with explicit ocean dynamics are superior to any kind of physically unconstrained box model
16 if they generate results that are consistent with observations. However, the physically-
17 constrained earth system models that we are aware of are not yet able to reproduce as many
18 tracer and proxy data as our box model. Our paper shows that shelf and sea-level effects help
19 to explain a wide range of findings (section 3) and we think that the outputs of physically
20 better constrained models may improve in case these effects are included in the model
21 architecture. It is not our intention to promote box modeling *per se* as the method-of-choice.
22 Rather we hope that the concepts and ideas advanced in our paper may stimulate the
23 community and help to further enhance cutting-edge earth system models with explicit ocean
24 dynamics (Tschumi et al., 2011a; Menviel et al., 2012; Brovkin et al., 2012; Roth et al., 2014;
25 Lambert et al., 2015).

26 For many decades it was widely assumed that the modern terrestrial carbon pool exceeds the
27 glacial pool by hundreds of Gt because of biosphere regrowth after the glacial termination
28 (Köhler and Fischer, 2004). This concept was initially developed to explain reduced $\delta^{13}\text{C}$
29 values in glacial seawater (Shackleton, 1977). However, the latest assessment of terrestrial
30 carbon pools indicates that the sum of the modern stocks does not exceed the LGM stock
31 (Brovkin and Ganopolski, 2015). Moreover, this new view on terrestrial carbon cycling
32 suggests a deglacial decline in total carbon stocks since the carbon release from high latitude
33 areas (melting permafrost soils and soils exposed by the retreat of glacial ice sheets) exceeded

1 the carbon uptake by biosphere regrowth and peat accumulation. Our model explains
2 deglacial and Holocene pCO₂ dynamics and the low glacial δ¹³C values by marine processes
3 and sea-level change only. However, we acknowledge that terrestrial processes that are
4 neglected in our model may have played a role especially over the Holocene even though
5 more work needs to be done to constrain the sign and magnitude of terrestrial effects on δ¹³C
6 and pCO₂ dynamics.

7 The major new component included in our earth system model is a comprehensive
8 formulation of shelf processes and sea-level effects. Appendix B explains in detail how sea-
9 level change affects fluxes at continental margins and how these effects are considered in the
10 model. [The full model code is made available by the first author on request.](#)

11

12 **3 Results and Discussion**

13 The model was run over a period of 130 kyr to simulate the behavior of the global system
14 over one full glacial cycle. Simulations start at 130 ka with modern (pre-human) tracer
15 distributions applied as initial values. The standard model run (STD) considers all effects
16 induced by sea-level change, changes in ocean circulation and nutrient utilization, that is the
17 full model forcing as defined in Figures 3 and 4. Additional simulations were performed to
18 better understand the controls on atmospheric pCO₂ and the chemical and isotopic
19 composition of seawater. Simulation STD-CC was run with constant circulation, that is, all
20 water fluxes were maintained at the Holocene level (upper panel of Fig. 2, Tab. A3) over the
21 full model period, whereas simulation STD-CC-CN was performed with the Holocene
22 circulation field and constant nutrient utilization.

23 **3.1 Atmospheric pCO₂**

24 The pCO₂ trend recorded in ice cores (Monnin et al., 2001; Monnin et al., 2004; Marcott et
25 al., 2014; Petit et al., 1999) was well reproduced by the standard simulation (Fig. 5a and 7a).
26 Over the last interglacial, simulated pCO₂ increased from an initial value of 280 ppmv at 130
27 ka to 285 ppmv at 120 ka (Fig. 5a). This increase was accompanied by a decline in nutrient
28 concentrations (Figs. 5f-g) and export production (Fig. 6d), supported by the high sea-level
29 stand promoting burial of phosphorus and benthic denitrification in continental margin
30 sediments. Over the subsequent glacial period, simulated pCO₂ declined due to sea-level fall,
31 enhanced nutrient utilization in the Southern Ocean, and the decline in deep ocean ventilation
32 until 21 ka, when a pCO₂ minimum of 190 ppmv was reached (Fig. 7b). The simulated glacial

1 pCO₂ drawdown was discontinuous, marked by several steps and turning points (Fig. 5a).
2 Major minima in atmospheric pCO₂ occurred at 90 ka (220 ppmv) and 65 ka (198 ppmv).
3 Both of them are well documented in the ice-core record (Fig. 5a) and accompanied by
4 maxima in nutrient utilization (Fig. 4e) and minima in sea-level (Fig. 3a). Sea-level fall and
5 nutrient utilization, thus, may have driven most of the glacial pCO₂ decline. Moreover, they
6 may have induced major turning points in the glacial pCO₂ record.

7 At constant ocean circulation and nutrient utilization (simulation STD-CC-CN), simulated
8 pCO₂ declined to a LGM value of 234 ppmv (Fig. 5a). Additional simulations based on the
9 standard simulation STD helped us to specify the driving forces for this decline (Tab. 1). To
10 study their effect on pCO₂ we suppressed the temporal changes of individual variables. A first
11 simulation test was based on the assumption of constant modern sea surface temperatures
12 (SSTs). It showed that the glacial decline in global mean SST by ca. 2°C (Schmittner et al.,
13 2011) induced a pCO₂ decline by 16 ppmv since the solubility of CO₂ in surface waters was
14 enhanced under low temperatures (compare rows 1 and 2 in Tab. 1). In a second simulation,
15 salinity was set constant, while the other model parameters varied as defined in the STD
16 simulation. Accordingly, the peak glacial increase in salinity induced a relative atmospheric
17 pCO₂ rise by 5 ppmv by lowering the solubility of CO₂ in surface waters (Tab. 1). In a third
18 test, both salinity and the volume of the ocean boxes were kept constant over time. Changes in
19 these parameters induced an LGM pCO₂ rise by 13 ppmv (Tab. 1), illustrating that the
20 contraction of the ocean volume during glacial sea-level low-stands reduced the ocean's
21 capacity to sequester atmospheric CO₂. In summary, the model runs confirmed previous
22 estimates (Broecker, 1982a) showing that the net effect of SST, volume, and salinity changes
23 on glacial pCO₂ is small (decrease by 3 ppmv). Thus, other processes need to be invoked to
24 explain the large glacial drawdown of atmospheric CO₂ simulated by model run STD-CC-CN.

25 Changes in the flux of dissolved phosphorus (DP) exert large effects on pCO₂, since DP is the
26 ultimate limiting nutrient of the model ocean (Menviel et al., 2012). Neglecting the glacial
27 increase in the weathering of P-bearing solids is raising the LGM pCO₂ value by 50 ppmv
28 (Tab. 1, rows 5 vs. 1). Most of the P released during chemical weathering originates from
29 apatite, a mineral equally occurring in all rock types (sedimentary, magmatic and
30 metamorphic). Thus, we assume that the P weathering rate is proportional to the total
31 weathering rate, that is the sum of carbonate, POC and silicate weathering (Wallmann, 2014).
32 During the glacial, total weathering increased due to the weathering of exposed shelf CaCO₃
33 and POC (Munhoven, 2002; Wallmann, 2014). This rise led to the increase in P weathering

1 simulated in the model. However, a further simulation shows that the overall pCO₂ change
2 induced by chemical weathering of silicate, POC, CaCO₃ and P is small (decrease by 3 ppmv)
3 because the glacial CO₂ draw-down induced by P and CaCO₃ weathering was largely
4 compensated by the CO₂ release induced by POC weathering (Tab. 1, STD run with constant
5 rates of chemical weathering). Applying very high molar C : P ratios for POM in shelf
6 sediments (ca. 200), it was previously calculated that shelf weathering resulted in a net
7 increase rather than decrease in atmospheric pCO₂ (Ushie and Matsumoto, 2012). However,
8 most of the phosphorus in shelf sediments and riverine particles is not organic but bound in
9 other reactive, inorganic phases such as carbonate-fluoro-apatite (Bernier and Rao, 1994)
10 which release DP when exposed to weathering (Ruttenberg, 1992; Ruttenberg and Bernier,
11 1993). Thus, the global mean atomic ratio of POC over reactive P in shelf sediments is lower
12 than the C : P ratio of marine organic matter (Baturin, 2007; Wallmann, 2010). Hence, the
13 glacial weathering of shelf sediments induced a small drop rather than a rise in LGM pCO₂
14 (Tab. 1).

15 By contrast, a stronger effect results from testing the glacial decrease in depositional areas at
16 continental margins, as revealed by a simulation that ignores the glacial decline in P burial
17 and reveals a glacial pCO₂ rise by 73 ppmv (Tab. 1) with respect to the standard case due to
18 the decline in DP concentration and export production. An additional simulation with constant
19 depositional area for POC burial resulted in a pronounced drawdown of both atmospheric
20 pCO₂ (by 61 ppmv) and DIC since POC burial at continental margins served as major sink for
21 CO₂ and DIC in the model system (Tab. 1). Changes in the burial of neritic carbonates were
22 mitigated by carbonate compensation at the deep-sea floor and thus had a less drastic effect on
23 atmospheric pCO₂ (change by 10 ppmv, Tab. 1). Thus the response of the model system to
24 sea-level change was dominated by changes in the burial of P and POC at continental
25 margins. The glacial drop in atmospheric pCO₂ that was induced by a decline in P burial, was
26 moderated by a coeval drop in POC burial at continental margins. The overall effect was an
27 increase in export production and a transfer of CO₂ from the atmosphere into the ocean via the
28 biological pump. Accordingly, most of the glacial pCO₂ decline in simulation STD-CC-CN
29 was driven by the glacial steepening of ocean margins and the resulting expansion of the DP
30 inventory. This conclusion is consistent with the results of previous experiments conducted
31 with more evolved earth system models showing a strong pCO₂ draw-down in response to an
32 increase in the oceanic phosphate inventory (Tschumi et al., 2011a; Menviel et al., 2012).

1 The glacial pCO₂ value dropped by 31 ppmv (from 234 ppmv to 203 ppmv) upon enhanced
2 nutrient utilization (difference between simulations STD-CC-CN and STD-CC). This
3 decrease was amplified by the glacial sea-level fall since the nutrient reservoir that was
4 unlocked by the enhanced utilization in the glacial Southern Ocean was enlarged as a result of
5 glacial marine regression. The remaining portion of the interglacial-to-peak glacial pCO₂ drop
6 by 13 ppmv down to the final LGM value of 190 ppmv was induced by ocean dynamics
7 (difference between simulation STD and STD-CC). Atmospheric pCO₂ rose by 10 ppmv,
8 when all water fluxes between the Atlantic and the Southern Ocean were maintained at their
9 Holocene level over the entire model period (simulation STD with constant AMOC, Tab. 1).
10 The glacial AMOC shoaling (Fig. 4a-b) thus contributed 10 ppmv to the simulated LGM
11 decline. This effect can be attributed to enhanced CO₂ storage in the deep Atlantic (>2000 m
12 water depth) which was less ventilated under glacial conditions, since the formation of
13 northern deep waters was greatly diminished and replaced by southern-source waters enriched
14 in DIC. Thus additional DIC was stored in the glacial deep ocean (Ganopolski et al., 2010;
15 Skinner, 2009; Sarnthein et al., 2013). The glacial decrease in water fluxes between the deep
16 Southern Ocean and Tropical Indo-Pacific applied in the model (Fig. 2) likewise supports
17 further sequestration and storage of CO₂ in the deep ocean and the glacial drawdown of
18 atmospheric pCO₂. The circulation changes employed to simulate LGM conditions (Fig. 2)
19 led to a reduction in the global water exchange across the 2000 m depth horizon from a
20 modern amount of 45 Sv down to 31 Sv at 21 ka. This corresponds to an increase in the
21 average residence time of water in the deep ocean (>2000 m) from 470 years in the modern
22 ocean to 680 years during the LGM where the residence time is calculated as ratio of the deep
23 ocean volume ($6.65 \times 10^{17} \text{ m}^3$ at >2000m) and the global vertical water fluxes across 2000 m.
24 The glacial increase in residence time by 210 yr may be compared to the 600 yr increase
25 reconstructed from benthic radiocarbon data (Sarnthein et al., 2013). We suggest that the
26 difference between these two estimates is related to the elevated production rate of
27 radiocarbon in the glacial atmosphere and changes in carbon cycling affecting the marine
28 radiocarbon budget (section 3.4).

29 A stepwise increase in pCO₂ was simulated over the deglaciation (Fig. 7). The first step
30 occurred from 18.5 to 16.3 ka when the simulated pCO₂ rose rapidly from 193 to 220 ppmv.
31 A second step followed at 15.9 - 14.1 ka with a pCO₂ rise from 222 to 244 ppmv, a third step
32 at 13.0 – 10.8 ka with a strong increase from 243 to 272 ppmv. The first step was driven by
33 the rapid drop in nutrient utilization at the glacial termination (Fig. 4e) and the ventilation of
34 intermediate and deep water masses in the North Pacific during H1 (Figs. 4d and A2). The

1 second and third steps were driven by the Southern Ocean where CO₂ was released into the
2 atmosphere due to the abrupt decline in stratification and the further decrease in nutrient
3 utilization (Fig. 4d-e). In major parts of the Southern Ocean these steps coincide with maxima
4 in opal accumulation indicating enhanced upwelling (Anderson et al., 2009). The pCO₂
5 drawdown from 10 to 8 ka reflects a recovery of the ocean system from the antecedent
6 ventilation pulse in the Southern Ocean centered at 11.5 ka (Fig. 4d). According to our model,
7 the ventilation pulse removed CO₂ from the ocean interior, enhanced the O₂ content of the
8 deep ocean, and diminished the vertical DIC and O₂ gradients. The subsequent restoration of
9 the vertical DIC gradient induced the pCO₂ decline observed in the model from 10 to 8 ka.
10 The biological pump needed about 2 kyr to reestablish the vertical DIC gradient due to the
11 large inventory of DIC in the deep ocean. Sea-level change was not uncovered as major driver
12 for the rapid deglacial pCO₂ rise since the long residence times of DP (13 kyr) and TA (77
13 kyr) inhibit fast inventory changes in the global ocean (Menviel et al., 2012; Wallmann,
14 2014). By contrast, the pCO₂ increase over the Holocene (8 – 0 ka), which is closing the
15 glacial cycle, may have been driven by a high sea-level stand inducing a gradual and slow
16 decline in marine DP and TA inventories.

17 In our model about equal portions of the extreme deglacial carbon flux are triggered by
18 changes in circulation and nutrient utilization in the Southern Ocean (Fig. 7). However, this
19 model outcome is not well constrained because the lack of both proxy data and physical
20 process understanding impedes an unequivocal determination of the magnitude of nutrient
21 utilization and stratification change in the Southern Ocean. As shown in Fig. 7, about equal
22 portions of the extreme deglacial carbon flux may have been triggered by changes in
23 circulation and nutrient utilization. Nutrients may have been used more efficiently in the
24 glacial Southern Ocean due to the enhanced dust input fertilizing the surface layer (Martinez-
25 Garcia et al., 2014) and because of buoyancy forces prolonging the residence time of nutrients
26 in the euphotic zone (Watson et al., 2015). However, further processes that are not considered
27 in our model such as the deglacial melting of permafrost (Zimov et al., 2006) and volcanic
28 CO₂ degassing (Huybers and Langmuir, 2009) may have also contributed to the pCO₂ rise
29 because the lack of proxy data and physical process understanding impedes an unequivocal
30 determination of the magnitude of nutrient utilization and stratification change in the Southern
31 Ocean.

32 **3.2 Dissolved nutrients and oxygen**

1 The standing stock of DP in the global ocean rose under glacial conditions since P burial was
2 diminished by the decrease in depositional area located at shallow water depths (Fig. 6h)
3 while chemical weathering was promoted by the exposure of shelf sediments (Fig. 6g). Most
4 of the glacial DP rise found in our simulations was induced by the glacial steepening of ocean
5 margins reducing the burial of P in margin sediments (Tab. 1, Fig. 1, Appendix B). Vice
6 versa, enhanced utilization in the Southern Ocean induced a strong decrease in glacial DP
7 stocks since more DP was taken up by phytoplankton to be drawn down and finally buried in
8 marine sediments (simulations STD-CC versus STD-CC-CN, Figs. 5f, 6d, 6h), while the
9 glacial DP stock was largely restored by changes in ocean dynamics (simulations STD versus
10 STC-CC, Fig. 5f) separating the large nutrient pool in the deep ocean from the surface layer.
11 The spatial distribution of DP in the global ocean reflects the export of POM by the biological
12 pump and ocean circulation. The overall pattern, that is a strong vertical gradient between
13 depleted surface waters and enriched deep water masses and a significant horizontal gradient
14 between the deep North Atlantic and North Pacific, was maintained over the glacial cycle
15 (Fig. 8). However, the vertical DP gradient was amplified over the LGM due to enhanced
16 utilization and the decrease in deep ocean ventilation. Reactive P accumulation rates in
17 marine sediments can be used to validate our model results. A global compilation of these
18 data confirmed that P accumulation in shelf sediments decreased drastically under glacial
19 conditions (Tamburini and Föllmi, 2009). The resulting decline in global P burial induced an
20 increase in the glacial DP inventory by 17 – 40 % (Tamburini and Föllmi, 2009) as predicted
21 by our model. Cd/Ca ratios in LGM sediments from the Atlantic Ocean (Boyle and Keigwin,
22 1982) and $\delta^{13}\text{C}$ records (Duplessy et al., 1988; Sarnthein et al., 1994; Oliver et al., 2010)
23 suggest a steepening of the vertical DP gradients broadly consistent with our model results.

24 The dissolved oxygen (DO) content of the global ocean decreased under glacial conditions
25 due to the decline in deep ocean ventilation and increase in export production (Fig. 5h). In
26 contrast, it recovered and peaked over the deglaciation since ocean ventilation was enhanced
27 in the Southern Ocean and the North Pacific. The spatial distribution of DO changed
28 significantly under LGM conditions (Fig. 8). Concentrations declined at >2000 m water depth
29 due to the decrease in ocean ventilation and increase in export production while glacial
30 cooling induced a small DO rise in surface waters. The DO minimum in intermediate waters
31 of the Indo-Pacific expanded and spread into the deep ocean under glacial conditions. The
32 lowest value was calculated for the intermediate water box of the North Pacific where the DO
33 concentration declined to 69 μM at 21 ka. The glacial DO decrease in the deep ocean is
34 consistent with a large data set showing that deep waters below 1500 m water depth were

1 significantly depleted in the LGM over all major ocean basins (Jaccard and Galbraith, 2012).
2 The glacial oxygen depletion in the intermediate Indo-Pacific ($76 \mu\text{M}$ during the LGM vs. 96
3 μM in the modern ocean) seems to be at odds with the geological record which shows that
4 OMZs located in the tropical ocean were better ventilated under glacial conditions (Altabet et
5 al., 1995). This discrepancy may probably arise from the spatial resolution of the box model
6 that is too coarse to resolve OMZs. Moreover, all sediment cores that have been used to
7 reconstruct the oxygen conditions in glacial intermediate waters were taken at continental
8 margins (Jaccard and Galbraith, 2012) while tracer concentrations in the model boxes are
9 basin-wide mean values reflecting open ocean rather than continental margin conditions.

10 The glacial oxygen decline simulated in the model has no significant effect on other model
11 parameters since the oxygen level stays above the threshold values for diminished phosphorus
12 burial ($20 \mu\text{M}$) in all ocean boxes (Wallmann, 2010). It was only benthic denitrification at the
13 deep-sea floor that was enhanced by the glacial oxygen depletion in bottom waters and rising
14 export production (Bohlen et al., 2012). Nevertheless, the global rate of benthic denitrification
15 calculated in simulation STD decreased under glacial conditions (Fig. 6j) since ocean margins
16 retreated into steeper terrain such that less nitrate was consumed on the continental shelf.
17 Nitrogen fixation was assumed to increase when the DN/DP ratio in the surface ocean fell
18 below the N/P ratio in exported POM (Eq. A8). Nitrogen fixation thus traced the temporal
19 evolution of benthic denitrification (Figs. 6i-j). This negative feedback mechanism (Tyrrell,
20 1999; Redfield, 1958) maintained the simulated DN/DP ratio close to its modern value over
21 the entire glacial cycle. The DN inventory peaked during the LGM where it exceeded the
22 modern value by 16 %. A similar increase in the LGM nitrate inventory (10 – 30 %) and
23 glacial decline in denitrification and nitrogen fixation was simulated with a box model
24 constrained by the marine $\delta^{15}\text{N}$ record (Deutsch et al., 2004).

25 **3.3 Dissolved inorganic carbon, carbonate ion concentrations, and $\delta^{13}\text{C}$ of** 26 **dissolved inorganic carbon**

27 In the standard case (STD) the global mean seawater concentrations of dissolved inorganic
28 carbon (DIC) and total alkalinity (TA) decreased over the last interglacial, attained a
29 minimum at its end ($2267 \mu\text{M}$ and $2394 \mu\text{M}$ at 118.5 ka, respectively), increased over the
30 glacial up to a maximum prior to the glacial termination ($2467 \mu\text{M}$ and $2631 \mu\text{M}$ at 19.5 ka)
31 and decreased again over the Holocene (Fig. 5b and 5e). On the basis of our model runs these
32 trends were mainly driven by sea-level change that controlled the burial of neritic carbonate
33 (Fig. 3d) and POC (Fig. 6e) and the rates of POC and carbonate weathering by shelf exposure

1 (Figs. 3h and 6c). The glacial DIC and TA rise was mitigated by nutrient utilization enhancing
2 marine export production and carbon burial (compare simulations STD-CC-CN and STD-CC
3 in Figs. 5 and 6). In turn, it was amplified by the glacial decrease in deep ocean ventilation, a
4 reduced turnover rate that also implied a decrease in marine export production, POC burial
5 and pelagic carbonate accumulation (STD-CC versus STD). Considering changes in ocean
6 volume by about 3 % (Fig. 3b), the increase in DIC over the last glacial (118.5 – 19.5 ka)
7 translates into a mean rate of 1.70 Tmol yr⁻¹. By comparison, the CO₂ uptake from the
8 atmosphere as calculated from the glacial rate of pCO₂ decline amounts to 0.17 Tmol yr⁻¹.
9 Thus, only 10 % of the glacial DIC rise was induced by CO₂ uptake from the atmosphere.
10 According to our model, the glacial demise of neritic carbon pools (carbonate and POC) was
11 the major forcing of the DIC rise, while the sequestration of atmospheric CO₂ only was of
12 minor importance for the glacial change in seawater composition. Most of the excess DIC
13 accumulating in the glacial ocean originated from exposed shelf carbonate and POC and from
14 riverine DIC which was not buried due to the contraction of depositional areas at ocean
15 margins. The accumulation of TA and DIC in the deep ocean (Fig. 9) was corroborated by a
16 change in Atlantic deep water chemistry. As outlined above, this LGM ocean basin was filled
17 with corrosive southern-source waters compromising the preservation of carbonates at the
18 deep-sea floor and diminishing the rate of pelagic carbonate burial (Tab. 1).

19 The global mean concentration of carbonate ions (CO₃²⁻) in the deep ocean (>2000 m) rose
20 over glacial times in simulation STD due to the decline in neritic carbonate burial and
21 dropped over the deglaciation, at least in part, due to the recovery of neritic carbonate
22 deposition (Fig. 10a). The glacial CO₃²⁻ rise was mitigated by the decline in deep ocean
23 ventilation and increase in ocean productivity promoting the sequestration of CO₂ in the deep
24 ocean. Interestingly, deep ocean pH and CO₃²⁻ trends diverged during the transition into the
25 LGM (Figs. 10a-b), that is, pH dropped while CO₃²⁻ was maintained at a constant level over
26 this period (30 – 20 ka). Due to this divergence, the late glacial pH was lower (that is, more
27 acidic) than the modern value, while the CO₃²⁻ concentration exceeded the modern
28 concentration in ocean deep waters. This apparent discrepancy may be explained by the fact
29 that alkalinity and DIC were strongly elevated in late glacial seawater (Figs. 5b and 5e)
30 thereby enhancing the concentrations of both H⁺ and CO₃²⁻ ions with respect to the pre-
31 industrial modern ocean. The deglacial CO₃²⁻ minimum is related to ventilation pulses in the
32 Southern Ocean and North Pacific employed in the model. Export production of CaCO₃ and
33 pelagic carbonate burial were enhanced by these upwelling events and removed dissolved

1 | CO₃²⁻ from the ~~deep-global~~ ocean. The Holocene was marked by a continuous CO₃²⁻ decline
2 | probably induced by the high sea-level stand promoting neritic carbonate burial.

3 | The strong enrichment of dissolved CO₃²⁻ in glacial surface waters was induced by the decline
4 | in atmospheric pCO₂ (Fig. 9). According to our standard simulation, these CO₃²⁻
5 | concentrations exceeded Holocene values down to water depths of 1000 m, likewise at
6 | northern high latitudes where deep-water formation transmitted the signature of glacial
7 | surface waters into the ocean's interior. The carbonate ion concentration was almost constant
8 | over the entire Indo-Pacific at >1000 m water depth since the strong increase in DIC (Fig. 9)
9 | was balanced by a corresponding TA rise. These model results well compare with those of
10 | B/Ca ratios in benthic foraminifera which probably record CO₃²⁻ changes in ambient bottom
11 | waters (Yu et al., 2008; Yu et al., 2013). The model is consistent with glacial to interglacial
12 | changes in deep-sea CO₃²⁻ reconstructed from this proxy (Tab. C1 in Appendix C). The only
13 | deviation occurs at >4km water depth in the Atlantic where the model predicts elevated LGM
14 | values while the data show a glacial CO₃²⁻ depletion (Tab. C1), possibly the result of a strong
15 | east-west gradient in bottom water chemistry not resolved yet by the B/Ca data that
16 | accordingly may not be fully representative for the Atlantic at large.

17 | The glacial distribution pattern of δ¹³C-DIC values calculated in the standard simulation (Fig.
18 | 11) is consistent with observations (Oliver et al., 2010) because glacial δ¹³C-DIC data were
19 | employed to define the LGM circulation pattern (section 2, Tab. A5 in Appendix A). In all
20 | simulations global mean δ¹³C-DIC values mirror inversely DIC concentrations (Figs. 5b-c)
21 | getting depleted with rising DIC concentrations and vice versa. This anti-correlation is linked
22 | to the turnover of POC being strongly depleted in ¹³C as compared to average seawater. The
23 | glacial demise of the sedimentary POC pool, induced by the weathering of exposed shelf
24 | sediments and the decline in depositional areas along continental margins, contributed
25 | significantly to the glacial DIC rise and affected the isotopic evolution of seawater (Broecker,
26 | 1982a; Wallmann, 2014). The glacial δ¹³C-DIC depletion was widely ascribed to a glacial
27 | loss of terrestrial biomass (Shackleton, 1977; Köhler and Fischer, 2004). However, our model
28 | can reproduce almost the entire glacial shift to depleted δ¹³C-DIC values recorded in benthic
29 | foraminifera (0.34 ± 0.19 ‰; (Peterson et al., 2014)) without invoking any net changes in
30 | terrestrial biomass (Tab. A5). This outcome is consistent with results of a new model study
31 | suggesting that the rise in carbon buried in permafrost and under ice largely compensated for
32 | the decline in peat, soil and biomass carbon over the LGM (Brovkin and Ganopolski, 2015).

33 | **3.4 Radiocarbon**

1 Atmospheric $\Delta^{14}\text{C-CO}_2$ was forced to follow the IntCal13 values derived from the geological
2 record by varying the ^{14}C -production rate in the atmosphere (Appendix A, section A8). The
3 ^{14}C production rate was calculated for each time step considering the ^{14}C transfer from
4 atmosphere to oceans and changes in the inventories of atmospheric CO_2 and $^{14}\text{C-CO}_2$. The
5 difference between global mean $\Delta^{14}\text{C-DIC}$ and atmospheric $\Delta^{14}\text{C-CO}_2$ ($\Delta\Delta^{14}\text{C-DIC} = \Delta^{14}\text{C-}$
6 $\text{DIC} - \Delta^{14}\text{C-CO}_2$) depended on the radiocarbon content of the atmosphere (Figs. 5d, 4g, and
7 12). $\Delta^{14}\text{C-CO}_2$ and the model-derived $\Delta\Delta^{14}\text{C-DIC}$ were anti-correlated, since the ^{14}C uptake
8 from the atmosphere was insufficient to raise the radiocarbon content of the model ocean up
9 to the level of elevated $\Delta^{14}\text{C-CO}_2$ values attained during periods of strong atmospheric
10 radiocarbon production. This anti-correlation was also observed in an additional simulation
11 (Fig. 12b) where the carbon cycle and ocean circulation were maintained at a steady state
12 representing Holocene boundary conditions, whereas $\Delta^{14}\text{C-CO}_2$ values were forced to follow
13 the IntCal13 record. In further steady-state simulations the radiocarbon production rate in the
14 atmosphere was held constant over time while the carbon cycle operated in a Holocene
15 steady-state mode with a constant $p\text{CO}_2$ value of 280 μatm . These model runs show that the
16 steady-state $\Delta\Delta^{14}\text{C-DIC}$ values attained after about 100 kyr simulation time decreased with
17 increasing production rate (Appendix C, Tab. C2). As previously shown, changing production
18 rates of radiocarbon in the atmosphere may affect the difference between $\Delta^{14}\text{C}$ values in
19 planktonic and benthic foraminifera (Adkins and Boyle, 1997) and the contrast between
20 atmospheric and marine $\Delta^{14}\text{C}$ values (Franke et al., 2008). However, these effects were
21 regarded as transient features induced by a slow ^{14}C transfer from the atmosphere into the
22 ocean. In contrast, the results of our steady-state model suggest that ^{14}C depletion of the ocean
23 during periods of elevated atmospheric ^{14}C production can be a permanent steady-state feature
24 (Tab. C2), a conclusion further substantiated by a simple steady-state model presented in
25 Appendix D.

26 The standard simulation STD yielded a mean ocean $\Delta\Delta^{14}\text{C-DIC}$ of -270 ‰ for the LGM (21
27 ka) and -152 ‰ at 0 ka corresponding to a glacial $\Delta\Delta^{14}\text{C-DIC}$ decline by 118 ‰. The
28 simulations depicted in Fig. 12b show that multiple processes contributed to the ^{14}C glacial
29 depletion of the ocean with respect to the atmosphere. These include the glacial decline in
30 deep ocean ventilation, sea-level fall, nutrient utilization, and rise in atmospheric radiocarbon
31 production. The $\Delta\Delta^{14}\text{C-DIC}$ decline observed upon sea-level fall in part was induced by the
32 glacial decline in sedimentary carbon pools adding fossil carbon to the global ocean. Glacial
33 changes in ocean circulation contributed to the $\Delta\Delta^{14}\text{C-DIC}$ decline since the glacial demise of
34 ventilation across the 2000 m depth horizon isolated the deep ocean from the atmosphere.

1 However, the simulations suggest that changes in ocean ventilation possibly were responsible
2 for less than one third of the glacial rise in the radiocarbon contrast between global ocean and
3 atmosphere.

4 Atmospheric ^{14}C production rates calculated in the model showed the same trends for all
5 simulations (Fig. 12c). They attained very high values at 25 ka and declined over time. The
6 only significant difference between the model runs occurred during the deglaciation. The
7 standard simulation yielded elevated production rates for this period since the rapid
8 ventilation of the deep ocean considered in simulation STD drew radiocarbon from the
9 atmosphere and released ^{14}C -depleted CO_2 into the atmosphere such that the production rate
10 was enhanced to maintain atmospheric $\Delta^{14}\text{C-CO}_2$ at the deglacial level documented by
11 IntCal13 (Fig. 12a). Our model results may support the hypothesis that a significant fraction
12 of the $\Delta^{14}\text{C-CO}_2$ record is controlled by changes in atmospheric radiocarbon production
13 (Köhler et al., 2006; Broecker et al., 2004).

14 However, in contrast to our model approach various authors have proposed that most of the
15 $\Delta^{14}\text{C-CO}_2$ record can be explained by changes in glacial ocean dynamics and carbon cycling
16 without invoking significantly elevated rates of atmospheric radiocarbon production
17 (Muscheler et al., 2005; Robinson et al., 2005). The Holocene trends calculated in the model
18 are similar to those observed in the ^{10}Be ice-core record (Muscheler et al., 2005) and derived
19 from Holocene geo-magnetic data (Laj et al., 2002) while the glacial values are closer to the
20 stacked sedimentary ^{10}Be record (Frank et al., 1997). Various reasons have been evoked to
21 explain the deviations between different records of atmospheric radionuclide production
22 (Köhler et al., 2006). The controversy suggests a clear need to develop a better constrained
23 record of atmospheric ^{14}C production suitable for model validations (Fig. 12d).

24 The spatial distribution of radiocarbon in the global ocean changed significantly during the
25 LGM (Fig. 11). According to the standard simulation $\Delta\Delta^{14}\text{C-DIC}$ values were strongly
26 depleted over the entire ocean and reached a minimum of -356‰ in North Pacific deep
27 water. Both, vertical and horizontal gradients were strengthened during the LGM. In the
28 modern ocean, marine $\Delta^{14}\text{C-DIC}$ values are correlated with DIC concentrations at water
29 depths below 2000 m (Sarnthein et al., 2013). If this correlation also holds for the glacial
30 ocean, glacial $\Delta\Delta^{14}\text{C-DIC}$ values may be used as proxy for DIC concentrations in glacial
31 seawater (Sarnthein et al., 2013). The model results show that the correlation was indeed
32 maintained in the glacial ocean and the slope of the correlation was similar for all model runs
33 and time slices (Fig. 13). However, the regression line for glacial conditions was shifted to

1 lower DIC and $\Delta\Delta^{14}\text{C}$ -DIC values due to changes in ocean carbon cycling and possibly
2 elevated radiocarbon production rates in the glacial atmosphere. Thus $\Delta\Delta^{14}\text{C}$ -DIC values may
3 serve as new proxy for DIC concentrations in ancient seawater, if suitable methods are found
4 to correct for the glacial shift observed in the simulations (Fig. 13). The overall LGM pattern
5 calculated in the standard simulation (Fig. 11) compares well with trends derived from the
6 radiocarbon contents of planktonic and benthic foraminifera even though radiocarbon data
7 indicate strong gradients within ocean basins, which were not resolved by the box model
8 (Appendix C, Tab. C3). A recent review of glacial $\Delta\Delta^{14}\text{C}$ -DIC data (Sarnthein et al., 2013)
9 revealed radiocarbon depletions in the deep Atlantic, Southern Ocean and Indo-Pacific
10 broadly consistent with those calculated by the model. However, the model was not able to
11 reproduce very strong radiocarbon depletions measured at some deep water sites due to its
12 coarse spatial resolution (Tab. C3). Moreover, it predicts significant ^{14}C -depletions in the
13 Atlantic thermocline which are inconsistent with coral ^{14}C data (Robinson et al., 2005). ^{14}C
14 measurements in foraminiferal shells and corals from the glacial ocean feature strong spatial
15 and temporal variability (Broecker et al., 2004; Sarnthein et al., 2013). More data will help to
16 resolve this variability and constrain the radiocarbon distribution and dynamics of the glacial
17 ocean.

18

19 **4 Conclusions**

20 For a first time we show model results that are consistent with both the atmospheric pCO_2
21 record (Figs. 5 and 7) and data on past distribution changes of dissolved oxygen, carbonate,
22 and radiocarbon in the glacial ocean (Figs. 8, 9, 11 and Tabs. C1 and C3). Atmospheric pCO_2
23 and the glacial distribution of seawater tracers were not prescribed but calculated as
24 prognostic model variables. Only marine $\delta^{13}\text{C}$ data were used to parameterize the glacial
25 circulation model. A comprehensive formulation of shelf processes and sea-level effects is a
26 major new component included in our earth system model. Thus, the conformity between
27 independent proxy data and key model results (atmospheric pCO_2 change over the last 130
28 kyr, distribution of dissolved oxygen, carbonate, and radiocarbon in the LGM ocean) supports
29 our hypothesis that the glacial sea-level drop induced a decline in atmospheric pCO_2 and a
30 rise in the inventories of nutrients, DIC, and alkalinity in the glacial ocean (Wallmann, 2014).
31 Also, we first show that the slope of DIC versus radiocarbon observed in the modern deep
32 ocean (Sarnthein et al., 2013) was probably maintained in the glacial ocean (Fig. 13).
33 However, a glacial shift in the intercept now complicates the use of ^{14}C as DIC proxy.

1 The shelf hypothesis was originally developed to explain the deglacial rise in atmospheric
2 pCO₂ (Broecker, 1982b). In contrast, our model analysis reveals that shelf and sea-level
3 effects were not responsible for this rapid rise but account for a major portion of the slow
4 glacial decline of atmospheric pCO₂ (Figs. 5 and 7). The deglacial sea-level rise induced a
5 decline in nutrient and carbon stocks in the global ocean. However, these stocks changed only
6 slowly due to their large size (Menviel et al., 2012). The gradual pCO₂ rise over the Holocene
7 may be attributed to the slow relaxation of nutrient and carbon stocks promoting CO₂ transfer
8 from the ocean into the atmosphere. The slow relaxation may also be responsible for the
9 imbalance in phosphate and TA sources and sinks observed in the modern ocean (Wallmann,
10 2010, 2014). Stocks of these chemical species may decline until today since tens of thousands
11 of years may be needed to draw down the dissolved P and TA inventories from their peak
12 values attained over the last glacial maximum.

13 According to standard Milankovitch theory (Milankovitch, 1941), variations in summer
14 insolation at high latitudes (Berger and Loutre, 1991) cause waxing and waning of northern
15 ice sheets (Fig. 14). Most of the global climate change over a glacial cycle is thus believed to
16 be driven by northern summer insolation and ice sheet dynamics (Denton et al., 2010).
17 However, it has always been difficult to explain why atmospheric pCO₂ declined over glacial
18 periods and how this drop was connected to the built-up of large continental ice sheets. The
19 sea-level effects explored in this paper provide the missing link between glacial ice sheet and
20 pCO₂ dynamics. The sea-level-driven pCO₂ decline was amplified by a decrease in deep
21 ocean ventilation, a decline in sea surface temperature, and enhanced nutrient utilization.
22 These additional changes were driven by a combination of greenhouse gas, albedo, and
23 insolation forcing (Fig. 14). Glacial terminations occurred when summer insolation increased
24 at northern latitudes (Raymo et al., 1997), ice sheets reached a critical size (Denton et al.,
25 2010), and carbonate compensation at the deep-sea floor reversed the declining pCO₂ trend
26 (Wallmann, 2014). The deglacial warming was again driven by greenhouse gas, albedo, and
27 insolation forcing promoting the retreat of continental ice sheets, sea-level rise, ocean
28 ventilation, and the decline in nutrient utilization in a positive feedback mode.

29 Due to their internal non-linear dynamics, continental ice sheets are able to generate 100-kyr
30 cycles with a slow glacial expansion and rapid deglacial contraction of ice volume under
31 Milankovitch forcing even though insolation oscillates on much shorter time scales (Imbrie
32 and Imbrie, 1980; Abe-Ouchi et al., 2013; Ganopolski and Calov, 2011; Pollard, 1983).
33 Positive feedbacks embedded in the global carbon cycle are able to generate a 100-kyr cycle

1 without any form of external forcing when surface temperature, ice volume, sea-level and
2 ocean circulation are assumed to be controlled by pCO₂ (Wallmann, 2014). Thus, both,
3 continental ice sheets and the global carbon system have the inherent tendency to generate
4 cycles with a length of 100 kyr. They interact via sea-level and pCO₂ change, respond to
5 insolation forcing, control changes in the climate system (surface temperature, ocean and
6 atmospheric circulation) and may generate the 100-kyr cycle dominating late Quaternary
7 climate change.

8

1 **Appendix A: Model set-up and calibration**

2 **A1 Data and procedures for model calibration**

3 Mean tracer concentrations were calculated for each of the model boxes using the GLODAP
4 data base for total alkalinity, DIC, ^{13}C -DIC and ^{14}C -DIC (Key et al., 2004) and the World
5 Ocean Atlas (WOA01) for temperature, salinity, PO_4 , NO_3 and O_2 (Conkright et al., 2002).
6 ^{14}C -DIC-data were corrected by subtracting the bomb- ^{14}C signal and DIC data were corrected
7 for the intrusion of anthropogenic CO_2 (Key et al., 2004) whereas ^{13}C -DIC data were not
8 corrected and are thus affected by ^{13}C -depleted anthropogenic CO_2 . The model was run into
9 steady state under pre-anthropogenic boundary conditions and resulting tracer concentrations
10 were compared to data to validate the model output and calibrate the model (Tab. A1 and A2,
11 Fig. A1). The pCO_2 value and global export production of particulate organic carbon were
12 used as additional constraints, i.e. the calculated values had to comply with the corresponding
13 observations (ca. 280 μatm and ca. 700 - 900 Tmol yr^{-1} , respectively, (Sarmiento and Gruber,
14 2006). For these initial model runs, the riverine fluxes to the ocean were enhanced to
15 compensate for the removal fluxes observed in the modern ocean. The atmospheric pCO_2
16 value was calculated applying a constant continental CO_2 uptake rate balancing the CO_2 being
17 produced in the modern ocean by carbonate burial and degassing processes (Wallmann,
18 2014). The isotopic composition of atmospheric CO_2 was maintained at a constant level
19 representative for the pre-human atmosphere ($\delta^{13}\text{C} = -6.5 \text{ ‰}$, $\Delta^{14}\text{C} = 0 \text{ ‰}$). Water fluxes
20 (Tab. A3) and parameter values for key biogeochemical processes (Tab. A4) were varied
21 until pCO_2 , global export production, and the tracer distribution fields generated by the
22 steady-state box model were consistent with data (Tab. A1 and A2, Fig. A1). A good fit was
23 obtained for all tracers except ^{13}C -DIC. ~~Most~~ Some of the ^{13}C mismatch was induced by
24 anthropogenic ^{13}C which has a strong effect on the observations in the modern ocean but was
25 not considered in the model simulations.

26 **A2 Ocean circulation and tracer transport**

27 Water fluxes between adjacent boxes were calculated using output of the Opa 8.2 ocean
28 circulation model in the framework of NEMO (Nucleus for European Modeling of the Ocean)
29 to start with a configuration that is dynamically consistent with a 3-D forward ocean model
30 (Madec et al., 1998). NEMO was forced by atmospheric reanalysis data as described in
31 (Aumont and Bopp, 2006). A more detailed analysis of the resulting large-scale circulation
32 pattern is given in (Bordelon-Katrynski and Schneider, 2012). The calculation of water
33 exchange was based on horizontal and vertical velocities on the box model grid. In order to

1 consider two-way exchange between the boxes, not only the net transports, but fluxes in both
2 directions (northward/southward, up/down) were taken into account. Water fluxes at the
3 atmosphere-ocean boundary were calculated as residual fluxes balancing the water exchange
4 for each vertical column. Test runs with the box model revealed, however, that tracer
5 distributions calculated with the NEMO-derived water fluxes were inconsistent with tracer
6 data when the NEMO circulation field was applied in the box model. This mismatch was
7 induced by the coarse spatial resolution of the box model and by errors inherent to the NEMO
8 simulations. The NEMO-derived circulation field was, thus, modified to allow for a better fit
9 to the independent observations listed in Tab. A1 and Tab. A2 and to bring the circulation
10 field in line with other observations and GCM modeling results. Thus, NEMO features a
11 North Atlantic Deep Water (NADW) formation rate of only ca. 10 Sv whereas tracer data
12 (radiocarbon, phosphate, oxygen) constrain this rate at ca. 15 Sv (Broecker et al., 1998).
13 Moreover, NEMO predicts that Antarctic Bottom Water (AABW) upwells in the Indo-Pacific
14 all the way to the thermocline and surface ocean. This pattern is consistent with the “great
15 ocean conveyor” (Broecker, 1991) but in conflict with other more recent ocean models
16 suggesting that deep water ascent occurs in the Southern Ocean rather than in the Indo-Pacific
17 (Sarmiento and Gruber, 2006). These models show that AABW flowing into the Indo-Pacific
18 returns as deep water to the Southern Ocean where it ascends to form intermediate water
19 masses flowing northwards into the major ocean basins (Imbrie et al., 1993; Gnanadesekian
20 and Hallberg, 2002; Marinov et al., 2006). NEMO also predicts an extremely high rate of
21 vertical water exchange in the Southern Ocean across 2000 m water depth of more than 200
22 Sv. These strong upward and downward water fluxes are inconsistent with tracer observations
23 showing strong vertical gradients between the deep ocean (>2000 m water depth) and the
24 overlying water masses. The water fluxes derived from NEMO were modified to remove
25 these biases and to provide more realistic water fluxes for the box model (Tab. A3). The
26 corresponding best-fit water fluxes are bidirectional, i.e. water flows in both directions
27 between each of the adjacent model boxes (Tab. A3). The net fluxes (Tab. A3) were
28 calculated as difference between these opposing fluxes. They represent the meridional
29 overturning circulation (MOC) as implemented in the box model (Fig. 2): NADW is formed
30 in the North Atlantic and Arctic basins at an overall rate of ca. 15 Sv. It flows towards the
31 Southern Ocean where Antarctic Bottom Water (AABW) is formed at a rate of ca. 18 Sv. A
32 minor AABW fraction flows northwards into the Atlantic while most of the AABW is filling
33 the deep basins of the Indo-Pacific at a rate of ca. 16 Sv where it upwells and returns into the
34 Southern Ocean as deep water. Intermediate water formed by deep water ascent in the

1 Southern Ocean flows into the Indo-Pacific at a rate of ca. 14 Sv where it upwells to form
2 surface water flowing back towards the Southern Ocean. Surface waters flowing northward
3 into the Atlantic and returning as NADW to the Southern Ocean are closing the loop. This
4 overall MOC pattern and the corresponding flow rates are consistent with tracer data and
5 other observations (Sarmiento and Gruber, 2006).

6 The exchange fluxes between adjacent boxes reflect, both, opposing water flows across the
7 box boundaries and eddy diffusive mixing (Tab. A3). The large vertical exchange flux
8 between tropical surface and intermediate waters in the Indo-Pacific is thus supported by
9 intense Ekman driven upwelling and down-welling while wind-driven eddy diffusive mixing
10 explains most of the vertical exchange between surface and intermediate water boxes in the
11 North Atlantic, Southern Ocean and North Pacific. The overall vertical water exchange
12 across the 100 m water depth horizon (ca. 297 Sv, Tab. A3) is sufficiently high to ventilate
13 the global thermocline and to support a global rate of new and export production in the order
14 of 700 – 900 Tmol yr⁻¹. About 37 % of this vertical exchange flux occurs in the Southern
15 Ocean (> 30°S). The global bidirectional water flux across the 2000 m water depth level is
16 much lower (only 45 Sv, 44 % in the Southern Ocean) while the flux across the 4000 m line
17 amounts to ca. 179 Sv with a 74 % contribution by the Southern Ocean. The box model's
18 major internal boundary for vertical exchange is thus located at 2000 m water depth between
19 the thermocline and the underlying deep ocean.

20 In box modeling, water fluxes (F_{Wab}) are multiplied by tracer concentrations (C_j) to calculate
21 tracer fluxes (F_{Tab}) between adjacent boxes:

$$22 \quad F_{Tab} = C_a \cdot F_{Wab} \quad (A1)$$

23 where F_{Wab} and F_{Tab} are the water and tracer fluxes from box a to box b while C_a is the
24 concentration of the considered tracer in box a . The back fluxes from box b to box a are
25 defined correspondingly:

$$26 \quad F_{Tba} = C_b \cdot F_{Wba} \quad (A2)$$

27 Tracer fluxes arising from the water exchange fluxes listed in Tab. A3 (F_{Wex}) are thus
28 proportional to the concentration difference between adjacent boxes:

$$29 \quad F_{Tex} = (C_a - C_b) \cdot F_{Wex} \quad (A3)$$

30 These fluxes can be regarded as diffusion-analog mass transfer processes since their
31 magnitude is proportional to concentration differences rather than concentrations. In contrast,

1 the tracer fluxes arising from the net water fluxes in Tab. A3 are purely advective. Most box
 2 models apply unidirectional advective fluxes, only, and ignore diffusive bidirectional fluxes.
 3 Tracer distributions observed in the global ocean and simulated with general circulation
 4 models are, however, strongly affected by diffusive processes. With the inclusion of
 5 bidirectional fluxes in our box model set-up, we aim to better mimic this diffusive behavior.

6 The low spatial resolution of box models is problematic and may induce significant errors.
 7 For the box model set-up presented in this paper, the largest errors are associated with the
 8 upward fluxes from the thermocline into the surface ocean. Tracer concentrations calculated
 9 for the intermediate water boxes represent mean values averaged over the depth range 100 –
 10 2000 m where strong vertical gradients exist in the natural system. Due to these strong
 11 vertical gradients, the mean concentration values are not representative for the thermocline
 12 waters ascending across the 100 m water depth line. The standard box model approach where
 13 tracer fluxes are calculated applying the mean concentration in the source box (s. equations
 14 above) was, thus, abandoned for these specific fluxes and tracer fluxes were calculated as:

$$15 \quad F_{TIS} = C_{TH} \cdot F_{WIS} \quad (A4)$$

16 where F_{TIS} is the tracer flux from the intermediate water box to the overlying surface water
 17 box, F_{WIS} is the corresponding water flux, and C_{TH} is the tracer concentration in the upwelling
 18 thermocline water calculate as:

$$19 \quad C_{TH} = f_I \cdot C_I + (1 - f_I) \cdot C_S \quad (A5)$$

20 C_I is the concentration in the intermediate water box, C_S the concentration in the overlying
 21 surface water box and f_I defines the fraction of C_I in the ascending two component mixture.
 22 The weighing factor f_I was set to 0.5 for salinity, DIC, and ^{13}C -DIC. A smaller value was
 23 applied for total alkalinity ($f_I = 0.3$) to mimic the deeper regeneration of this tracer while
 24 larger values were applied for other tracers featuring steeper thermocline gradients (DP and
 25 DN: $f_I = 0.55$; DO: $f_I = 0.9$; ^{14}C -DIC: 0.7).

26 **A3 Salinity and surface temperatures**

27 Salinity (Sal) was treated as an inert tracer. The mass balance equations for Sal in each of the
 28 24 ocean boxes were thus simply defined as:

$$29 \quad \frac{\partial Vol \cdot Sal}{\partial t} = \sum F_{Sal-in} - \sum F_{Sal-out} \quad (A6)$$

1 where $F_{\text{Sal-in}}$ are the salinity fluxes from the neighboring boxes into the considered box while
2 $F_{\text{Sal-out}}$ gives the corresponding fluxes from the considered box into the adjacent boxes. The
3 volume of the considered box (Vol) was allowed to change over time to mimic the contraction
4 of the ocean volume during glacial sea-level low-stands. Fluxes were calculated as products
5 of water flux and salinity in the source box (Eq. A1 and Eq. A2) with the exception of
6 intermediate to surface water fluxes where thermocline concentrations were applied (Eq. A4
7 and A5). Surface water boxes were subject to evaporation and precipitation and received river
8 input from the continents. The fresh water fluxes listed in Tab. A3 represent the overall
9 budget of evapotranspiration and river water input. Negative fluxes thus indicate that
10 evaporation exceeds the sum of precipitation and river water input. Freshwater fluxes were
11 varied in the initial steady state simulations until the calculated salinity values were consistent
12 with observations. These simulations showed, however, that unrealistically high freshwater
13 fluxes were needed to reproduce the low salinity values observed in the Arctic Ocean surface
14 water box. This problem arises since the standard box model procedure demands that water
15 masses leaving the Arctic carry a chemical signature corresponding to the mean salinity value
16 integrated over the entire Arctic surface ocean. Observations show, however, that Arctic
17 surface waters sinking into the abyss are more salty than mean Arctic surface water. The
18 standard model procedure was, hence, modified to consider this characteristic feature of deep
19 water formation and to avoid unrealistically high freshwater fluxes to the Arctic surface
20 ocean, that is an enhanced salinity (+ 0.9 PSU with respect to the mean salinity of Arctic
21 surface water) was employed for the waters sinking into the underlying intermediate water
22 box.

23 Over a glacial cycle, surface temperatures are regulated by changes in, both, albedo and the
24 partial pressure of greenhouse gases. In the model it was assumed that 50 % of the
25 temperature change is proportional to the prescribed sea-level, that is continental ice sheet
26 formation and albedo change while the remaining 50 % are proportional to the logarithm of
27 atmospheric $p\text{CO}_2$ calculated as prognostic model variable. The global mean atmospheric
28 surface temperature was assumed to fall by 3°C during the glacial while the average sea
29 surface temperature (SST) was allowed to drop by ca. 2°C (Schmittner et al., 2011). The SST
30 drop was assumed to be twice as high as the global mean at high latitudes and only half as
31 high in the low latitude surface water boxes. Temperatures in intermediate and deep waters
32 were maintained at their modern values, for simplicity.

33 **A4 Phosphorus**

1 The model includes a comprehensive phosphorus cycle. Rivers transport dissolved
 2 phosphorus (DP) into the ocean where it is taken up by phytoplankton, gets exported,
 3 degraded, buried in marine sediments, and removed via hydrothermal activity (Wallmann,
 4 2014). Export production (F_{EPOP}) of particulate organic P (POP) from the individual surface
 5 water boxes across 100 m water depth was calculated applying Liebig's law:

$$6 \quad F_{EPOP} = k_{EXP} \cdot \text{Min} \left[DP_S \cdot \frac{DP_S}{DP_S + K_{DP}}, \frac{DN_S}{r_{NP}} \cdot \frac{DN_S}{DN_S + r_{NP} \cdot K_{DP}} \right] \cdot Vol_S \quad (A7)$$

7 POP export was thus limited either by dissolved reactive nitrogen (DN) or DP where K_{DP} is a
 8 Monod constant ($K_{DP} = 0.01 \mu\text{M}$), r_{NP} is the atomic N to P ratio in exported particulate
 9 organic matter ($r_{NP} = 17$; (Körtzinger et al., 2001)), Vol_S is the volume of the considered
 10 surface water box, and k_{EXP} is a site specific kinetic constant defined by fitting the model to
 11 DP concentrations observed in the modern surface ocean (Tab. A4). Most of the exported
 12 POP was degraded in the water column while a small but significant fraction was permanently
 13 buried in marine sediments (Appendix B). POP degradation in the water column (incl. the
 14 bioturbated surface layer of marine sediments) was distributed between intermediate (93 %),
 15 deep (6 %) and bottom water boxes (1 %). Export and degradation of particulate organic
 16 carbon (POC) and nitrogen (PON) and oxygen respiration were derived from the
 17 corresponding POP turnover applying constant Redfield ratios (PON/POP = 17, POC/PON =
 18 123/17, $O_2/POC = 1.34$ (Körtzinger et al., 2001)).

19 **A5 Nitrogen**

20 Nitrogen cycling was simulated considering export, degradation and burial of PON, nitrogen
 21 fixation, benthic and pelagic denitrification, and riverine fluxes of dissolved reactive nitrogen
 22 (DN). Nitrogen fixation in surface water boxes (F_{NF}) was calculated as:

$$23 \quad F_{NF} = k_{NF} \cdot DP_S \cdot \frac{DP_S}{DP_S + K_{DP}} \cdot \frac{r_{NP}}{r_{DNDPS}} \cdot Vol_S \quad (A8)$$

24 It was controlled by the ambient DP concentration and modulated by the DN/DP ratio in
 25 surface water (r_{DNDPS}) such that nitrogen fixation decreased when r_{DNDPS} exceeded the N/P
 26 ratio in exported biomass (r_{NP}) and vice versa. The biomass of nitrogen-fixing organisms was
 27 completely degraded in the surface ocean boxes and the organic nitrogen compounds were
 28 transformed into DN. Nitrogen fixation thus enhanced the DN pool in the surface ocean but
 29 did not contribute to export production. The kinetic constant for nitrogen fixation (k_{NF}) was

1 determined by fitting the model to the nitrate concentrations observed in the modern surface
2 ocean (Tab. A1 and Tab. A4).

3 Denitrification in the water column was limited to the intermediate water box of the Tropical
4 Indo-Pacific where the major oxygen minimum zones (OMZs) are located. It proceeded at a
5 constant rate of 5 Tmol yr⁻¹ (Deutsch et al., 2001). No attempt was made to simulate the
6 temporal evolution of water column denitrification since the box model did not resolve the
7 dynamics and spatial extent of OMZs. Benthic denitrification was calculated as function of
8 bottom water chemistry (nitrate and oxygen) and the rain rate of particulate organic carbon
9 (POC) to the seafloor (Appendix B) using an empirical transfer function (Bohlen et al., 2012).

10 **A6 Oxygen**

11 Oxygen was produced in the surface ocean via export production and consumed in the
12 ocean's interior by degradation of particulate organic matter. The oxygen exchange between
13 surface ocean and atmosphere was calculated as:

$$14 \quad F_{\text{DO}} = k_w \cdot A_{\text{SUR}} \cdot (\text{DO}_s - \text{DO}_{\text{SEQ}}) \quad (\text{A9})$$

Feldfunktion geändert

15 where k_w is piston velocity, A_{SUR} is the ice-free surface area of the considered box (Köhler et
16 al., 2005), DO_s is the concentration of DO in the considered surface water box while DO_{SEQ} is
17 the temperature-dependent equilibrium concentration of DO in surface water (García and
18 Gordon, 1992). The piston velocity was determined for each surface water box by fitting the
19 model to the observed $\Delta^{14}\text{C}$ values (Tab. A2 and Tab. A4). The deep ocean is ventilated by
20 cold and oxygen-enriched surface waters sinking into the ocean's interior at high latitudes
21 with a temperature of ca. -1.5°C. To mimic this process in the box model, the oxygen
22 concentration in downward flowing water masses was calculated applying a temperature of -
23 1.5°C rather than the significantly higher mean SSTs of North Atlantic and Southern Ocean
24 surface waters.

25 **A7 Carbon**

26 POC burial depended on export production and depositional area while neritic carbonate
27 burial was proportional to the shelf area at 0 – 50 m water depths (Appendix B). Export of
28 pelagic PIC (particulate inorganic carbon) was calculated from POC export production and
29 the PIC/POC export ratios which were derived by fitting the TA values in the surface ocean to
30 observations (Tab. A2 and A4). Exported PIC dissolved in intermediate water boxes until the
31 PIC/POC export ratio at 2000 m water depth reached a value of unity as observed in sediment
32 trap studies (Berelson et al., 2007; Honjo et al., 2008). Carbonate compensation was

1 implemented at >2000 m water depth where PIC dissolution was controlled by the carbonate
 2 ion concentrations calculated from TA and DIC values in deep and bottom water boxes
 3 (Wallmann, 2014). The remaining PIC was buried in pelagic sediments. The TA mass
 4 balance equations considered alkalinity production via denitrification and PON export
 5 production and alkalinity consumption via nitrogen fixation and PON degradation. The CO₂
 6 gas flux from the surface ocean into the atmosphere across the seawater/atmosphere boundary
 7 layer (F_{CO₂}) was calculated as (Sarmiento and Gruber, 2006):

$$8 \quad F_{\text{CO}_2} = k_w \cdot A_{\text{SUR}} \cdot (\text{CO}_{2\text{S}} - \text{CO}_{2\text{SEQ}}) \quad (\text{A10})$$

Feldfunktion geändert

9 where CO_{2S} is the concentration of CO₂ in the considered surface water box (as calculated
 10 from ambient DIC and TA), while CO_{2SEQ} is the equilibrium concentration of CO₂ in surface
 11 water (as calculated from atmospheric pCO₂). The thermodynamic equations included in the
 12 box model considered the effects of sea surface temperature (SST) and salinity on CO_{2SEQ} and
 13 CO_{2S} (Zeebe and Wolf-Gladrow, 2001). Constant rates were applied for on-shore volcanic
 14 and metamorphic degassing, degassing at mid-ocean ridges, alteration of oceanic crust, and
 15 silicate weathering (Wallmann, 2014). The rate of silicate weathering was set to a constant
 16 value since the weathering of exposed shelf sediments was assumed to compensate for the
 17 glacial decrease in silicate weathering in the continental hinterland (Munhoven, 2002). The
 18 rate of carbonate weathering was assumed to depend on surface temperature, run-off, and the
 19 size of the exposed shelf area (Wallmann, 2014). Riverine POC fluxes are ignored in the
 20 model. However, POC weathering is considered. It has two components: i) weathering of
 21 POC in exposed shelf sediments and ii) weathering of fossil POC in continental hinterland
 22 (Wallmann, 2014). Both components produce atmospheric CO₂ depleted in ¹³C and ¹⁴C.

23 **A8 Carbon isotopes**

24 The model includes ¹³C-DIC and ¹⁴C-DIC as tracers in addition to total DIC. Isotope ratios as
 25 well as δ¹³C and Δ¹⁴C values of DIC were calculated from ¹³C-DIC/DIC and ¹⁴C-DIC/DIC
 26 mole fractions. The gas exchange of ¹³C-CO₂ across the seawater/atmosphere boundary layer
 27 (F_{13CO₂}) was calculated as (Schmittner et al., 2013; Zhang et al., 1995):

$$28 \quad F_{13\text{CO}_2} = k_w \cdot A_{\text{SUR}} \cdot \alpha_{\text{aq-g}} \cdot \alpha_k \cdot \left(\frac{R_{13\text{DIC}}}{\alpha_{\text{DIC-g}}} \cdot \text{CO}_{2\text{S}} - R_{13\text{CO}_2\text{A}} \cdot \text{CO}_{2\text{SEQ}} \right) \quad (\text{A11})$$

Feldfunktion geändert

29 where α_{aq-g} is the equilibrium fractionation factor for CO₂ gas exchange between seawater
 30 and air, α_k is the corresponding kinetic fractionation factor, α_{DIC-g} is the equilibrium
 31 fractionation factor defining the ¹³C fractionation between DIC and gaseous CO₂, R_{13DIC} is the

1 $^{13}\text{C}/^{12}\text{C}$ ratio in DIC, and $R_{13\text{CO}_2\text{A}}$ is the $^{13}\text{C}/^{12}\text{C}$ ratio in atmospheric CO_2 . The isotopic
2 composition of DIC species (CO_2 , HCO_3^- , CO_3^{2-}) was calculated using equilibrium
3 fractionation factors given in (Zeebe and Wolf-Gladrow, 2001). These values were applied to
4 calculate the isotopic composition of exported POC and neritic and pelagic carbonates
5 applying isotopic fractionation factors according to (Ridgwell, 2001) and (Romanek et al.,
6 1992), respectively.

7 Fig. A3 shows the atmospheric $\delta^{13}\text{C}\text{-CO}_2$ record as calculated in our standard simulation.
8 According to this simulation and our previous studies (Sarnthein et al., 2013), the strong
9 negative $\delta^{13}\text{C}$ -excursion observed in the ice-core record was largely caused by deglacial
10 upwelling pulses in the Southern Ocean, though the amplitude of the simulated $\delta^{13}\text{C}\text{-CO}_2$
11 decline is much larger than that observed in the dataset (Schmitt et al., 2012). The trends of
12 our results and the empiric data are similar. The different extent of shift of the two records is
13 probably related to the poor representation of the ^{13}C -DIC turnover in the Southern Ocean in
14 our coarse-resolution model. We were not able to reproduce more closely the observed $\delta^{13}\text{C}$ -
15 DIC distribution in our model calibration even though a good fit was attained for all other
16 tracers (salinity, DIC, ^{14}C -DIC, alkalinity, phosphate, nitrate, oxygen, Fig. A1). Hence, we do
17 not conclude that this deviation for $\delta^{13}\text{C}\text{-CO}_2$ implies erroneous model results for all
18 remaining model variables. It rather reflects a specific weakness in the model set-up with
19 respect to the simulation of $\delta^{13}\text{C}$ -DIC in the Southern Ocean. Our model predicts a negative
20 value for intermediate waters in the modern Southern Ocean ($\delta^{13}\text{C}\text{-DIC} = -0.05 \text{ ‰}$) while
21 observations yield a positive value of $+0.72 \text{ ‰}$ for this ocean box (SO_1 in Tab. A2). Due to
22 this deviation the vertical gradient in the model exceeds the observed $\delta^{13}\text{C}$ gradient between
23 surface and intermediate waters by more than a factor of two. The glacial rise and deglacial
24 drop in $\delta^{13}\text{C}\text{-CO}_2$ are amplified by this model artefact. The deglacial intermediate water,
25 overly depleted in ^{13}C , upwells into the surface ocean where it induces a far too strong
26 atmospheric $\delta^{13}\text{C}\text{-CO}_2$ decline. Since the biased vertical $\delta^{13}\text{C}\text{-DIC}$ gradient in the Southern
27 Ocean impedes a meaningful simulation of atmospheric $\delta^{13}\text{C}\text{-CO}_2$, we tuned the $^{13}\text{C}\text{-CO}_2$
28 fluxes between the surface ocean and the atmosphere such that the resulting atmospheric
29 $\delta^{13}\text{C}\text{-CO}_2$ values were consistent with the ice-core record. By this way we effectively
30 employed the ice-core data to force the $\delta^{13}\text{C}\text{-DIC}$ model (Fig. 4f). The $\delta^{13}\text{C}$ values of
31 intermediate, deep and bottom water boxes employed to derive the glacial circulation field
32 (Tab. A5) were not significantly affected by this tuning since the inventory of ^{13}C residing in
33 the global ocean exceeds the atmospheric inventory by almost two orders of magnitude.

1 The $^{14}\text{C}/^{12}\text{C}$ fractionation between DIC, CO_2 , POC and CaCO_3 was calculated using the
 2 squared ^{13}C equilibrium fractionation factors since the mass difference between ^{14}C and ^{12}C
 3 exceeds the $^{13}\text{C} - ^{12}\text{C}$ difference by a factor of 2. The gas exchange of $^{14}\text{C}\text{-CO}_2$ across the
 4 seawater/atmosphere boundary layer ($F_{14\text{CO}_2}$) was thus calculated as:

$$5 \quad F_{14\text{CO}_2} = k_w \cdot A_{\text{SUR}} \cdot \alpha_{\text{aq-g}}^2 \cdot \alpha_k \cdot \left(\frac{R_{14\text{DIC}}}{\alpha_{\text{DIC-g}}^2} \cdot \text{CO}_{2\text{S}} - R_{14\text{CO}_2\text{A}} \cdot \text{CO}_{2\text{SEQ}} \right) \quad (\text{A12})$$

Feldfunktion geändert

6 where $R_{14\text{DIC}}$ is the $^{14}\text{C}/^{12}\text{C}$ ratio in DIC of the considered surface water box and $R_{14\text{CO}_2\text{A}}$ the
 7 $^{14}\text{C}/^{12}\text{C}$ ratio in atmospheric CO_2 . Moreover, $^{14}\text{C}\text{-DIC}$ was subject to radioactive decay with a
 8 decay constant of $\lambda = 1/8267 \text{ yr}^{-1}$.

9 $\Delta^{14}\text{C}\text{-DIC}$ values were calculated as:

$$10 \quad \Delta^{14}\text{C} - \text{DIC} = \left(\frac{f_N \cdot \Phi_{14\text{DIC}}}{\Phi_{\text{abs}}} - 1 \right) \cdot 1000 \quad (\text{A13})$$

11 where $\Phi_{14\text{DIC}}$ is the ^{14}C mole fraction ($\Phi_{14\text{DIC}} = ^{14}\text{C}\text{-DIC}/\text{DIC}$), Φ_{abs} is the ^{14}C mole fraction of
 12 the standard (1.175×10^{-12} (Mook and Plicht, 1999), pre-human atmosphere with a $\delta^{13}\text{C}$ value
 13 of -25 ‰), f_N is the normalization factor defined as:

$$14 \quad f_N = \left(\frac{0.975}{\left(1 + \frac{\delta^{13}\text{C}}{1000} \right)} \right)^2 \quad (\text{A14})$$

15 and $\delta^{13}\text{C}$ is the $\delta^{13}\text{C}$ value of DIC in the considered box in ‰ PDB. The isotopic
 16 fractionation experienced by the considered DIC pool was thus taken into account in the
 17 calculation of marine $\Delta^{14}\text{C}\text{-DIC}$ values by applying the $\delta^{13}\text{C}\text{-DIC}$ calculated for the
 18 considered ocean box (Stuiver and Polach, 1977).

19 ~~The isotopic compositions of atmospheric CO_2 were not calculated as prognostic model~~
 20 ~~variables but prescribed using data from the geological record. Ice core data were applied to~~
 21 ~~define the $\delta^{13}\text{C}\text{-CO}_2$ values (Schmitt et al., 2012) while $\Delta^{14}\text{C}\text{-CO}_2$ values were forced to~~
 22 ~~follow the IntCal13 values (Reimer et al., 2013). The atmospheric records are affected by~~
 23 ~~vertical mixing processes in the Southern Ocean and the distribution of SSTs and vertical $\delta^{13}\text{C}$~~
 24 ~~and $\Delta^{14}\text{C}$ gradients within this region (Schmitt et al., 2012; Tschumi et al., 2011b; Köhler et~~
 25 ~~al., 2005). Sediment records show an anti-phased pattern in export production and vertical~~
 26 ~~mixing between the region south of the Antarctic Polar Front and the Subantarctic Ocean~~

~~(Anderson et al., 2014) which may have a strong effect on atmospheric isotope values but was not resolved by our model since the entire global surface ocean at >30°S was pooled in a single box (Fig. 2). This lack of resolution hindered us to simulate the carbon isotopic composition of atmospheric pCO₂ with our box model. Sensitivity tests showed that the δ¹³C values of intermediate, deep and bottom water boxes employed to derive the glacial circulation field (Tab. A5) were not significantly affected by the prescribed atmospheric δ¹³C values since the inventory of ¹³C residing in the global ocean exceeds the atmospheric inventory by almost two orders of magnitude.~~

The time-dependent radiocarbon production rate in the atmosphere (R₁₄) was calculated applying the following equation:

$$R_{14} = k_{14} (\Delta^{14}\text{C-CO}_2 (\text{data}) - \Delta^{14}\text{C-CO}_2 (\text{model})) \quad (\text{A15})$$

where k_{14} is a constant ($\geq 10^5 \text{ mmol yr}^{-1} \text{ ‰}^{-1}$), $\Delta^{14}\text{C-CO}_2 (\text{model})$ is the atmospheric value calculated for each time step of the model, and $\Delta^{14}\text{C-CO}_2 (\text{data})$ is the data trend reconstructed from the geological record (Reimer et al., 2013). R_{14} thus increased when $\Delta^{14}\text{C-CO}_2 (\text{model})$ was smaller than $\Delta^{14}\text{C-CO}_2 (\text{data})$ and vice versa. With this approach, the production rate was varied such that the model always complied with the atmospheric ¹⁴C record. The atmospheric radiocarbon model considered production and the decay of radiocarbon in the atmosphere as well as exchange processes with the continents and the surface ocean (Eq. A12). The major output of the atmospheric ¹⁴C model was the time-dependent ¹⁴C production rate (Eq. A15).

Appendix B: Impact of sea-level change on benthic processes at continental margins

B1 Particulate organic carbon (POC) turnover

The overwhelming portion of POC produced in the euphotic zone is degraded in the water column before it can reach the seabed. Hence, in the open ocean, only ca. 1 % of the primary production ~~reaches-is deposited at~~ the deep-sea floor (Suess, 1980; Jahnke, 1996; Seiter et al., 2005; Dunne et al., 2007). However, the fraction reaching the seabed increases drastically at continental margins where shallow water depths limit the transit time of POC sinking through the water column. Global models and observations thus indicate that ca. 30 % of ambient primary production reaches the shallow seafloor at 0 – 50 m water depth (Dunne et al., 2007). Due to this effect and the high productivity of continental margins, the margin seabed located

1 at <2 km water depths receives ca. 85 ± 15 % of the global POC rain rate (Dunne et al., 2007;
2 Burdige, 2007) even though only 16 % of the global seabed is located at <2km water depth
3 (Eakins and Sharman, 2012). Continental margins are even more dominant in terms of POC
4 burial because burial is promoted by the deposition of riverine particles (Berner, 1982, 2004)
5 accumulating mostly on the continental shelf during interglacial sea-level high-stands
6 (Burwicz et al., 2011). Thus, 90 ± 10 % of the global POC burial takes place at <2 km water
7 depth (Dunne et al., 2007; Burdige, 2007; Wallmann et al., 2012).

8 POC rain and burial rates at continental margins declined during glacial sea-level low-stands
9 since the oceans retreated into steeper terrains. During the LGM when the sea-level was 120
10 m lower than today, the shelf seafloor area at 0 - 100 m contracted by 73 % while the outer
11 shelf and upper slope area located at 100 - 2000 m water depth was reduced by 13 % (Eakins
12 and Sharman, 2012) neglecting isostatic adjustment. Considering the high rain rates at
13 shallow water depths (Dunne et al., 2007), the glacial margin contraction diminished the
14 global POC rain rate by possibly up to 50 %. The burial rate of marine POC may have been
15 reduced by a similar proportion since POC burial is ultimately limited by the amount of POC
16 reaching the seabed. However, there are a number of additional factors that affect the rate of
17 POC burial. These include bulk sedimentation rate (Berner, 1982), surface area of sediment
18 particles (Mayer et al., 2004), oxygen exposure time (Hartnett et al., 1998), and the re-
19 suspension and down-slope transport of shelf POC promoting POC burial at the upper slope
20 (Walsh et al., 1981; Dale et al., 2015). These secondary processes control the burial efficiency
21 of POC, that is the ratio between POC burial and POC rain rate.

22 POC burial efficiency is to a large degree controlled by sedimentation processes on the shelf
23 that are strongly affected by sea-level change. At high sea-level most of the riverine particle
24 load is deposited on the shelf (Burwicz et al., 2011) while low sea-level stands promote down-
25 slope transport (Hay and Southam, 1977). Hence, data on Quaternary shelf and deep-sea fan
26 sedimentation clearly show that the riverine particle flux was discharged over the shelf edge
27 onto deep-sea fans and abyssal plains by turbidity currents over most of the glacial period
28 (Hay and Southam, 1977; Hay, 1994; Schlünz et al., 1999). The corresponding increase in
29 sedimentation rate probably led to a rise in burial efficiency and POC burial at >2km water
30 depths (Burwicz et al., 2011; Wallmann, 2014). The efficiency of POC burial at the
31 continental rise and deep-sea floor may have been further amplified by the glacial decline in
32 dissolved oxygen concentrations in the deep ocean (Jaccard and Galbraith, 2012) favoring the
33 preservation of POC in marine sediments (Hartnett et al., 1998; Dale et al., 2015). It is

1 difficult to validate glacial changes in burial efficiency at <2km water depths. Here, POC
2 preservation was possibly reduced by the intense ventilation of the glacial thermocline
3 (Jaccard and Galbraith, 2012) while preservation might have been enhanced if sedimentation
4 rates on the outer shelf and upper slope were significantly elevated by the glacial loss of inner
5 shelf regions. Considering the available evidence it can be concluded that the glacial marine
6 regression induced a strong decline in POC burial on the continental shelf while POC burial
7 was enhanced at the continental rise and deep-sea floor. The overall effect was an increase in
8 water column degradation and decline in marine POC burial since the focus of POC burial
9 was shifted to >2km water depth where rain and burial rates are limited by the almost
10 complete degradation of marine POC in the water column.

11 **B2 Nutrient turnover**

12 Continental margins are also major sinks for nitrate and phosphate since >50 % of the global
13 benthic denitrification and burial of marine phosphorus occur in sediments deposited at <2km
14 water depth (Bohlen et al., 2012; Archer et al., 2002; Froelich et al., 1982; Baturin and
15 Savenko, 1997; Wallmann, 2010; Middelburg et al., 1996). These fluxes are driven by the rain
16 of marine POM to the seabed which is focused on shallow water environments (Dunne et al.,
17 2007). The strong decrease in shallow seafloor area during glacial marine regressions thus
18 induced a decline in nitrate and phosphate removal contributing to the expansion of the
19 nutrient inventory in the glacial ocean (Broecker, 1982a; Deutsch et al., 2004; Eugster et al.,
20 2013; Wallmann, 2014). A negative feedback was probably established where the expansion
21 of the nutrient inventory induced a rise in export production and rain rate to the seabed which
22 in turn promoted the burial of POC and removal of nutrients from the ocean. The glacial
23 decline in POC burial and the glacial rise in the standing stocks of macronutrients may have
24 been mitigated by this negative feedback mechanism (Middelburg et al., 1996).

25 Phosphate cycling in marine sediments is affected by oxygen conditions in ambient bottom
26 waters and sediments (Krom and Berner, 1981; Van Cappellen and Ingall, 1994; Wallmann,
27 2003). Phosphate is released from sediments under suboxic and anoxic conditions due to the
28 reduction of iron and manganese oxides and the preferential degradation of P-bearing organic
29 matter (POP). However, a large fraction of the released phosphate is precipitated and retained
30 in the sediment as authigenic carbonate fluorapatite (CFA). Hence, OMZ sediments are
31 depleted in Fe/Mn-bound P, enriched in CFA and characterized by high POC/POP ratios
32 exceeding the Redfield ratio by a factor of 2 – 8 (Schenau and De Lange, 2001; Lomnitz et
33 al., 2015). Ratios between POC and reactive P (P_{react} , sum of POP, CFA and Fe/Mn-bound P)

1 amount to $POC/P_{\text{reac}} = 100 - 300$ in OMZ sediments and 20 - 70 in continental margin
2 sediments underlying oxygenated bottom waters (Schenau and De Lange, 2001; Noffke et al.,
3 2012). Hence, the burial efficiency of reactive P and total P is reduced under low oxygen
4 conditions (Ingall and Jahnke, 1994; Schenau and De Lange, 2001) whereas POC is more
5 efficiently buried in OMZ sediments covered by oxygen-depleted bottom waters (Dale et al.,
6 2015).

7 **B3 Equations and parameter values employed to simulate carbon and nutrient turnover**

8 The parameterization of margin processes applied in the model is summarized in Tables B1
9 and B2. A very simple approach was chosen to calculate the burial of neritic carbonates. It
10 was assumed that the burial rate is proportional to the seafloor area at 0 - 50 m water depth
11 (A_{NM}) which is controlled by sea-level change, only (see Fig. 3). Burial of marine POC and
12 phosphorus (P) at continental margins was assumed to be proportional to POC export
13 production (F_{EPOC}) and the depositional areas at 0 – 100 m (A_{S}) and 100 – 2000 m (A_{I}) that
14 were controlled by sea-level change (Fig. 3). The decline in seafloor area at 0 – 2000 m water
15 depths was applied to parameterize the rise in POC burial at the deep-sea floor induced by the
16 glacial marine regression. We thus effectively assumed that the burial efficiency of POC
17 remained constant at <2km water depth but increased at >2km during glacial sea-level low-
18 stands.

19 Phosphorus considered in the model refers to the sum of organic and reactive inorganic P
20 phases (CFA and Fe/Mn-bound P). The latter fractions contribute strongly to P burial since
21 most of the marine particulate P deposited at the seafloor is degraded and transformed into
22 inorganic authigenic phases during early diagenesis (Ruttenberg and Berner, 1993). P burial
23 decreases when the dissolved oxygen content of ambient bottom waters (DO) falls below a
24 threshold value of about 20 μM (Wallmann, 2010). This effect was taken into account by
25 introducing corresponding Monod terms in the P burial flux definitions (Tab. B2). Moreover,
26 the model formulation ensured that the molar POC/P_{reac} burial ratio did not exceed the
27 maximum value of about 400 observed in Quaternary sediments (Anderson et al., 2001).

28 Benthic denitrification was calculated from the POC rain rate and ambient dissolved oxygen
29 and nitrate concentrations (DN) applying an empirical transfer function calibrated by in-situ
30 benthic flux data (Bohlen et al., 2012). The rain rates needed for this function were derived
31 from POC burial rates using the corresponding burial efficiencies. Marine PON burial was
32 calculated from POC burial applying a molar PON/POC ratio of 17/123 (Körtzinger et al.,
33 2001).

1 In contrast to previous sediment models (Heinze et al., 1999; Gehlen et al., 2006), our model
2 does not resolve transport processes and reactions within surface sediments. We prefer to
3 employ observational data on POC and P burial and empirical transfer functions to constrain
4 benthic turnover rates (Bohlen et al., 2012; Wallmann, 2010) because most depth-resolving
5 transport-reaction models yield results that are not yet consistent with key data such as
6 benthic oxygen and nitrate fluxes and POC burial rates (Stolpovsky et al., 2015).

7 The applied parameter values were constrained by field data from the modern ocean (Tab.
8 B1). The available POC and P burial data suggest that burial is rather evenly distributed
9 between 0 - 100 m and 100 - 2000 m water depths (Tab. B1) whereas POM rain rates at 0 –
10 100 m clearly exceed the corresponding rates at 100 – 2000 m (Dunne et al., 2007). This
11 difference is caused by bottom currents transporting marine POM from the inner shelf
12 towards outer shelf and upper slope environments (Walsh et al., 1981). Note that the POC
13 burial rates applied in our model (Tab. B1) are conservative that is lower than most previous
14 estimates (Burdige, 2007; Dunne et al., 2007). The burial efficiency applied in the model is
15 low at shallow water depth since winnowing by bottom currents affects large parts of the
16 shallow seafloor such that about 70 % of the modern shelf sediments are non-accumulating,
17 relict sands with very low POC contents (Burdige, 2007). POM exported laterally from these
18 shallow areas provides POM for slope deposits (Walsh et al., 1981). The highest burial
19 efficiency is applied at 100 – 2000 m water depth where the deposition of fine-grained
20 riverine particles and low oxygen values in ambient bottom waters favor the preservation of
21 marine POC. Parameter values and fluxes listed in Tabs. B1 and B2 refer to global fluxes.
22 These fluxes were distributed among the 6 ocean basins defined in the box model considering
23 the respective seafloor areas and export productions. Neritic carbonate burial was distributed
24 between the Tropical Indo-Pacific and Atlantic (Kleypas, 1997).

25 Our model predicts that the global burial rates of POC and P would decline to 7.9 Tmol yr^{-1}
26 and $0.14 \text{ Tmol yr}^{-1}$ during the LGM, respectively, if export production and oxygen
27 concentrations were maintained at their modern value. The export production was, however,
28 promoted by the decline in P burial such that the best fit simulation STD produced LGM
29 burial rates of 9.6 Tmol yr^{-1} and $0.165 \text{ Tmol yr}^{-1}$ compared to modern global rates of 11.5
30 Tmol yr^{-1} and $0.18 \text{ Tmol yr}^{-1}$, respectively (s. Tab. B1). Our standard model run suggests that
31 the shelf (0 – 100 m water depths) trapped a total of 4650 Gt POC over the last glacial cycle
32 (130 – 0 ka) while 7870 Gt POC accumulated on the continental slope (100 – 2000 m water
33 depth). Shelf weathering released a total of 1940 GtC over the last 130 ka in simulation STD

1 that is less than 50 % of the POC accumulating on the shelf over the last glacial cycle.
2 According to the model, the glacial marine regression affected the chemical and isotopic
3 composition of seawater and the CO₂ content of the atmosphere via a chain of interconnected
4 processes: Ocean margins retreated into steeper terrain and shelf areas were exposed by the
5 marine regression; the burial of phosphorus and neritic carbonate and benthic denitrification
6 declined due to the steepening of ocean margins; carbonate, POC, and P weathering rates
7 increased due to the exposure of shelf sediments; atmospheric CO₂ was consumed and
8 converted into dissolved alkalinity by enhanced carbonate weathering while isotopically
9 depleted CO₂ was released into the atmosphere by POC weathering; standing stocks of
10 dissolved nutrients and alkalinity in the ocean expanded due to the decrease in burial and
11 denitrification and the increase in weathering; export production rose due to the increase in
12 the dissolved nutrient stocks and CO₂ was transferred from the atmosphere into the ocean
13 interior by the intensified biological pump while CO₂ sequestration was supported by
14 enhanced seawater alkalinity.

15 **B4 Model limitations**

16 Model parameterizations were chosen to the best of our knowledge. It should, however, be
17 noted that key processes such as glacial changes in POC and P burial efficiency are only
18 poorly constrained by available data. Moreover, we assumed that the global mean
19 morphology of continental margins was retained over the glacial cycle and that the average
20 global change in relative sea-level was equal to eustatic sea-level change. This approach
21 neglects the glacial isostatic adjustment, i.e. the glacial subsidence of northern land masses
22 loaded by large ice sheets, the uplift in flanking regions, and the numerous far field effects
23 (Daly, 1934; Milne and Mitrovica, 2008). It also neglects changes in margin morphology
24 induced by the erosion and down-slope transport of shelf sediments during glacial sea-level
25 low-stands (Hay, 1994) and the deglacial tilting of continental margins (Clark et al., 1978).
26 Moreover, we assumed that during the LGM eustatic sea-level was 120 m lower than today
27 while growing evidence supports the view that LGM sea-level fall was in fact larger than this
28 consensus value (Austermann et al., 2013; Lambeck et al., 2014). The changes in the size of
29 depositional and exposed areas at continental margins applied in the model should thus be
30 regarded as rough estimates. Clearly, more work needs to be done to improve these estimates.
31 However, there is no doubt that ocean margins retreated into steeper terrain while large shelf
32 areas were exposed during glacial marine regressions and that these changes had a profound
33 effect on glacial seawater composition and atmospheric pCO₂.

1 Moreover, our model does not consider the growth of land plants and soil formation on
 2 emerged shelf regions during glacial sea-level low-stands. Trees and other plants may use
 3 sediment nutrients after shelf exposure and accumulate terrestrial POC on the emerged shelf.
 4 However, we think that the POC accumulation associated with these processes is small
 5 compared to the sedimentary POC turnover considered in the model. Modern continental
 6 margins (shelf and rise) accumulate sedimentary POC at a rate of about 100 - 200 Gt kyr⁻¹
 7 (Hedges and Keil, 1995; Burdige, 2007; Wallmann et al., 2012; Dunne et al., 2007). This
 8 enormous flux is induced by the high marine productivity of the region and the rapid
 9 accumulation of sediments facilitating the burial of marine POC. Trees and soils growing on
 10 the emerged shelf would have to accumulate POC in the order of 10 000 Gt C to maintain this
 11 high carbon flux over the glacial period (ca. 80 kyr), an unlikely scenario since the global
 12 terrestrial carbon stock is ≤2000 GtC. The standing stock of POC in margin sediments
 13 exceeds the global terrestrial stock since POC is buried more efficiently in sediments than in
 14 most soils and plants. Sedimentary POC burial and preservation are promoted by high
 15 sedimentation rates and the lack of oxygen in these water-saturated deposits.

16

17 **Appendix C: Model results**

18 Key model results are listed in Tabs. C1 to C4 and compared to proxy data where available.

19

20 **Appendix D: Radiocarbon model**

21 A simple two-box-model helps to explain why the ocean is strongly depleted in radiocarbon
 22 with respect to the atmosphere when radiocarbon production rates are high. In this model,
 23 radiocarbon is produced in the atmosphere and transferred from the atmosphere to the ocean
 24 by a diffusion-analog process. It decays both in the atmosphere and in the ocean. At steady
 25 state, this simple system can be represented by the following set of equations:

$$26 \text{ Atmosphere mass balance: } R_{14} - \lambda \, {}^{14}\text{C}_A - F_{AO} = 0 \quad (\text{D1})$$

$$27 \text{ Ocean mass balance: } F_{AO} - \lambda \, {}^{14}\text{C}_O = 0 \quad (\text{D2})$$

$$28 \text{ }^{14}\text{C flux from atmosphere to ocean: } F_{AO} = k ({}^{14}\text{C}_A - {}^{14}\text{C}_O) \quad (\text{D3})$$

29 where R_{14} is the radiocarbon production rate, λ is the decay constant, ${}^{14}\text{C}_A$ is the radiocarbon
 30 mass in the atmosphere, ${}^{14}\text{C}_O$ is the radiocarbon mass in the ocean, and k is a mass transfer

1 coefficient. Equations C1 – C3 can be combined and solved for the radiocarbon difference
2 between atmosphere and ocean:

$$3 \quad {}^{14}\text{C}_A - {}^{14}\text{C}_O = \frac{R_{14}}{\lambda + 2 \cdot k} \quad (\text{D4})$$

4 The resulting equation shows that the difference is proportional to the radiocarbon production
5 rate. The steady-state ^{14}C -depletion of the ocean with respect to the atmosphere, thus,
6 increases under high production rates. The difference would vanish if the mass transport
7 coefficient would be infinitely large. The example of the modern ocean shows, however, that
8 this is not the case and that the ocean is significantly depleted in ^{14}C with respect to the
9 atmosphere since the transfer of ^{14}C from the atmosphere into the ocean is too slow to
10 eliminate the ^{14}C difference. In our simple 2-box model, the radiocarbon flux is assumed to be
11 proportional to the radiocarbon gradient between atmosphere and ocean (Eq. D3). The
12 gradient increases under high production rates such that more ^{14}C is transferred from the ^{14}C -
13 enriched atmosphere into the depleted ocean. The rate of radioactive decay in the ocean (λ
14 $^{14}\text{C}_O$) increases since the ^{14}C content of the ocean is raised by the enhanced radiocarbon flux
15 from the atmosphere. Steady state is attained when the decay rate in the ocean and the ^{14}C
16 flux from the atmosphere are balanced (Eq. D2). The steady-state gradient ($^{14}\text{C}_A - ^{14}\text{C}_O$), thus,
17 increases in proportion to the atmospheric production rate such that the flux into the ocean
18 compensates for the elevated decay rate in the ocean. The analytical solution for the simple
19 two-box-model (Eq. D4) correctly predicts the steady-state behavior of our more evolved
20 model system where the ocean is represented by 24 boxes and the radiocarbon uptake from
21 the atmosphere is calculated applying Eq. (A12) rather than Eq. (D3). It predicts that $\Delta\Delta^{14}\text{C}$ -
22 DIC increases linearly with production rate as observed in the steady state simulations (Tab.
23 C2). The real ocean-atmosphere system is obviously more complex than any kind of model.
24 However, the simple 2-box-model captures the basic features of the real system and reveals
25 that the ^{14}C contrast increases in proportion to the production rate. Since radiocarbon
26 production rates may have changed significantly over the last glacial cycle, this basic system
27 property has to be considered in the interpretation of the marine ^{14}C -record.

28

29 **Acknowledgements**

30 This work was funded by the DFG via the collaborative project SFB 754. The manuscript was
31 greatly improved in the review process thanks to the very helpful comments by the two
32 reviewers (Victor Brovkin and anonymous) and the associated editor (Luke Skinner).

1

2 **References**

3 Abe-Ouchi, A., Saito, F., Kawamura, K., Raymo, M. E., Okuno, J., Takahashi, K., and
4 Blatter, H.: Insolation-driven 100,000-year glacial cycles and hysteresis of ice-sheet volume,
5 *Nature*, 500, 190-193, 10.1038/nature12374, 2013.

6 Adkins, J. F., and Boyle, E. A.: Changing atmospheric $\Delta^{14}\text{C}$ and the record of deep water
7 paleoventilation ages, *Paleoceanography*, 12, 337-344, 1997.

8 Altabet, M. A., Francois, R., Murray, D. W., and Prell, W. L.: Climate-related variations in
9 denitrification in the Arabian Sea from sediment $^{15}\text{N}/^{14}\text{N}$ ratios, *Nature*, 373, 506-509, 1995.

10 Anderson, L. D., Delaney, M. L., and Faul, K. L.: Carbon to phosphorus ratios in sediments:
11 Implications for nutrient cycling, *Global Biogeochemical Cycles*, 15, 65-79, 2001.

12 Anderson, R. F., Ali, S., Bradtmiller, L. I., Nielsen, S. H. H., Fleisher, M. Q., Anderson, B.
13 E., and Burckle, L. H.: Wind-driven upwelling in the Southern Ocean and the deglacial rise in
14 atmospheric CO_2 , *Science*, 323, 1443-1448, 2009.

15 Anderson, R. F., Barker, S., Fleisher, M., Gersonde, R., Goldstein, S. L., Kuhn, G., Mortyn,
16 P. G., Pahnke, K., and Sachs, J. P.: Biological response to millennial variability of dust and
17 nutrient supply in the Subantarctic South Atlantic Ocean, *Phil. Trans. R. Soc. A* 372,
18 20130054, 2014.

19 Archer, D. E., Morford, J. L., and Emerson, S. R.: A model of suboxic sedimentary diagenesis
20 suitable for automatic tuning and gridded global domains, *Global Biogeochemical Cycles*, 16,
21 10.1029/2000GB001288, 2002.

22 Aumont, O., and Bopp, L.: Globalizing results from ocean in situ iron fertilization studies,
23 *Global Biogeochem. Cycles*, 20, GB2017, doi:10.1029/2005GB002591, 2006.

24 Austermann, J., Mitrovica, J. X., Latychev, K., and Milne, G. A.: Barbados-based estimate of
25 ice volume at Last Glacial Maximum affected by subducted plate, *Nature Geoscience*, 6, 553-
26 557, 2013.

27 Barker, S., Knorr, G., Vautravers, M. J., Diz, P., and Skinner, L. C.: Extreme deepening of the
28 Atlantic overturning circulation during deglaciation, *Nature Geoscience*, 3, 567-571, 2010.

- 1 Baturin, G. N., and Savenko, V. S.: Phosphorus in oceanic sedimentogenesis, *Oceanology*, 37,
2 107-113, 1997.
- 3 Baturin, G. N.: Issue of the relationship between primary productivity of organic carbon in
4 ocean and phosphate accumulation (Holocene - Late Jurassic), *Lithology and Mineral*
5 *Resources*, 42, 318-348, 2007.
- 6 Berelson, W. E., Balch, W. M., Najjar, R., Feely, R. A., Sabine, C., and Lee, K.: Relating
7 estimates of CaCO₃ production, export, and dissolution in the water column to measurements
8 of CaCO₃ rain into sediment traps and dissolution on the sea floor: A revised global carbonate
9 budget, *Global Biogeochem. Cycles*, 21, doi:10.1029/2006GB002803, 2007.
- 10 Berger, A., and Loutre, M. F.: Insolation values for the climate of the last 10 Million years,
11 *Quaternary Science Reviews*, 10, 297-317, 1991.
- 12 Berger, W. H.: Increase of carbon dioxide in the atmosphere during deglaciation: The coral
13 reef hypothesis, *Naturwissenschaften*, 69, 87-88, 1982.
- 14 Berner, R. A.: Burial of organic carbon and pyrite sulfur in the modern ocean: Its geochemical
15 and environmental significance, *American Journal of Science*, 282, 451-473, 1982.
- 16 Berner, R. A., and Rao, J.-J.: Phosphorus in sediments of the Amazon River and estuary:
17 Implications for the global flux of phosphorus to the sea, *Geochimica et Cosmochimica Acta*,
18 58, 2333-2339, 1994.
- 19 Berner, R. A.: *The Phanerozoic Carbon Cycle: CO₂ and O₂*, Oxford University Press, Oxford,
20 150 pp., 2004.
- 21 Bohlen, L., Dale, A., and Wallmann, K.: Simple transfer functions for calculating benthic
22 fixed nitrogen losses and C:N:P regeneration ratios in global biogeochemical models *Global*
23 *Biochemical Cycles*, 26, 10.1029/2011GB004198, 2012.
- 24 Bordelon-Katrynski, L. A., and Schneider, B.: Modeled CO₂ feedbacks from increased
25 phytoplankton DOC exudation, *Biogeosciences Discussions*, 9, 1-29, 2012.
- 26 Boyle, E. A., and Keigwin, L. D.: Deep circulation of the North Atlantic over the last 200,000
27 years: Geochemical evidence, *Science*, 218, 784-787, 1982.

- 1 Broecker, W. S.: Ocean chemistry during glacial time, *Geochimica et Cosmochimica Acta*,
2 46, 1689-1705, 1982a.
- 3 Broecker, W. S.: Glacial to interglacial changes in ocean chemistry, *Prog. Oceanogr.*, 11, 151-
4 197, 1982b.
- 5 Broecker, W. S.: The great ocean conveyor, *Oceanography*, 4, 79-90, 1991.
- 6 Broecker, W. S., Peacock, S. L., Walker, S., Weiss, R., Fahrbach, E., Schroeder, M.,
7 Mikolajewic, U., Heinze, C., Key, R., Peng, T.-H., and Rubin, S.: How much deep water is
8 formed in the Southern Ocean?, *Journal of Geophysical Research*, 103, 15833-15843, 1998.
- 9 Broecker, W. S., Clark, E., Hajdas, I., and Bonani, G.: Glacial ventilation rates for the deep
10 Pacific Ocean, *Paleoceanography*, 19, 10.1029/2003PA000974, 2004.
- 11 Brovkin, V., Ganopolski, A., Archer, D., and Munhoven, G.: Glacial CO₂ cycle as a
12 succession of key physical and biogeochemical processes, *Clim. Past*, 8, 251–264, 2012.
- 13 Brovkin, V., and Ganopolski, A.: The role of the terrestrial biosphere in CLIMBER-2
14 simulations of the last 4 glacial CO₂ cycles, *Nova Acta Leopoldina NF*, 121, 43-47, 2015.
- 15 Bryan, S. P., Marchitto, T. M., and Lehman, S. J.: The release of ¹⁴C-depleted carbon from the
16 deep ocean during the last deglaciation: Evidence from the Arabian Sea, *Earth and Planetary
17 Science Letters*, 298, 244-254, 2010.
- 18 Burdige, D. J.: Preservation of organic matter in marine sediments: Controls, mechanisms,
19 and an imbalance in sediment organic carbon budgets?, *Chem. Rev.*, 107, 467-485, 2007.
- 20 Burke, W. H., Denison, R. E., Hetherington, E. A., Koepnick, R. B., Nelson, H. F., and Otto,
21 J. B.: Variation of seawater ⁸⁷Sr/⁸⁶Sr throughout Phanerozoic time, *Geology*, 10, 516-519,
22 1982.
- 23 Burwicz, E. B., Rüpke, L. H., and Wallmann, K.: Estimation of the global amount of
24 submarine gas hydrates formed via microbial methane formation based on numerical reaction-
25 transport modeling and a novel parameterization of Holocene sedimentation, *Geochim.
26 Cosmochim. Acta*, 75, 4562-4576, 2011.
- 27 Clark, J. A., Farrell, W. E., and Peltier, W. R.: Global changes in postglacial sea level: A
28 numerical calculation, *Quaternary Science Reviews*, 9, 265-287, 1978.

1 Conkright, M. E., Locarnini, R. A., Garcia, H. E., O'Brien, T. D., Boyer, T. P., Stephens, C.,
2 and J. I. Antonov: World Ocean Atlas 2001: Objective Analyses, Data Statistics, and Figures,
3 National Oceanographic Data Center, Silver Spring, MD, 17, 2002.

4 Curry, W. B., and Oppo, D. W.: Glacial water mass geometry and the distribution of $d^{13}C$ of
5 SCO_2 in the western Atlantic Ocean, *Paleoceanography*, 20, 10.1029/2004PA001021, 2005.

6 Dale, A. W., Sommer, S., Lomnitz, U., Montes, I., Treude, T., Liebetrau, V., Gier, J., Hensen,
7 C., Dengler, M., Stolpovsky, K., Bryant, L. D., and Wallmann, K.: Organic carbon
8 production, mineralisation and preservation on the Peruvian margin, *Biogeosciences*, 12,
9 1537-1559, 2015.

10 Daly, R. A.: *The Changing World of the Ice Age*, Yale University Press, New Haven, 1934.

11 Denton, G. H., Anderson, R. F., Toggweiler, J. R., Edwards, R. L., Schaefer, J. M., and
12 Putnam, A. E.: The Last Glacial Termination, *Science*, 328, 1652-1656, 2010.

13 Deutsch, C., Gruber, N., Key, R. M., and Sarmiento, J. L.: Denitrification and N_2 fixation in
14 the Pacific Ocean, *Global Biogeochemical Cycles*, 15, 483-506, 2001.

15 Deutsch, C., Sigman, D. M., Thunell, R. C., Meckler, A. N., and Haug, G. H.: Isotopic
16 constraints on glacial/interglacial changes in the oceanic nitrogen budget, *Global*
17 *Biogeochem. Cycles*, 18, GB4012, doi:10.1029/2003GB002189, 2004.

18 Dunne, J. P., Sarmiento, J. L., and Gnanadesikan, A.: A synthesis of global particle export
19 from the surface ocean and cycling through the ocean interior and on the seafloor, *Global*
20 *Biogeochem. Cycles*, 21, doi:10.1029/2006GB002907, 2007.

21 Duplessy, J. C., Shackleton, N. J., Fairbanks, R. G., Labeyrie, L., Oppo, D., and Kallel, N.:
22 Deepwater source variations during the last climatic cycle and their impact on the global
23 deepwater circulation, *Paleoceanography*, 3, 343-360, 1988.

24 Eakins, B. W., and Sharman, G. F.: *Hypsographic curve of Earth's surface from ETOPO1*,
25 NOAA National Geophysical Data Center, Boulder, CO, 2012.

26 Eugster, O., Gruber, N., Deutsch, C., Jaccard, S. L., and Payne, M. R.: The dynamics of the
27 marine nitrogen cycle across the last deglaciation, *Paleoceanography*, 28, 116-129,
28 10.1002/palo.20020, 2013.

- 1 Frank, M., Schwarz, B., Baumann, S., Kubik, P. W., Suter, M., and Mangini, A.: A 200 kyr
2 record of cosmogenic radionuclide production rate and geomagnetic field intensity from ^{10}Be
3 in globally stacked deep-sea sediments, *Earth and Planetary Science Letters*, 149, 121-129,
4 1997.
- 5 Franke, J., Paul, A., and Schulz, M.: Modeling variations of marine reservoir ages during the
6 last 45 000 years, *Climate of the Past*, 4, 125-136, 2008.
- 7 Froelich, P. N., Bender, M. L., Luedtke, N. A., Heath, G. R., and DeVries, T.: The marine
8 phosphorus cycle, *American Journal of Science*, 282, 474-511, 1982.
- 9 Ganopolski, A., Rahmstorf, S., Petoukhov, V., and Claussen, M.: Simulation of modern and
10 glacial climates with a coupled global model of intermediate complexity, *Nature*, 391, 351-
11 356, 1998.
- 12 Ganopolski, A., Calov, R., and Claussen, M.: Simulation of the last glacial cycle with a
13 coupled climate ice-sheet model of intermediate complexity, *Clim. Past*, 6, 229–244, 2010.
- 14 Ganopolski, A., and Calov, R.: The role of orbital forcing, carbon dioxide and regolith in 100
15 kyr glacial cycles, *Clim. Past*, 7, 1415-1425, 2011.
- 16 García, H. E., and Gordon, L. I.: Oxygen solubility in seawater: Better fitting equations,
17 *Limnol. Oceanogr.*, 37, 1307-1312, 1992.
- 18 Gebhardt, H., Sarnthein, M., Grootes, P. M., Kiefer, T., Kuehn, H., Schmieder, F., and Röhl,
19 U.: Paleonutrient and productivity records from the subarctic North Pacific for Pleistocene
20 glacial terminations I to V, *Paleoceanography*, 23, doi:10.1029/2007PA001513, 2008.
- 21 Gehlen, M., Bopp, L., Emprin, N., Aumont, O., Heinze, C., and Ragueneau, O.: Reconciling
22 surface ocean productivity, export fluxes and sediment composition in a global
23 biogeochemical ocean model, *Biogeosciences*, 3, 521-537, 2006.
- 24 Gnanadesekian, A., and Hallberg, R.: Physical oceanography, thermal structure and general
25 circulation, in: *Encyclopedia of Physical Science and Technology*, edited by: Meyers, R. A.,
26 Academic Press, San Diego, 189-210, 2002.

- 1 Hartnett, H. E., Keil, R. G., Hedges, J. I., and Devol, A. H.: Influence of oxygen exposure
2 time on organic carbon preservation in continental margin sediments, *Nature*, 391, 572-574,
3 1998.
- 4 Hay, W. W., and Southam, J. R.: Modulation of marine sedimentation by the continental
5 shelves, in: *The Fate of Fossil Fuel CO₂ in the Oceans*, edited by: Andersen, N. R., and
6 Malahoff, A., Plenum Press, New York, 569-604, 1977.
- 7 Hay, W. W.: Pleistocene-Holocene Fluxes Are Not the Earth's Norm, in: *Material Fluxes on*
8 *the Surface of the Earth*, edited by: Hay, W. W., and Usselman, T., *Studies in Geophysics*,
9 National Academy Press, Washington, 15-27, 1994.
- 10 Hedges, J. I., and Keil, R. G.: Sedimentary organic matter preservation: an assessment and
11 speculative synthesis, *Marine Chemistry*, 49, 81-115, 1995.
- 12 Heinze, C., Maier-Reimer, E., Winguth, A. M. E., and Archer, D.: A global oceanic sediment
13 model for long-term climate studies, *Global Biogeochemical Cycles*, 13, 221-250, 1999.
- 14 Honjo, S., Manganini, S. J., Krishfield, R. A., and Francois, R.: Particulate organic carbon
15 fluxes to the ocean interior and factors controlling the biological pump: A synthesis of global
16 sediment trap programs since 1983, *Progress In Oceanography*, 76, 217-285, doi: DOI:
17 10.1016/j.pocean.2007.11.003, 2008.
- 18 Huybers, P., and Langmuir, C.: Feedback between deglaciation, volcanism, and atmospheric
19 CO₂, *Earth and Planetary Science Letters*, 286, 479-491, 2009.
- 20 Imbrie, J., and Imbrie, J. Z.: Modeling the climatic response to orbital variations, *Science*,
21 207, 943-953, 1980.
- 22 Imbrie, J., Berger, A., E.A., B., Clemens, S. C., Duffy, A., Howard, W. R., Kukja, G.,
23 Kutzbach, J., Martinson, D. G., McIntyre, A., Mix, A. C., Molino, B., Morley, J. J., Peterson,
24 L. C., Pjsias, N. G., Prell, W. L., Raymo, M. E., Shackleton, N. J., and Toggweiler, J. R.: On
25 the structure and origin of major glaciation cycles. 2. The 100,000-year cycle,
26 *Paleoceanography*, 8, 699-735, 1993.
- 27 Ingall, E. D., and Jahnke, R. A.: Evidence for enhanced phosphorus regeneration from marine
28 sediments overlain by oxygen depleted waters, *Geochimica et Cosmochimica Acta*, 58, 2571-
29 2575, 1994.

- 1 Jaccard, S. L., and Galbraith, E. D.: Large climate-driven changes of oceanic oxygen
2 concentrations during the last deglaciation, *Nature Geoscience*, 5, 151-156, 2012.
- 3 Jahnke, R. A.: The global ocean flux of particulate organic carbon: Areal distribution and
4 magnitude, *Global Biogeochemical Cycles*, 10, 71-88, 1996.
- 5 Key, R. M., Kozyr, A., Sabine, C. L., Lee, K., Wanninkhof, R., Bullister, J. L., Feely, R. A.,
6 Millero, F. J., Mordy, C., and Peng, T.-H.: A global ocean carbon climatology: Results from
7 Global Data Analysis Project (GLODAP), *Global Biogeochem. Cycles*, 18, GB4031,
8 doi:10.1029/2004GB002247, 2004.
- 9 Kleypas, J. A.: Modeled estimates of global reef habitat and carbonate production since the
10 last glacial maximum, *Paleoceanogr.*, 12, 533-545, 1997.
- 11 Köhler, P., and Fischer, H.: Simulating changes in the terrestrial biosphere during the last
12 glacial/interglacial transition, *Global and Planetary Change*, 43, 33-55, 2004.
- 13 Köhler, P., Fischer, H., Munhoven, G., and Zeebe, R. E.: Quantitative interpretation of
14 atmospheric carbon records over the last glacial termination, *Global Biogeochemical Cycles*, 19,
15 10.1029/2004GB002345, 2005.
- 16 Köhler, P., Muscheler, R., and Schmitt, J.: A model-based interpretation of low-frequency
17 changes in the carbon cycle during the last 120,000 years and its implications for the
18 reconstruction of atmospheric $\Delta^{14}\text{C}$, *Geochemistry, Geophysics, Geosystems*, 7,
19 doi:10.1029/2008PA001703, 2006.
- 20 Körtzinger, A., Hedges, J. I., and Quay, P. D.: Redfield ratios revisited: Removing the biasing
21 effect of anthropogenic CO_2 , *Limnology and Oceanography*, 46, 964-970, 2001.
- 22 Krom, M. D., and Berner, R. A.: The diagenesis of phosphorus in a nearshore marine
23 sediment, *Geochimica et Cosmochimica Acta*, 45, 207-216, 1981.
- 24 Laj, C., Kissel, C., Mazaud, A., Michel, E., Muscheler, R., and Beer, J.: Geomagnetic field
25 intensity, North Atlantic Deep Water circulation and atmospheric D^{14}C during the last 50 kyr,
26 *Earth and Planetary Science Letters*, 200, 177-190, 2002.
- 27 Lambeck, K., Rouby, H., Purcell, A., Sun, Y., and Sambridge, M.: Sea level and global ice
28 volumes from the Last Glacial Maximum to the Holocene, *PNAS*, 111, 15296–15303, 2014.

1 Lambert, F., Tagliabue, A., Shaffer, G., Lamy, F., Winckler, G., Farias, L., Gallardo, L., and
2 De Pol-Holz, R.: Dust fluxes and iron fertilization in Holocene and Last Glacial Maximum
3 climates, *Geophysical Research Letters*, 42, 6014-6023, 10.1002/2015gl064250, 2015.

4 Lomnitz, U., Sommer, S., Dale, A. W., Löscher, C. R., ke, A. N., K. Wallmann, and Hensen,
5 C.: Benthic phosphorus cycling in the Peruvian oxygen minimum zone, *Biogeosciences*
6 *Discuss.*, 12, 16755–16801, doi:10.5194/bgd-12-16755-2015, 2015.

7 Madec, G., Delecluse, P., Imbard, M., and Levy, C.: OPA8.1 Ocean general circulation model
8 reference manual, Notes du pôle de modél. 11, Inst. Pierre-Simon Laplace, Paris, 91, 1998.

9 Marcott, S. A., Bauska, T. K., Buizert, C., Steig, E. J., Rosen, J. L., Cuffey, K. M., Fudge, T.
10 J., Severinghaus, J. P., Ahn, J., Kalk, M. L., McConnell, J. R., Sowers, T., Taylor, K. C.,
11 White, J. W. C., and Brook, E. J.: Centennial-scale changes in the global carbon cycle during
12 the last deglaciation, *Nature*, 514, 616-619, 2014.

13 Marinov, I., Gnanadesikan, A., Toggweiler, J. R., and Sarmiento, J. L.: The Southern Ocean
14 biogeochemical divide, *Nature*, 441, 964-967, 2006.

15 Martin, J. H.: Glacial-interglacial CO₂ change: The iron hypothesis, *Paleoceanography*, 5, 1-
16 13, 1990.

17 Martinez-Garcia, A., Sigman, D. M., Ren, H., Anderson, R. F., Straub, M., Hodell, D. A.,
18 Jaccard, S. L., Eglinton, T. I., and Haug, G. H.: Iron fertilization of the Subantarctic ocean
19 during the last ice age, *Science*, 343, 1347-1350, 10.1126/science.1246848, 2014.

20 Martinez-Garcia, A., Sigman, D. M., Ren, H., Anderson, R. F., Straub, M., Hodell, D. A.,
21 Jaccard, S. L., L.Eglinton, T., and Haug, G. H.: Iron fertilization of the Subantarctic Ocean
22 during the last ice age, *Science*, 343, 1347-1350, 2014.

23 Mayer, L. M., Schick, L. L., Hardy, K. R., Wagal, R., and McCarthy, J.: Organic matter in
24 small mesopores in sediments and soils, *Geochimica et Cosmochimica Acta*, 68, 3863-3872,
25 2004.

26 McManus, J. F., Francois, R., Gherardi, J.-M., Keigwin, L. D., and Brown-Leger, S.: Collapse
27 and rapid resumption of Atlantic meridional circulation linked to deglacial climate changes,
28 *Nature*, 428, 834-837, 2004.

- 1 Menviel, L., Joos, F., and Ritz, S. P.: Simulating atmospheric CO₂, C-13 and the marine
2 carbon cycle during the Last Glacial-Interglacial cycle: possible role for a deepening of the
3 mean remineralization depth and an increase in the oceanic nutrient inventory, *Quaternary
4 Science Reviews*, 56, 46-68, 10.1016/j.quascirev.2012.09.012, 2012.
- 5 Middelburg, J. J., Soetaert, K., Herman, P. M. J., and Heip, C. H. R.: Denitrification in marine
6 sediments: A model study, *Global Biogeochemical Cycles*, 10, 661-673, 1996.
- 7 Milankovitch, M.: *Kanon der Erdbestrahlung und Seine Anwendung auf das
8 Eiszeitenproblem*, Royal Serbian Academy Special Publication, Royal Serbian Academy,
9 Belgrade, Serbia, 1941.
- 10 Milliman, J. D., and Droxler, A. W.: Neritic and pelagic carbonate sedimentation in the
11 marine environment: ignorance is not a bliss, *Geol. Rundsch.*, 85, 496-504, 1996.
- 12 Milne, G. A., and Mitrovica, J. X.: Searching for eustasy in deglacial sea-level histories,
13 *Quaternary Science Reviews*, 27, 2292-2302, 2008.
- 14 Monnin, E., Indermühle, A., Dallenbach, A., Flückiger, J., Stauffer, B., Stocker, T. F.,
15 Raynaud, D., and Barnola, J.-M.: Atmospheric CO₂ concentrations over the Last Glacial
16 Termination *Science*, 291, 112-114, 2001.
- 17 Monnin, E., Steig, E. J., Siegenthaler, U., Kawamura, K., Schwander, J., Stauffer, B., Stocker,
18 T. F., Morse, D. L., Barnola, J.-M., Bellier, B., Raynaud, D., and Fischer, H.: Evidence for
19 substantial accumulation rate variability in Antarctica during the Holocene, through
20 synchronization of CO₂ in the Taylor Dome, Dome C and DML ice cores, *Earth and Planetary
21 Science Letters*, 224, 45-54, 2004.
- 22 Mook, W. G., and Plicht, J. v. d.: Reporting C-14 activities and concentrations, *Radiocarbon*,
23 41, 227-239, 1999.
- 24 Munhoven, G.: Glacial-interglacial changes of continental weathering: estimates of the related
25 CO₂ and HCO₃⁻ flux variations and their uncertainties, *Global and Planetary Change*, 33, 155-
26 176, 2002.
- 27 Muscheler, R., Beer, J., Kubik, P. W., and Synal, H.-A.: Geomagnetic field intensity during
28 the last 60,000 years based on ¹⁰Be and ³⁶Cl from the Summit ice cores and ¹⁴C., *Quaternary
29 Science Reviews*, 24, 1849-1860, 2005.

- 1 Noffke, A., Hensen, C., Sommer, S., Scholz, F., Bohlen, L., Mosch, T., Graco, M., and
2 Wallmann, K.: Benthic iron and phosphorus fluxes across the Peruvian oxygen minimum
3 zone, *Limnology and Oceanography*, 57, 851-867, 2012.
- 4 Oliver, K. I. C., Hoogakker, B. A. A., Crowhurst, S., Henderson, G. M., Rickaby, R. E. M.,
5 Edwards, N. R., and Elderfield, H.: A synthesis of marine sediment core $\delta^{13}\text{C}$ data over the
6 last 150 000 years, *Clim. Past*, 6, 645-673, 2010.
- 7 Opdyke, B. N., and Walker, J. C. G.: Return of the coral reef hypothesis: Basin to shelf
8 partitioning of CaCO_3 and its effect on atmospheric CO_2 , *Geology*, 20, 733-736, 1992.
- 9 Peterson, C. D., Lisiecki, L. E., and Stern, J. V.: Deglacial whole-ocean $\delta^{13}\text{C}$ change
10 estimated from 480 benthic foraminiferal records, *Paleoceanography*, 29, 549-563,
11 doi:10.1002/2013PA002552., 2014.
- 12 Petit, L. R., Jouzel, J., Raynaud, D., Barkov, N. I., Barnola, J.-M., Basile, I., Bender, M.,
13 Chappelaz, J., Davis, M., Delaygue, G., Delmotte, M., Kotlyakov, V. M., Legrand, M.,
14 Lipenkov, V. Y., Lorius, C., Pépin, L., Ritz, C., Saltzman, E., and Stievenard, M.: Climate
15 and atmospheric history of the past 420,000 years from the Vostok ice core, Antarctica,
16 *Nature*, 399, 429-436, 1999.
- 17 Piotrowski, A. M., Goldstein, S. L., Hemming, S. R., and Fairbanks, R. G.: Temporal
18 relationships of carbon cycling and ocean circulation at glacial boundaries, *Science*, 307,
19 1933-1937, 2005.
- 20 Pollard, D.: Ice-age simulations with a calving ice-sheet model, *Quaternary Research*, 20, 30-
21 48, 1983.
- 22 Rae, J. W. B., Sarnthein, M., Foster, G. L., Ridgwell, A., Grootes, P. M., and Elliott, T.:
23 Deep water formation in the North Pacific and deglacial CO_2 rise, *Paleoceanography*, 29, 645-
24 667, 10.1002/2013PA002570, 2014.
- 25 Raitzsch, M., Hathorne, E. C., Kuhnert, H., Groeneveld, J., and Bickert, T.: Modern and late
26 Pleistocene B/Ca ratios of the benthic foraminifer *Planulina wuellerstorfi* determined with
27 laser ablation ICP-MS, *Geology*, 39, 1039-1042, 2011.
- 28 Raymo, M. E., Oppo, D. W., and Curry, W.: The mid-Pleistocene climate transition: A deep
29 sea carbon isotope perspective, *Paleoceanogr.*, 12, 546-559, 1997.

- 1 Redfield, A. C.: The biological control of chemical factors in the environment, *American*
2 *Scientist*, 46, 205-221, 1958.
- 3 Reimer, P. J., Bard, E., Bayliss, A., Beck, J. W., Blackwell, P. G., Ramsey, C. B., Buck, C. E.,
4 Cheng, H., Edwards, R. L., Friedrich, M., Grootes, P. M., Guilderson, T. P., Haflidason, H.,
5 Hajdas, I., Hatté, C., Heaton, T. J., Hoffmann, D. L., Hogg, A. G., Hughen, K. A., Kaiser, K.
6 F., Kromer, B., Manning, S. W., Niu, M., Reimer, R. W., Richards, D. A., Scott, E. M.,
7 Southon, J. R., Staff, R. A., Turney, C. S. M., and Plicht, J. v. d.: IntCal13 and marine13
8 radiocarbon age calibration curves 0 - 50,000 years Cal BP, *Radiocarbon*, 55, 1869-1887,
9 2013.
- 10 Ridgwell, A.: Glacial-interglacial perturbations in the global carbon cycle, PhD, University
11 of East Anglia, Norwich, UK, 2001.
- 12 Roberts, N. L., Piotrowski, A. M., McManus, J. F., and Keigwin, L. D.: Synchronous
13 deglacial overturning and water mass source changes, *Science*, 327, 75-78, 2010.
- 14 Robinson, L. F., Adkins, J. F., Keigwin, L. D., Southon, J., Fernandez, D. P., Wang, S.-L.,
15 and Scheirer, D. S.: Radiocarbon Variability in the Western North Atlantic During the Last
16 Deglaciation, *Science*, 310, 1469-1473, 2005.
- 17 Romanek, C. S., Grossman, E. L., and Morse, J. W.: Carbon isotope fractionation in synthetic
18 aragonite and calcite: Effects of temperature and precipitation rate, *Geochimica et*
19 *Cosmochimica Acta*, 56, 419-430, 1992.
- 20 Roth, R., Ritz, S. P., and Joos, F.: Burial-nutrient feedbacks amplify the sensitivity of
21 atmospheric carbon dioxide to changes in organic matter remineralisation, *Earth Syst.*
22 *Dynam.*, 5, 321-343, 2014.
- 23 Ruttenberg, K. C.: Development of a sequential extraction method for different forms of
24 phosphorus in marine sediments, *Limnol. Oceanogr.*, 37, 1460-1482, 1992.
- 25 Ruttenberg, K. C., and Berner, R. A.: Authigenic apatite formation and burial in sediments
26 from non-upwelling, continental margin environments, *Geochimica et Cosmochimica Acta*,
27 57, 991-1007, 1993.
- 28 Sarmiento, J. L., and Gruber, N.: *Ocean Biogeochemical Cycles*, Princeton University Press,
29 Princeton, 503 pp., 2006.

- 1 Sarnthein, M., Winn, K., Jung, S. J. A., Duplessy, J.-C., Labeyrie, L., Erlenkeuser, H., and
2 Ganssen, G.: Changes in east Atlantic deepwater circulation over the last 30,000 years: Eight
3 time slice reconstructions, *Paleoceanography*, 9, 209-267, 1994.
- 4 Sarnthein, M., Schneider, B., and Grootes, P. M.: Peak glacial ^{14}C ventilation ages suggest
5 major draw-down of carbon into the abyssal ocean, *Clim. Past*, 9, 2595-2614, 2013.
- 6 Sarnthein, M., Balmer, S., Grootes, P. M., and Mudelsee, M.: Planktic and benthic ^{14}C
7 reservoir ages for three ocean basins, calibrated by a suite of ^{14}C plateaus in the glacial-to-
8 deglacial Suigetsu atmospheric ^{14}C record, *Radiocarbon*, in press, 2014.
- 9 Sarnthein, M., Balmer, S., Grootes, P. M., and Mudelsee, M.: Planktic and benthic ^{14}C
10 reservoir ages for three ocean basins, calibrated by a suite of ^{14}C plateaus in the glacial-to-
11 deglacial Suigetsu atmospheric ^{14}C record, *Radiocarbon*, 57, 129-151, 2015.
- 12 Schenau, S. J., and De Lange, G. J.: Phosphorus regeneration vs. burial in sediments of the
13 Arabian Sea, *Marine Chemistry*, 75, 201-217, 2001.
- 14 Schlünz, B., Schneider, R. R., Müller, P. J., Swowers, W. J., and Wefer, G.: Terrestrial
15 organic carbon accumulation on the Amazon deep sea fan during the last glacial sea level
16 stand, *Chemical Geology*, 159, 263-281, 1999.
- 17 Schmitt, J., Schneider, R., Elsig, J., Leuenberger, D., Laurantou, A., Chappellaz, J., Köhler,
18 P., Joos, F., Stocker, T. F., Leuenberger, M., and Fischer, H.: Carbon isotope constraints on
19 the deglacial CO_2 rise from ice cores, *Science*, 336, 711-714, 2012.
- 20 Schmittner, A., Urban, N. M., Shakun, J. D., Mahowald, N. M., Clark, P. U., Bartlein, P. J.,
21 Mix, A. C., and Rosell-Melé, A.: Climate sensitivity estimated from temperature
22 reconstructions of the Last Glacial Maximum, *Science*, 334, 1385-1388, 2011.
- 23 Schmittner, A., Gruber, N., Mix, A. C., Key, R. M., Tagliabue, A., and Westberry, T. K.:
24 Biology and air–sea gas exchange controls on the distribution of carbon isotope ratios ($\delta^{13}\text{C}$)
25 in the ocean, *Biogeosciences*, 10, 5793-5816, 2013.
- 26 Seiter, K., Hensen, C., and Zabel, M.: Benthic carbon mineralization on a global scale, *Global*
27 *Biogeochemical Cycles*, 19, doi:10.1029/2004GB002225, 2005.

- 1 Shackleton, N. J.: Carbon-13 in *Uvigerina*: Tropical rainforest history in the equatorial Pacific
2 carbonate dissolution cycles, in: *The Fate of Fossil Fuel in the Oceans*, edited by: Andersen,
3 N. R., and Malahoff, A., Plenum, New York, 401-427, 1977.
- 4 Skinner, L. C.: Glacial-interglacial atmospheric CO₂ change: a possible “standing volume”
5 effect on deep-ocean carbon sequestration, *Climate of the Past*, 5, 537–550, 2009.
- 6 Skinner, L. C., Fallon, S., Waelbroeck, C., Michel, E., and Barker, S.: Ventilation of the deep
7 Southern Ocean and deglacial CO₂ rise, *Science*, 328, 1147-1151, 2010.
- 8 Skinner, L. C., Waelbroeck, C., Scrivner, A. E., and Fallon, S. J.: Radiocarbon evidence for
9 alternating northern and southern sources of ventilation of the deep Atlantic carbon pool
10 during the last deglaciation, *PNAS*, 111, 5480-5484, 2014.
- 11 Stanford, J. D., Hemingway, R., Rohling, E. J., Challenor, P. G., Medina-Elizalde, M., and
12 Lester, A. J.: Sea-level probability for the last deglaciation: A statistical analysis of far-field
13 records, *Global and Planetary Change*, 79, 193-203, 2011.
- 14 Stolpovsky, K., Dale, A. W., and Wallmann, K.: Toward a parameterization of global-scale
15 organic carbon mineralization kinetics in surface marine sediments, *Global Biogeochemical*
16 *Cycles*, 29, 812-829, 10.1002/2015gb005087, 2015.
- 17 Stuiver, M., and Polach, H. A.: Discussion: Reporting of ¹⁴C data, *Radiocarbon*, 19, 355-363,
18 1977.
- 19 Suess, E.: Particulate organic carbon flux in the oceans - Surface productivity and oxygen
20 utilization, *Nature*, 288, 260-263, 1980.
- 21 Tamburini, F., and Föllmi, K. B.: Phosphorus burial in the ocean over glacial-interglacial time
22 scales, *Biogeosciences*, 6, 501-513, 2009.
- 23 Thornalley, D. J. R., Barker, S., Broecker, W. S., Elderfield, H., and McCave, N.: The
24 Deglacial Evolution of North Atlantic Deep Convection, *Science*, 331, 202-205, 2011.
- 25 Toggweiler, J. R.: Variation of atmospheric CO₂ by ventilation of the ocean's deepest water,
26 *Paleoceanography*, 14, 571-588, 1999.

- 1 Tschumi, T., Joos, F., Gehlen, M., and Heinze, C.: Deep ocean ventilation, carbon isotopes,
2 marine sedimentation and the deglacial CO₂ rise, *Climate of the Past*, 7, 771-
3 800, 10.5194/cp-7-771-2011, 2011a.
- 4 Tschumi, T., Joos, F., Gehlen, M., and Heinze, C.: Deep ocean ventilation, carbon isotopes,
5 marine sedimentation and the deglacial CO₂ rise, *Clim. Past*, 7, 771–800, 2011b.
- 6 Tyrrell, T.: The relative influences of nitrogen and phosphorus on oceanic primary
7 production, *Nature*, 400, 525-531, 1999.
- 8 Ushie, H., and Matsumoto, K.: The role of shelf nutrients on glacial-interglacial CO₂: A
9 negative feedback, *Global Biogeochemical Cycles*, 26, doi:10.1029/2011GB004147, 2012.
- 10 Van Cappellen, P., and Ingall, E. D.: Benthic phosphorus regeneration, net primary
11 production, and ocean anoxia: A model of the coupled marine biogeochemical cycles of
12 carbon and phosphorus, *Paleoceanography*, 9, 677-692, 1994.
- 13 Waelbroeck, C., Labeyrie, L., Michel, E., Duplessy, J.-C., McManus, J. F., Lambeck, K.,
14 Balbon, E., and Labracherie, M.: Sea-level and deep water temperature changes derived from
15 benthic foraminifera isotopic records, *Quaternary Science Reviews*, 21, 295-305, 2002.
- 16 Wallmann, K.: Feedbacks between oceanic redox states and marine productivity: A model
17 perspective focused on benthic phosphorus cycling, *Global Biogeochemical Cycles*, 17, 1084,
18 doi: 1010.1029GB001968, 2003.
- 19 Wallmann, K.: Phosphorus imbalance in the global ocean?, *Global Biogeochemical Cycles*,
20 24, doi:10.1029/2009GB003643, 2010.
- 21 Wallmann, K., Burwicz, E., Ruepke, L., Marquardt, M., Pinero, E., Haeckel, M., and Hensen,
22 C.: Constraining the global inventory of methane hydrate in marine sediments, *Proceedings of*
23 *the 7th International Conference on Gas Hydrates*, Edinburgh, Edinburgh, Scotland, United
24 Kingdom, 2011,
- 25 Wallmann, K., Pinero, E., Burwicz, E., Haeckel, M., Hensen, C., Dale, A., and Ruepke, L.:
26 The global inventory of methane hydrate in marine sediments: A theoretical approach,
27 *Energies*, 5, 2449-2498, 2012.

- 1 Wallmann, K.: Is late Quaternary climate change governed by self-sustained oscillations in
2 atmospheric CO₂?, *Geochimica et Cosmochimica Acta*, 132, 413-439, 2014.
- 3 Walsh, J. J., Rowe, G. T., Iverson, R. L., and McRoy, C. P.: Biological export of shelf carbon
4 is a sink of the global CO₂ cycle, *Nature*, 291, 196-201, 1981.
- 5 Watson, A. J., Vallis, G. K., and Nikurashin, M.: Southern Ocean buoyancy forcing of ocean
6 ventilation and glacial atmospheric CO₂, *Nature Geoscience*, 10.1038/NGEO2538, 2015.
- 7 Yu, J., Elderfield, H., and Piotrowski, A. M.: Seawater carbonate ion- $\delta^{13}\text{C}$ systematics and
8 application to glacial-interglacial North Atlantic ocean circulation, *Earth and Planetary
9 Science Letters*, 271, 209 - 220, 2008.
- 10 Yu, J., Broecker, W. S., Elderfield, H., Jin, Z., McManus, J., and Zhang, F.: Loss of carbon
11 from the deep sea since the Last Glacial Maximum, *Science*, 330, 1084-1087, 2010.
- 12 Yu, J., Anderson, R. F., Jin, Z., Rae, J. W. B., Opdyke, B. N., and Eggins, S. M.: Responses
13 of the deep ocean carbonate system to carbon reorganization during the Last Glacial-
14 interglacial cycle, *Quaternary Science Reviews*, 76, 39 - 52, 2013.
- 15 Yu, J., Anderson, R. F., Jin, Z., Menviel, L., Zhang, F., Ryerson, F. J., and Rohling, E. J.:
16 Deep South Atlantic carbonate chemistry and increased interocean deep water exchange
17 during last deglaciation, *Quaternary Science Reviews*, 90, 80-89, 2014.
- 18 Zeebe, R., and Wolf-Gladrow, D.: CO₂ in Seawater: Equilibrium, Kinetics and Isotopes,
19 Elsevier Oceanography Series, Elsevier, Amsterdam, 346 pp., 2001.
- 20 Zhang, J., Quay, P. D., and Wilbur, D. O.: Carbon-isotope fractionation during gas-water
21 exchange and dissolution of CO₂, *Geochimica et Cosmochimica Acta*, 59, 107-114, 1995.
- 22 Zimov, S. A., Schuur, E. A. G., and Chapin III, F. S.: Permafrost and the global carbon
23 budget, *Science*, 312, 1612-1613, 2006.

24
25
26

1 Table 1 Controls on atmospheric pCO₂ and mean dissolved carbon and phosphorus
 2 concentrations in the global ocean

Simulation	pCO ₂ at 21 ka in ppmv	pCO ₂ at 0 ka in ppmv	DIC at 21 ka in μM	DIC at 0 ka in μM	DP at 21 ka in μM	DP at 0 ka in μM
STD (standard simulation)	190	279	2465	2300	2.44	2.14
STD with constant SST	206	275	2453	2289	2.48	2.15
STD with constant salinity	185	291	2466	2301	2.44	2.14
STD with constant salinity and constant ocean volume	177	281	2409	2310	2.41	2.16
STD with constant riverine DP flux	240	345	2564	2430	2.16	1.98
STD with constant rates of chemical weathering	193	268	2355	2202	2.15	1.98
STD with constant depositional area for P burial	263	367	2599	2478	2.03	1.95
STD with constant depositional area for POC burial	129	180	2132	1925	2.42	2.07
STD with constant burial rate of neritic carbonates	200	277	2437	2291	2.46	2.15
STD-CC-CN	234	255	2400	2273	2.68	2.30
STD with constant AMOC	200	262	2381	2233	2.49	2.12
STD-CC	203	263	2364	2240	2.31	2.14

3

4

- 1 Table A1. Salinity (Sal in PSU), dissolved phosphate, nitrate, and oxygen in model boxes (in
- 2 μM): Model versus data. Subscripts: S: surface water (0 – 100m), I: intermediate water (100 –
- 3 2000m), D: deep water (2000 – 4000m), B: bottom water (>4000m)

Box	Sal Data	Sal Model	PO ₄ Data	PO ₄ Model	NO ₃ Data	NO ₃ Model	O ₂ Data	O ₂ Model
AR _S	32.96	33.01	0.84	0.825	6.58	11.1	340.7	349
NA _S	35.55	35.24	0.29	0.325	4.	4.67	257.2	248
TA _S	36.22	36.1	0.31	0.335	3.09	4.19	201.6	212
SO _S	34.5	34.3	1.05	1.08	13.01	14.2	290.3	284
TIP _S	35.03	34.95	0.4	0.447	3.03	4.34	198.9	208
NP _S	33.6	33.59	0.84	0.781	8.15	9.88	276.	263
AR _I	34.83	34.82	0.99	0.961	13.22	13.4	296.7	313
NA _I	35.28	35.05	0.87	1.12	16.29	16.8	238.6	234
TA _I	34.99	34.93	1.63	1.72	25.1	25.5	181.5	169
SO _I	34.58	34.54	1.98	2.05	28.43	29.1	209.7	212
TIP _I	34.68	34.64	2.37	2.43	32.16	34.1	107.1	93.4
NP _I	34.32	34.52	2.75	2.67	38.17	35.7	73.65	90.7
AR _D	34.94	34.87	1.04	1.07	14.69	15	287.	287
NA _D	34.95	34.92	1.18	1.19	18.71	16.9	265.1	257
TA _D	34.92	34.9	1.43	1.54	21.67	21.8	245.5	220
SO _D	34.72	34.76	2.2	2.14	31.32	29.2	203.7	211
TIP _D	34.69	34.75	2.49	2.53	35.5	33.9	145.5	149
NP _D	34.65	34.69	2.73	2.57	38.63	34.1	116.	134
AR _B	34.94	34.87	1.05	1.08	14.6	15.2	276.5	285
NA _B	34.9	34.91	1.33	1.42	20.18	19.3	260.5	237
TA _B	34.86	34.87	1.56	1.64	23.81	23	242.4	217
SO _B	34.7	34.76	2.22	2.16	32.07	29.4	220.2	206
TIP _B	34.7	34.75	2.34	2.39	33.65	31.8	176.4	173
NP _B	34.69	34.71	2.51	2.52	36.02	33.4	155.9	144

4

- 1 Table A2. Dissolved inorganic carbon (DIC), total alkalinity (TA), $\delta^{13}\text{C}$ -DIC, and $\Delta^{14}\text{C}$ -DIC
 2 in model boxes (concentrations in μM , isotope data in ‰): Model versus data.

Box	DIC Data*	DIC Model	TA Data	TA Model	$\delta^{13}\text{C}$ Data ⁺	$\delta^{13}\text{C}$ Model	$\Delta^{14}\text{C}$ Data*	$\Delta^{14}\text{C}$ Model
AR _S	2101	2166	2372.	2357	n. d.	2.11	n. d.	-68.26
NA _S	2074	2056	2410.	2410	1.47	2.77	-75.6	-69.02
TA _S	2061	2032	2444.	2453	1.64	2.77	-67.3	-65.35
SO _S	2104	2083	2365.	2340	1.41	1.8	-85.1	-78.38
TIP _S	2006	1944	2359.	2347	1.28	2.24	-60.1	-64.04
NP _S	2037	2022	2300.	2306	1.3	2.27	-75.7	-72.01
AR _I	2169	2176	2373.	2375	n. d.	1.79	n. d.	-78.03
NA _I	2179	2180	2391.	2392	0.9	1.45	-75.	-90.32
TA _I	2225	2259	2386.	2400	0.84	0.625	-101.8	-114
SO _I	2254	2257	2392.	2380	0.72	-0.053	-130.4	-126.5
TIP _I	2317	2311	2418.	2391	0.32	-0.653	-148.3	-134.7
NP _I	2370	2373	2421.	2436	-0.23	-0.875	-179.7	-183.3
AR _D	2188	2185	2371.	2379	n. d.	1.62	n. d.	-85.97
NA _D	2216	2195	2388.	2384	0.97	1.44	-87.9	-93.75
TA _D	2242	2239	2402.	2401	0.96	0.933	-116.6	-122.3
SO _D	2315	2314	2431.	2441	0.1	0.119	-166.	-167.1
TIP _D	2382	2382	2481.	2493	-0.06	-0.272	-199.6	-192.5
NP _D	2416	2388	2491.	2492	-1.09	-0.432	-217.8	-214.2
AR _B	2188	2186	2371.	2379	n. d.	1.6	n. d.	-86.2
NA _B	2241	2221	2403.	2395	0.92	1.17	-118.4	-110.7
TA _B	2268	2253	2418.	2411	0.77	0.792	-132.1	-132.9
SO _B	2318	2319	2434.	2446	0.1	0.102	-162.7	-169.2
TIP _B	2360	2363	2472.	2488	0.14	-0.111	-184.4	-184.7
NP _B	2388	2384	2491.	2495	-0.58	-0.352	-206.8	-212.7

- 3 *: corrected for anthropogenic CO₂; †: not corrected for anthropogenic CO₂

4

1 Table A3. Water fluxes (in Sv) derived from the NEMO model run and fluxes applied in the
 2 box model to reproduce observed tracer distributions (Tabs. A1 and A2)

Fluxes NEMO	NEMO Net	NEMO Exchange	Fluxes Box model	Box model Net	Box model Exchange
NA _S → AR _S	1.1	2.64	NA _S → AR _S	3.	1.74
NA _S → NA _I	0.43	12.2	NA _S → NA _I	9.93	42.2
TA _S → NA _S	1.48	7.26	TA _S → NA _S	12.83	0.36
SO _S → TA _S	1.34	4.33	SO _S → TA _S	12.94	0.43
SO _S → SO _I	10.43	77.58	SO _S → SO _I	3.93	106.58
TIP _S → SO _S	8.16	12.42	TIP _S → SO _S	15.94	12.42
NP _S → TIP _S	0.43	10.93	NP _S → TIP _S	0.31	2.93
NP _S → AR _S	1.14	0.03	NP _S → AR _S	1.14	0.03
AR _S → AR _I	2.37	10.38	AR _S → AR _I	4.37	45.38
NA _I → AR _I	2.11	24.51	NA _I → AR _I	2.11	14.51
NA _I → NA _D	2.23	23.08	NA _I → NA _D	8.23	0.08
TA _I → TA _S	0.58	24.91	TA _I → TA _S	0.58	0.41
TA _I → NA _I	3.91	27.73	TA _I → NA _I	0.41	17.73
SO _I → TA _I	3.42	24.89	TA _I → SO _I	0.08	4.87
SO _I → TIP _I	1.29	88.37	SO _I → TIP _I	13.79	73.37
TIP _I → TIP _S	11.39	77.11	TIP _I → TIP _S	16.39	77.11
NP _I → NP _S	1.26	16.98	NP _I → NP _S	1.26	3.98
NP _I → TIP _I	2.	38.55	NP _I → TIP _I	2.	3.55
AR _I → AR _D	4.48	6.87	AR _I → AR _D	6.48	6.87
NA _D → TA _D	10.35	3.89	NA _D → TA _D	15.35	1.19
TA _D → TA _I	1.07	13.78	TA _D → TA _I	1.07	8.78
TA _D → SO _D	9.29	5.68	TA _D → SO _D	15.29	1.68
SO _I → SO _D	5.72	224.4	SO _D → SO _I	9.78	10.12
SO _D → SO _B	19.65	84.24	SO _D → SO _B	17.65	114.24
TIP _D → TIP _I	8.1	18.08	TIP _D → TIP _I	0.6	3.08
TIP _D → SO _D	4.64	12.54	TIP _D → SO _D	12.14	2.54
NP _D → TIP _D	5.71	10.96	TIP _D → NP _D	1.29	0.67
NP _D → NP _I	3.26	2.48	NP _D → NP _I	3.26	1.48
AR _D → NA _D	4.48	1.	AR _D → NA _D	6.48	11.
NA _B → NA _D	3.64	2.53	NA _B → NA _D	0.64	2.53
TA _B → TA _D	0.01	20.75	TA _B → TA _D	1.01	20.75
TA _B → NA _B	3.64	2.93	TA _B → NA _B	0.64	0.43
SO _B → TA _B	3.65	2.53	SO _B → TA _B	1.65	2.53
SO _B → TIP _B	16.	0.72	SO _B → TIP _B	16.	15.72
TIP _B → TIP _D	7.03	55.76	TIP _B → TIP _D	14.03	35.76
TIP _B → NP _B	8.97	8.65	TIP _B → NP _B	1.97	0.65
NP _B → NP _D	8.97	7.32	NP _B → NP _D	1.97	7.32
AR _B → AR _D	0	0.19	AR _B → AR _D	0	1.19
FRESH → NA _S	0.05		FRESH → NA _S	0.10	
FRESH → TA _S	-0.44		FRESH → TA _S	-0.69	
FRESH → SO _S	3.61		FRESH → SO _S	0.93	
FRESH → TIP _S	-3.66		FRESH → TIP _S	-0.76	

FRESH \rightarrow NP _S	0.31		FRESH \rightarrow NP _S	0.19	
FRESH \rightarrow AR _S	0.13		FRESH \rightarrow AR _S	0.23	

1

2 Table A4. Biogeochemical parameter values determined by fitting the model to observations

Parameter	Symbol	Units	AR	NA	TA	SO	TIP	NP
Kinetic constant for export production	k _{EXP}	yr ⁻¹	0.05	1.5	0.4	0.15	1.1	0.12
Kinetic constant for nitrogen fixation	k _{NF}	yr ⁻¹	0.0	3.0	1.0	0.2	1.0	0.5
PIC/POC export ratio	Γ _{PICPOC}		0.01	0.08	0.20	0.01	0.15	0.07
Piston velocity	k _{SA}	cm yr ⁻¹	0.4	0.1	0.12	0.12	0.24	0.1

3

4 Table A5. Difference in δ¹³C-DIC between LGM (21 kyr BP) and Holocene (5 kyr BP) as
5 derived from data (Oliver et al., 2010; Sarnthein et al., 1994) and calculated in the standard
6 model run

Box	Data	Model
NA _I	+0.04 ± 0.28	+0.01
NA _D	-0.55 ± 0.16	-0.60
NA _B	-0.70 ± 0.13	-0.70
TA _I	+0.15 ± 0.20	+0.22
TA _D	-0.55 ± 0.24	-0.66
TA _B	-0.78 ± 0.21	-0.73
SO _D	-0.44 ± 0.26	-0.52
TIP _D	-0.44 ± 0.20	-0.36

7

8

1 Table B1 Parameter values applied in the simulation of margin processes

Parameter	Symbol	Value	Source
Modern seafloor area at 0 - 50 m	A_{NM}	$13.54 \times 10^6 \text{ km}^2$	(Eakins and Sharman, 2012)
Modern seafloor area at 0 - 100 m	A_{SM}	$20.34 \times 10^6 \text{ km}^2$	(Eakins and Sharman, 2012)
Modern seafloor area at 100 - 2000 m	A_{IM}	$38.29 \times 10^6 \text{ km}^2$	(Eakins and Sharman, 2012)
Modern rate of neritic carbonate burial	F_{BPICSM}	10 Tmol yr^{-1}	(Kleypas, 1997)
Modern rate of marine POC burial at 0 - 100 m	F_{BPOCSM}	5 Tmol yr^{-1}	(Wallmann et al., 2011)
Modern rate of marine POC burial at 100 - 2000 m	F_{BPOCIM}	5 Tmol yr^{-1}	(Wallmann et al., 2011)
Modern rate of marine POC burial at 2000 - 4000 m	F_{BPOCDM}	1.3 Tmol yr^{-1}	(Wallmann et al., 2011)
Modern rate of marine POC burial at >4000 m	F_{BPOCBM}	0.2 Tmol yr^{-1}	(Wallmann et al., 2011)
Modern POC export production	F_{EPOCM}	809 Tmol yr^{-1}	(Sarmiento and Gruber, 2006)
Modern rate of marine P burial at 0 - 100 m	F_{BPMSM}	$0.05 \text{ Tmol yr}^{-1}$	(Wallmann, 2010)
Modern rate of marine P burial at 100 - 2000 m	F_{BPIM}	$0.05 \text{ Tmol yr}^{-1}$	(Wallmann, 2010)
Modern rate of marine P burial at 2000 - 4000 m	F_{BPDM}	$0.06 \text{ Tmol yr}^{-1}$	(Wallmann, 2010)
Modern rate of marine P burial at >4000 m	F_{BPBM}	$0.02 \text{ Tmol yr}^{-1}$	(Wallmann, 2010)
Monod constant for P burial	k_P	$20 \mu\text{M}$	(Wallmann, 2010)
Burial efficiency of marine POC at 0 - 100 m	BE_S	0.05	This work
Burial efficiency of marine POC at 100 - 2000 m	BE_I	0.2	This work
Burial efficiency of marine POC at 2000 - 4000 m	BE_D	0.1	This work
Burial efficiency of marine POC at >4000 m	BE_B	0.02	This work
Maximum POC to P ratio in marine sediments	Γ_{CPM}	400	(Anderson et al., 2001)

2

1 Table B2 Flux parameterizations applied in the simulation of margin processes

Process	Equation*
Neritic carbonate burial	$F_{\text{BPICS}} = F_{\text{BPICSM}} \cdot \frac{A_N}{A_{\text{NM}}}$
POC burial at 0 - 100 m	$F_{\text{BPOCS}} = F_{\text{BPOCSM}} \cdot \frac{F_{\text{EPOC}}}{F_{\text{EPOCM}}} \cdot \frac{A_S}{A_{\text{SM}}}$
POC burial at 100 - 2000 m	$F_{\text{BPOCI}} = F_{\text{BPOCIM}} \cdot \frac{F_{\text{EPOC}}}{F_{\text{EPOCM}}} \cdot \frac{A_I}{A_{\text{IM}}}$
POC burial at 2000 - 4000 m	$F_{\text{BPOCD}} = F_{\text{BPOCDM}} \cdot \frac{F_{\text{EPOC}}}{F_{\text{EPOCM}}} \cdot \frac{A_{\text{SM}} + A_{\text{IM}}}{A_S + A_I}$
POC burial at > 4000 m	$F_{\text{BPOCB}} = F_{\text{BPOCBM}} \cdot \frac{F_{\text{EPOC}}}{F_{\text{EPOCM}}} \cdot \frac{A_{\text{SM}} + A_{\text{IM}}}{A_S + A_I}$
P burial at 0 - 100 m	$F_{\text{BPS}} = \text{Max} \left[F_{\text{BPSM}} \cdot \frac{F_{\text{EPOC}}}{F_{\text{EPOCM}}} \cdot \frac{A_S}{A_{\text{SM}}} \cdot \frac{\text{DO}_S}{\text{DO}_S + k_p} \cdot \frac{\text{DO}_{\text{SM}} + k_p}{\text{DO}_{\text{SM}}}, \frac{F_{\text{BPOCS}}}{r_{\text{CPM}}} \right]$
P burial at 100 - 2000 m	$F_{\text{BPI}} = \text{Max} \left[F_{\text{BPI M}} \cdot \frac{F_{\text{EPOC}}}{F_{\text{EPOCM}}} \cdot \frac{A_I}{A_{\text{IM}}} \cdot \frac{\text{DO}_I}{\text{DO}_I + k_p} \cdot \frac{\text{DO}_{\text{IM}} + k_p}{\text{DO}_{\text{IM}}}, \frac{F_{\text{BPOCI}}}{r_{\text{CPM}}} \right]$
P burial at 2000 - 4000 m	$F_{\text{BPD}} = \text{Max} \left[F_{\text{BPD M}} \cdot \frac{F_{\text{EPOC}}}{F_{\text{EPOCM}}} \cdot \frac{\text{DO}_D}{\text{DO}_D + k_p} \cdot \frac{\text{DO}_{\text{DM}} + k_p}{\text{DO}_{\text{DM}}}, \frac{F_{\text{BPOCD}}}{r_{\text{CPM}}} \right]$
P burial at > 4000 m	$F_{\text{BPB}} = \text{Max} \left[F_{\text{BPB M}} \cdot \frac{F_{\text{EPOC}}}{F_{\text{EPOCM}}} \cdot \frac{\text{DO}_B}{\text{DO}_B + k_p} \cdot \frac{\text{DO}_{\text{BM}} + k_p}{\text{DO}_{\text{BM}}}, \frac{F_{\text{BPOCB}}}{r_{\text{CPM}}} \right]$
Benthic denitrification with i = (S, I, D, B)	$F_{\text{BDENi}} = \frac{F_{\text{BPOCI}}}{\text{BE}_i} \cdot (0.06 + 0.19 \cdot 0.99^{(\text{DO}_i - \text{DN}_i)})$

2 *Subscripts indicate modern values (M) and the following environments: shelf (S, 0 – 100
3 water depth), outer shelf and slope (I, 100 – 2000 m), continental rise and deep-sea floor (D,
4 2000 – 4000 m), deep-sea floor and abyssal plain (B, >4000 m). The equations define global
5 fluxes. These were distributed among the ocean basins considered their export production and
6 the seafloor areas of individual boxes.

7

1 Table C1. Deep-sea CO₃²⁻ concentrations (in μmol/kg): Differences between 21 and 5 kyr BP
 2 (LGM - H) calculated in the standard simulation STD are compared to corresponding
 3 observational data (derived from B/Ca ratios in foraminifera, LGM - Holocene differences).

Box	Model	Data	Sites/References
AR _D	36	24 ± 10	60°N, 24°W, 2.4 km (Yu et al., 2008)
NA _D	23	18 ± 9	55°N, 20°W, 2.0 km (Yu et al., 2008)
		24 ± 10	60°N, 24°W, 2.4 km (Yu et al., 2008)
		4 ± 6	55°N, 21°W, 2.8 km (Yu et al., 2008)
		-18 ± 8	51°N, 22°W, 3.5 km (Yu et al., 2008)
		-19 ± 9	52°N, 22°W, 4.0 km (Yu et al., 2008)
NA _B	15	-19 ± 9	52°N, 22°W, 4.0 km (Yu et al., 2008)
TA _D	14	9 ± 10	4°S, 13°W, 2.9 km (Raitzsch et al., 2011)
TA _B	6	-17 ± 12	4°S, 16°W, 4.7 km (Raitzsch et al., 2011)
SO _B	1	3 ± 2	41°S, 8°E, 5.0 km (Yu et al., 2014)
TIP _D	3	2 ± 3	0°S, 158°E, 2.3 km (Yu et al., 2010)
		-6 ± 4	0°S, 161°E, 3.4 km (Yu et al., 2010)
TIP _B	2	1 ± 4	1°S, 140°W, 4.3 km (Yu et al., 2013)
		5 ± 3	10°S, 52°E, 4.1 km (Yu et al., 2010)

4

5

6 Table C2. Effect of radiocarbon production rate on atmospheric and marine ¹⁴C values under
 7 steady-state conditions. R₁₄(0) is the pre-human atmospheric production rate applied in the
 8 model calibration (1.64 atoms cm⁻² s⁻¹ = 437 mol yr⁻¹).

Rate	Δ ¹⁴ C-CO ₂ (‰)	Δ ¹⁴ C-DIC (‰)	ΔΔ ¹⁴ C-DIC (‰)
R ₁₄ (0)	+0	-148	-148
1.5 x R ₁₄ (0)	+500	+278	-222
2.0 x R ₁₄ (0)	+1000	+704	-296

9

10

- 1 Table C3. $\Delta\Delta^{14}\text{C}$ -DIC for the LGM (19 – 23 kyr BP) calculated in simulation STD and
 2 derived from radiocarbon measurements in foraminifera (atmosphere – water differences).

Box	Model	Data	Reference
AR _S	-196 to -177	EAST: -95 to -60 WEST: -210 to -240	GIK 23074 (66°66.67'N, 4°90'E, 1157 m, Norw. Current), (Sarnthein et al., 2014) PS2644 (67°52.02'N, 21°45.92'W, 777 m, East Greenland Current), (Sarnthein et al., 2013; Sarnthein et al., 2014)
AR _I	-206 to -187	-50 -220 to -270	PS2644 (67°52.02'N, 21°45.92'W, 777 m, millennial-scale oscillations?), (Sarnthein et al., 2013)
NA _S	-169 to -153	-115 to -40	MD90-917 (41°29.78'N, 17°61.3'E, 1010 m) MD99-2334K (37°48'N, 10°10'W, 3146 m) RAPID-17-5P (61°29'N, 19°32'W, 2303 m) (Thornalley et al., 2011) MD08-3180 (38°N, 31°13.45'W, 3064 m) (Sarnthein et al., 2013)
NA _D	-257 to -228	-40 to -60 -260 to -275	MD99-2334K (37°48'N, 10°10'W, 3146 m) RAPID-17-5P (61°29'N, 19°32'W, 2303 m) (Thornalley et al., 2011) MD08-3180 (38°N, 31°13.45'W, 3064 m) (Sarnthein et al., 2014)
NA _B	-285 to -253	-330	Extrapolated from Portuguese margin site MD99-2334K (37°48'N, 10°10'W, 3146 m, a site subject to enhanced Coriolis forcing) (Skinner et al., 2014) and assuming a transit time of ~800 yr from TNO57-21 (41°06'S, 7°48'E, 4981 m) (Barker et al., 2010)
TA _S	-128 to -108	-130 to -95	ODP 1002 (10°42.37'N, 65°10.18'W, 893 m) and southward extrapolated from MD08-3180 (38°N, 31°13.45'W, 3064 m) (Sarnthein et al., 2014)
TA _I	-241 to -218	-160 to -185 -85	Dredged coral transects at Gregg, Manning, and Muir Sea Mt. 33°–39°N, <2300 m, corr. according to (Robinson et al., 2005)
SO _S	-160 to -140	-270 to -190	MD07-3076 (44°09'S, 14°13'W, 3770 m) (Skinner et al., 2010)
SO _I	-228 to -201	-220 to -210	Dredged coral transect Drake Passage, <1800 m (Burke et al., 1982), + AWI unpubl. data under review
SO _D	-332 to -296	-300 to -185 -600 to -500	D07-3076 (44°09'S, 14°13'W, 3770 m) ATL. SECTOR: (Skinner et al., 2010) Sonne core transect off New Zealand PAC. SECTOR: AWI unpubl. records, under review
SO _B	-335 to -299	-230 to -130	TNO57-21 (41°06'S, 7°48'E, 4981 m) (Barker et al., 2010)
TIP _S	-139 to -120	-220 to -105	MD01-2378 (13°08.25'S, 121°78.8'E, 1783 m) (Sarnthein et al., 2014)
TIP _I	-238 to -211	-264 to -61 -205 to -190 -220 to -165	RC 27-14 (18.3°N, 57.6°E, 596 m) RC 27-23 (18.0°N, 57.6°E, 820 m) (Bryan et al., 2010) MD01-2378 (13°08.25'S, 121°78.8'E, 1783 m)

			(Sarnthein et al., 2013)
TIP _D	-363 to -324	-410 to -320	MD01-2378 (13°08.25'S, 121°78.8'E, 1783 m) GIK 17940 (20°07.0'N, 117°23.0'E, 1727 m) extrapolated to >2000 m, (Sarnthein et al., 2013)
NP _S	-156 to -137	-190 to -115	MD01-2416 (51°26.8'N, 167°72.5'E, 2317 m) MD02-2489 (54°39.07'N, 148°92.13'W, 3640 m) (Sarnthein et al., 2013; Sarnthein et al., 2014)
NP _D	-378 to -337	-470	MD01-2416 (51°26.8'N, 167°72.5'E, 2317 m) (Sarnthein et al., 2013; Sarnthein et al., 2014)
NP _B	-375 to -335	-270	MD02-2489 (54°39.07'N, 148°92.13'W, 3640 m) extrapolated to >4000 m, (Sarnthein et al., 2013; Gebhardt et al., 2008)

1

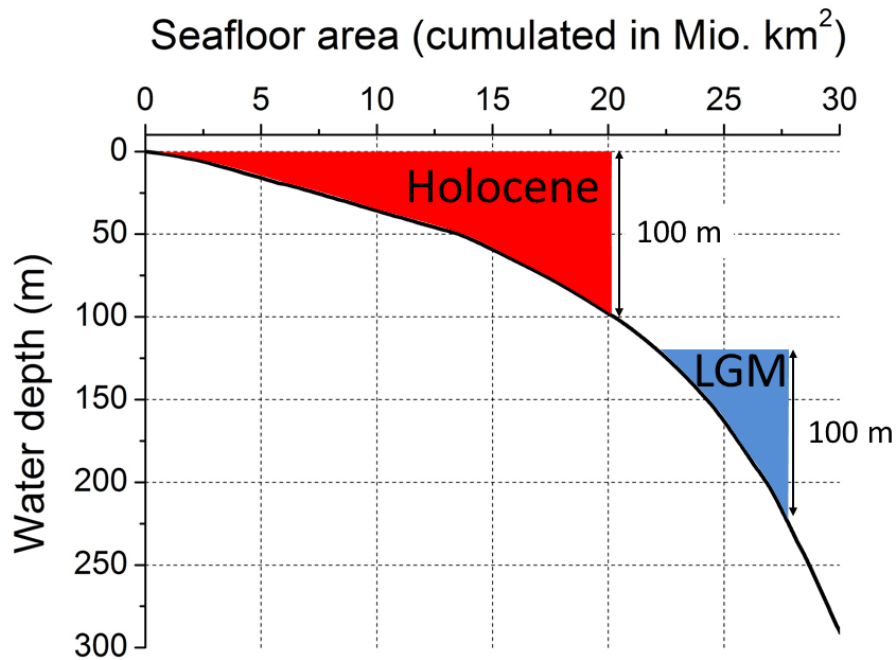
2

3 Table C4. LGM tracer concentrations in model boxes at 21 ka in simulation STD (see Tab.

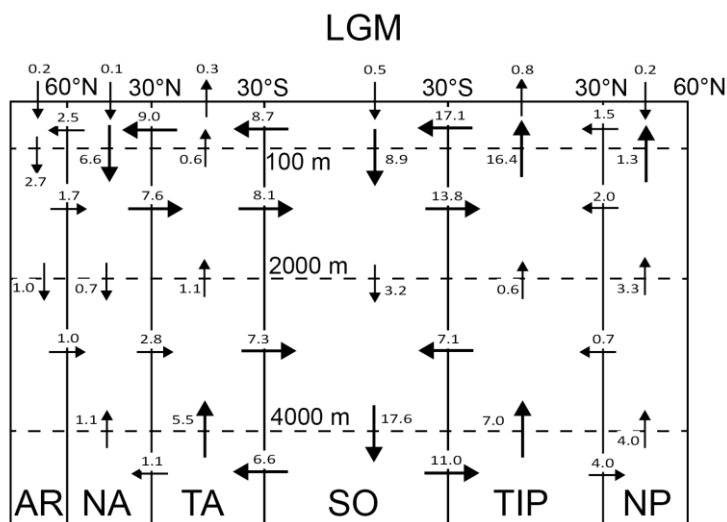
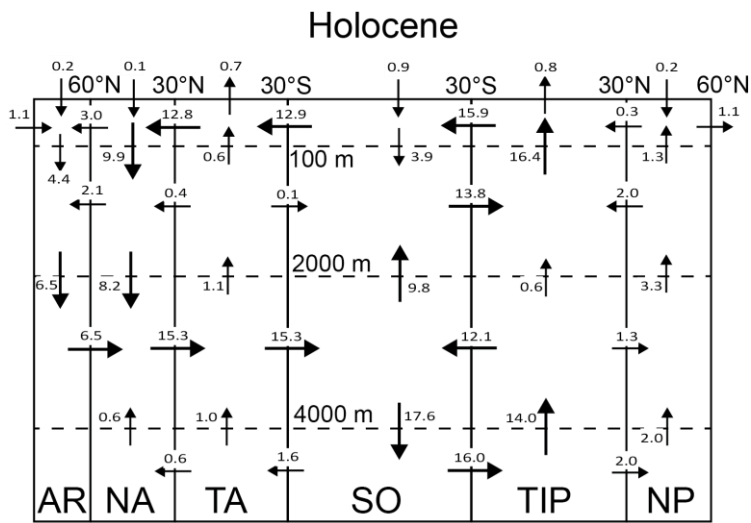
4 A1 and A2 for further information)

Box	Sal (PSU)	PO ₄ (μM)	NO ₃ (μM)	O ₂ (μM)	DIC (μM)	TA (μM)	δ ¹³ C (‰)	ΔΔ ¹⁴ C (‰)
AR _S	33.69	0.93	12.2	369	2244	2562	1.63	-181
NA _S	35.84	0.34	4.2	266	2158	2619	2.56	-156
TA _S	36.94	0.14	1.7	214	2122	2685	2.90	-119
SO _S	35.80	0.42	6.0	306	2184	2588	2.38	-148
TIP _S	36.40	0.36	4.1	211	2040	2583	2.51	-128
NP _S	34.87	0.79	10.9	282	2131	2521	2.43	-145
AR _I	35.48	1.07	14.8	330	2268	2579	1.39	-192
NA _I	35.69	1.12	16.4	258	2277	2595	1.32	-192
TA _I	35.72	1.60	23.2	212	2345	2601	0.71	-224
SO _I	35.86	2.09	32.3	143	2419	2583	-0.13	-213
TIP _I	35.94	2.35	35.5	76	2444	2591	-0.38	-223
NP _I	35.72	2.97	42.1	69	2537	2631	-0.96	-300
AR _D	35.54	1.45	19.4	282	2315	2587	0.96	-221
NA _D	35.59	1.70	22.5	251	2346	2593	0.69	-239
TA _D	35.72	2.16	29.2	201	2422	2621	0.11	-281
SO _D	35.80	2.81	36.9	179	2518	2649	-0.60	-312
TIP _D	35.81	3.16	40.4	112	2576	2690	-0.83	-342
NP _D	35.79	3.12	40.6	108	2574	2691	-0.86	-356
AR _B	35.54	1.48	19.7	280	2317	2587	0.94	-222
NA _B	35.65	2.04	26.4	222	2392	2607	0.32	-266
TA _B	35.74	2.37	31.5	193	2453	2631	-0.11	-294
SO _B	35.80	2.84	37.1	174	2523	2654	-0.61	-315
TIP _B	35.81	3.06	39.0	135	2565	2694	-0.74	-334
NP _B	35.79	3.11	40.0	118	2574	2698	-0.81	-353

5



1
 2 Figure 1. Morphology of global ocean margin. The black line is the cumulated seafloor area
 3 as derived from the high-resolution ETOPE 1 grid (Eakins and Sharman, 2012). The ocean
 4 margin at 0 – 100 m water depth is indicated for the modern ocean (red area) and for the LGM
 5 when eustatic sea-level was lowered by 120 m (blue area). The global ocean retreated into
 6 steeper terrain during the glacial marine regression. The seafloor areas covered by shallow
 7 waters were reduced by this steepening of ocean margins.
 8



1

2 Figure 2. Set-up of the box model: The global ocean is separated into 24 boxes representing

3 surface (0 – 100 m), intermediate (100 - 2000 m), deep (2000 – 4000 m), and bottom (>4000

4 m) waters in the Arctic (AR), North Atlantic (NA), Tropical Atlantic (TA), Southern Ocean

5 (SO), Tropical Indo-Pacific (TIP), and North Pacific (NP) . Arrows with numbers indicate net

6 water fluxes between boxes in Sv; major fluxes (>5 Sv) are represented by large arrows,

7 minor fluxes (<5 Sv) by small arrows. Arrows crossing the top boundary of the surface water

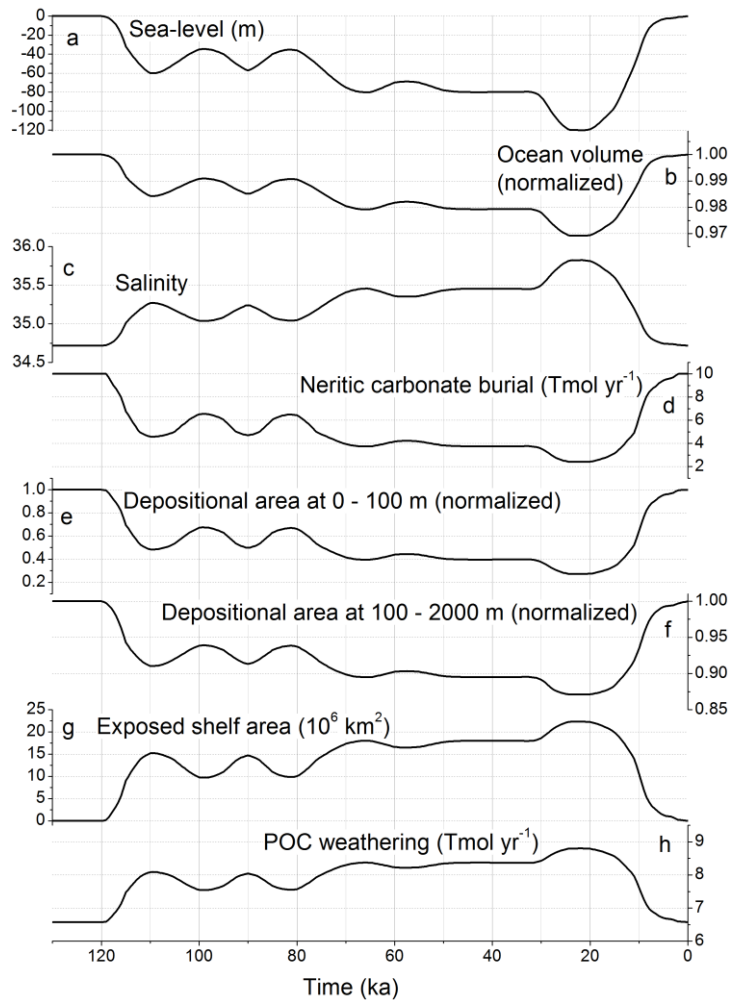
8 boxes (seawater-atmosphere interface) indicate net freshwater fluxes (precipitation + river

9 water fluxes - evaporation). The upper panel shows the circulation field applied for the

10 modern ocean and the previous interglacial, the lower panel shows the circulation applied

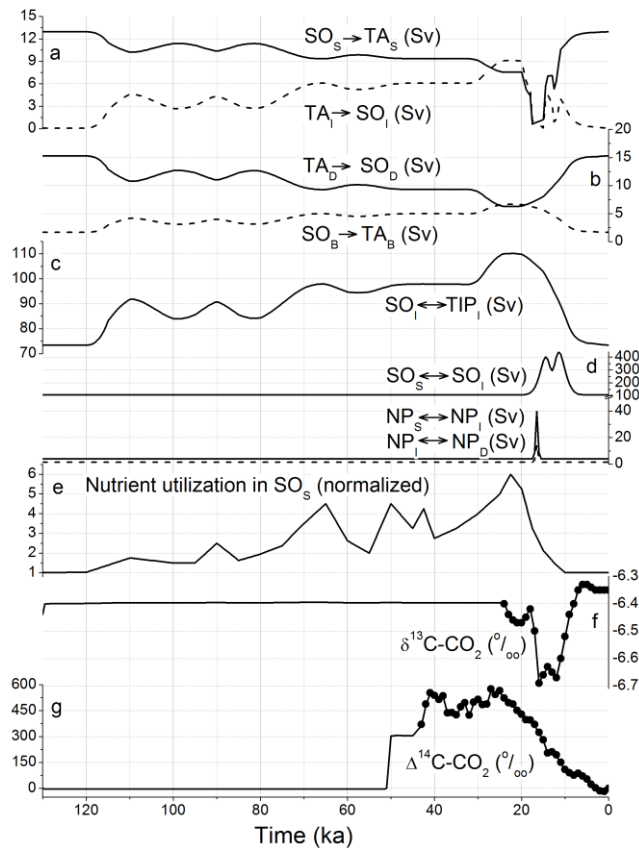
11 over the LGM.

1



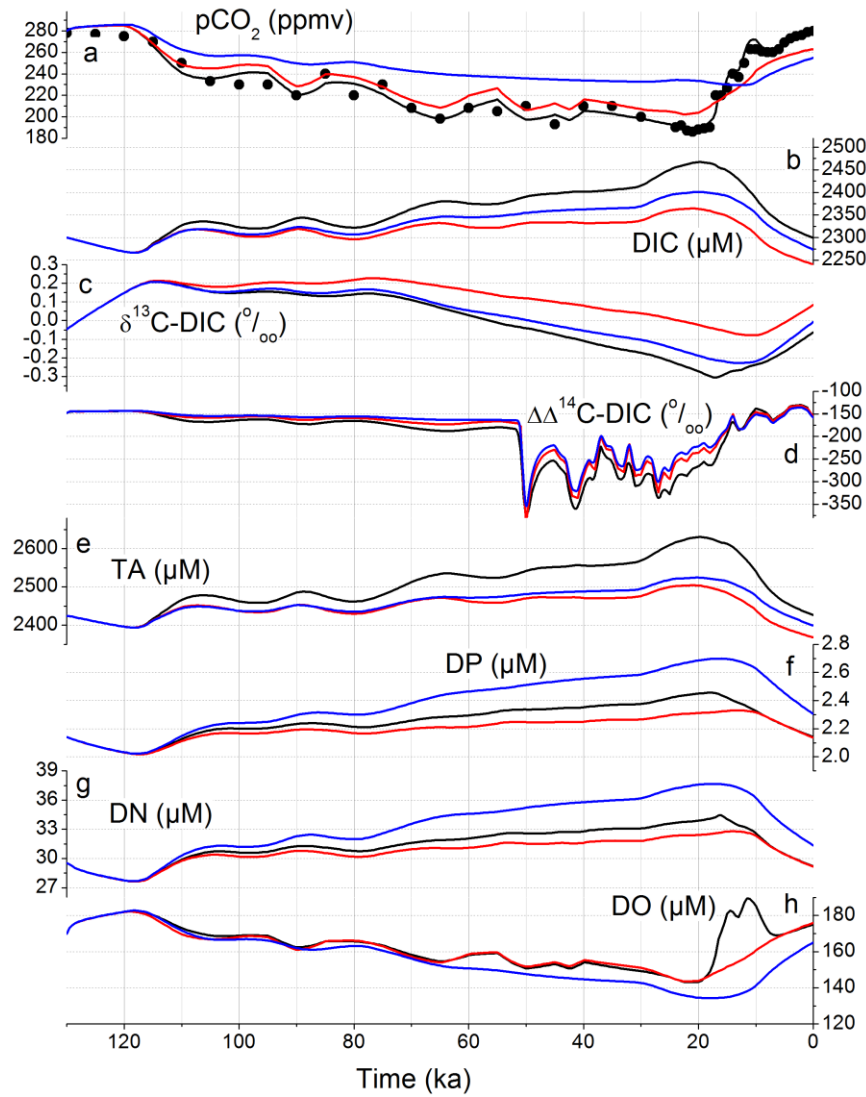
2

3 Figure 3. Model forcing related to sea-level change. (a) Eustatic sea-level (Waelbroeck et al.,
4 2002; Stanford et al., 2011); (b) Global ocean volume as calculated from eustatic sea-level
5 and ocean bathymetry data (Eakins and Sharman, 2012); (c) Salinity of global mean seawater
6 as calculated from global ocean volume; (d) Global burial rate of neritic carbonate as
7 calculated from seafloor area at 0 – 50 m water depth (Kleypas, 1997; Wallmann, 2014); (e-f)
8 Seafloor area at 0 – 100 m and 100 -2000 m water depth calculated from sea-level and ocean
9 bathymetry data (Eakins and Sharman, 2012); (g) Exposed shelf area calculated from sea-
10 level and ocean bathymetry data (Eakins and Sharman, 2012); (h) Global rate of POC
11 weathering calculated from exposed shelf area (Wallmann, 2014).

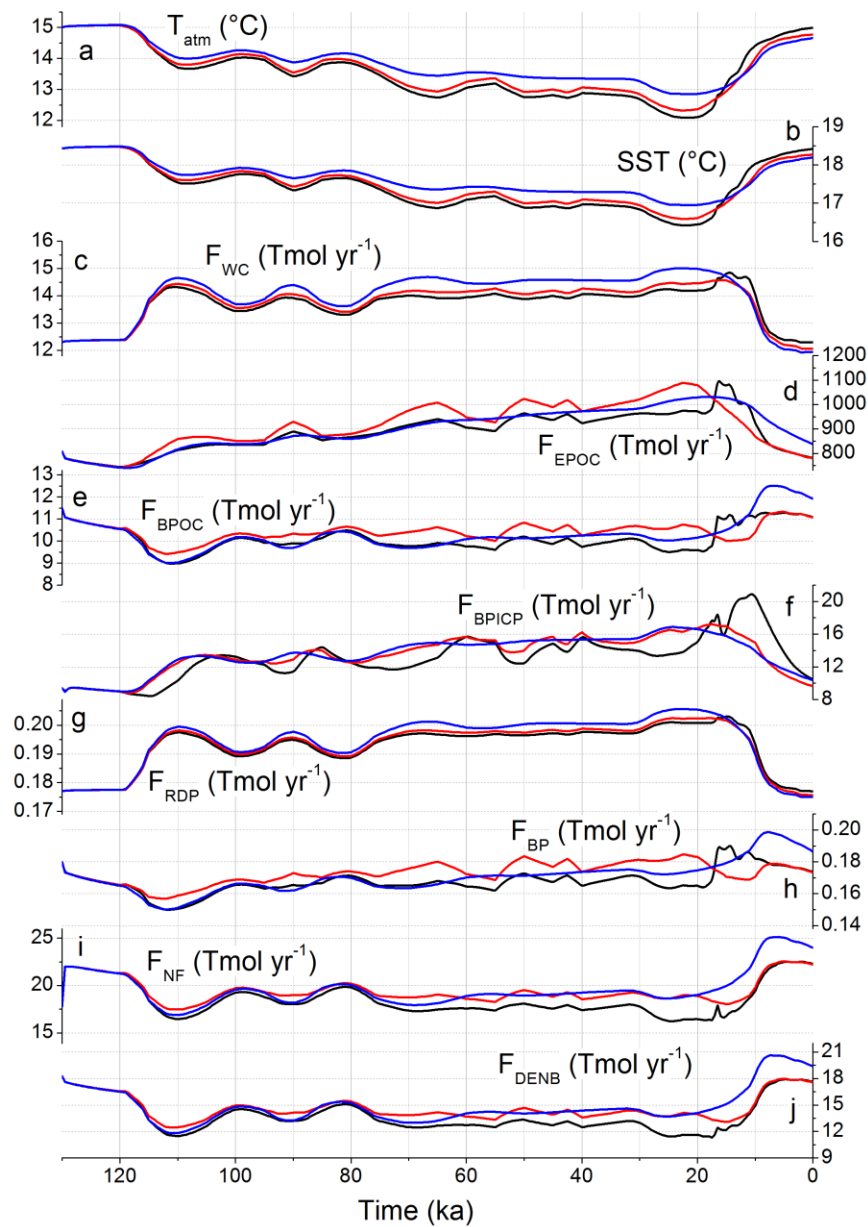


1

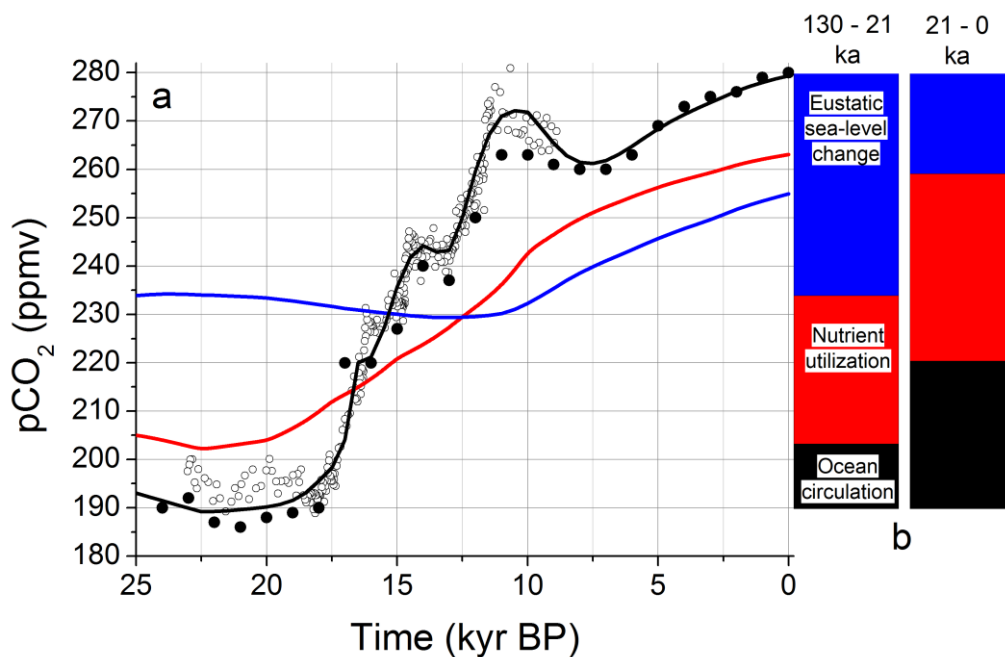
2 Figure 4. Model forcing applied to define ocean circulation, nutrient utilization in the
 3 Southern Ocean, and the isotopic composition of atmospheric CO₂. (a-b) Net water fluxes
 4 between Southern Ocean (SO) and Tropical Atlantic (TA). The horizontal flows are given for
 5 (from top to bottom) surface water (subscript S), intermediate water (subscript I), deep water
 6 (subscript D), and bottom water (subscript B); c) Horizontal exchange flux between Southern
 7 Ocean and Tropical Indo-Pacific intermediate waters ; d) Vertical water exchange fluxes in
 8 the Southern Ocean and North Pacific across 100 m water depth (solid lines) and 2000 m
 9 water depth (broken line); (e) Nutrient utilization in the Southern Ocean (Martinez-Garcia et
 10 al., 2014); f) δ¹³C value of atmospheric CO₂. Dots indicate ice-core data (Schmitt et al., 2012)
 11 while the solid line defines the values applied in the model. For >24 kyr BP, where data are
 12 not available, the δ¹³C-CO₂ value is set to -6.4 ‰; (g) Δ¹⁴C value of atmospheric CO₂, dots
 13 indicate values reconstructed from the geological record (Reimer et al., 2013) while the solid
 14 line defines the values applied in the model. For >50 kyr BP, where data are not available, the
 15 atmospheric Δ¹⁴C-CO₂ is assumed to correspond to the pre-anthropogenic modern value (0
 16 ‰).



1
 2 Figure 5. Model results for the standard case (simulation STD, black lines), for constant
 3 circulation (simulation STD-CC, red lines), and constant circulation and nutrient utilization
 4 (simulation STD-CC-CN, blues lines). (a) Atmospheric pCO₂, dots indicate ice core data
 5 (Monnin et al., 2001; Petit et al., 1999; Monnin et al., 2004); (b) - (h) Global mean seawater
 6 concentrations and isotopic compositions (b) Dissolved inorganic carbon (DIC); (c) δ¹³C of
 7 DIC; (d) Difference between radiocarbon in seawater DIC and atmospheric CO₂ ($\Delta\Delta^{14}\text{C-DIC}$
 8 = $\Delta^{14}\text{C-DIC} - \Delta^{14}\text{C-CO}_2$); (e) Total alkalinity (TA); (f) Dissolved phosphorus (DP); (g)
 9 Dissolved reactive nitrogen (DN); (h) Dissolved oxygen (DO).



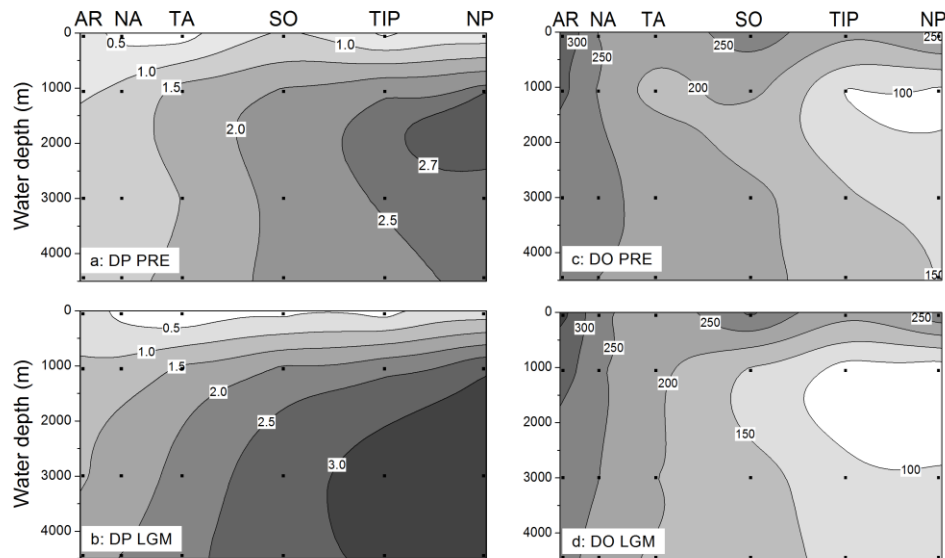
1
 2 Figure 6. Model results for simulations STD (black lines), STD-CC (red lines), and STD-CC-
 3 CN (blue lines). (a) Global mean atmospheric near-surface temperature (T_{atm}); (b) Global
 4 mean sea surface temperature (SST); (c) – (j) Global rates; (c) Carbonate weathering (F_{WC});
 5 (d) Marine export production of POC (F_{EPOC}); (e) POC burial (F_{BPOC}); (f) Burial of pelagic
 6 carbonate (F_{BPICP}); (g) Riverine flux of dissolved phosphorus (F_{RDP}); (h) Burial of marine
 7 phosphorus (F_{BP}); (i) Nitrogen fixation (F_{NF}); (j) Benthic denitrification (F_{DENB}).



1
2 Figure 7. Atmospheric pCO₂ over the last 25 kyr. (a) Model results for simulations STD
3 (black line), STD-CC (red line), and STD-CC-CN (blues line); solid dots indicate ice core
4 data by (Monnin et al., 2004; Monnin et al., 2001) while ice core data reported in (Marcott et
5 al., 2014) are shown as open circles; (b) relative contribution of sea-level change (blue),
6 nutrient utilization (red), and ocean circulation changes (black) to pCO₂ model results; the left
7 hand column shows contributions to the glacial pCO₂ draw-down (51 % induced by sea-level
8 fall, 34 % by enhanced nutrient utilization, 15 % by changes in ocean circulation); the right
9 hand column indicates the driving forces for the deglacial pCO₂ rise (23 % induced by sea-
10 level rise, 43 % by decrease in nutrient utilization, 34 % by changes in ocean circulation).

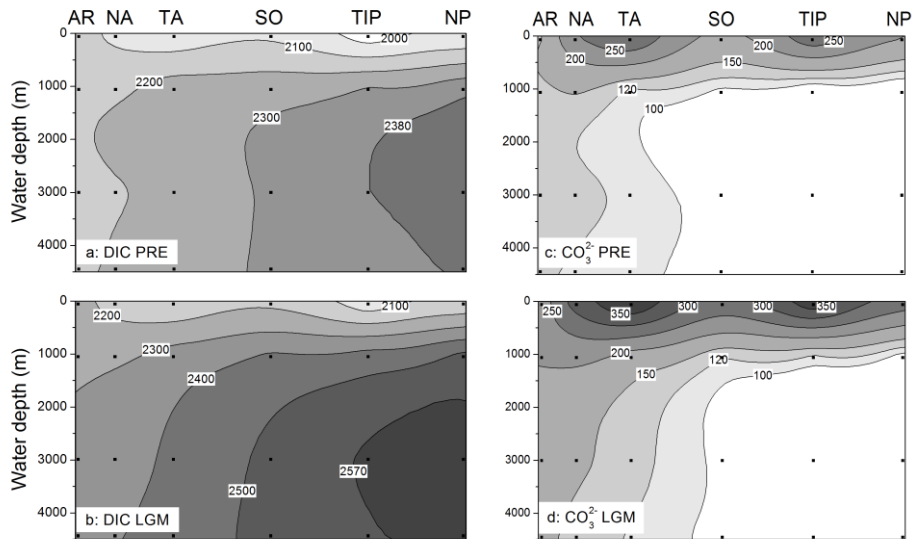
11

12

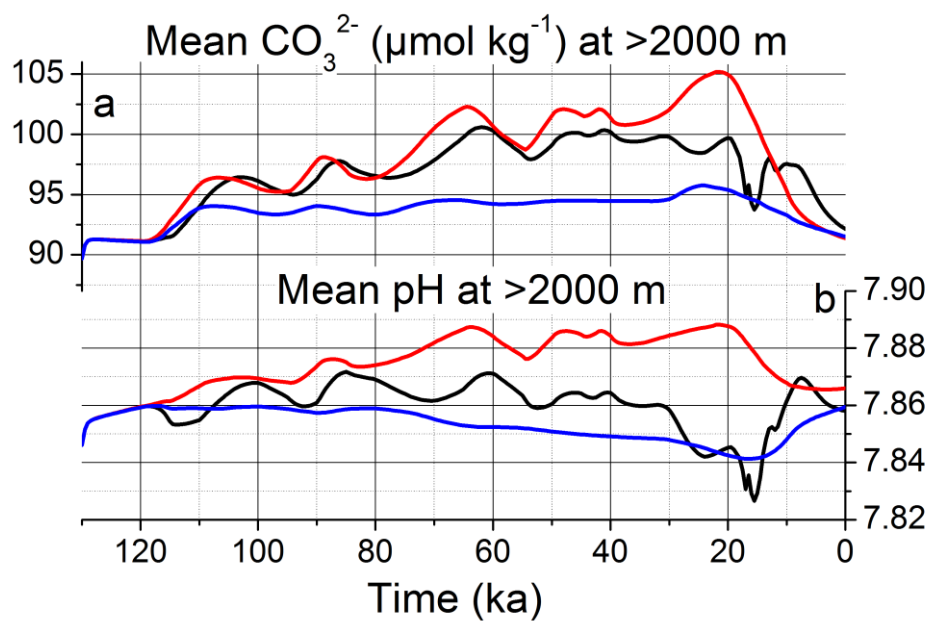


1
 2 Figure 8. Concentrations (in μM) of dissolved phosphorus (DP) and oxygen (DO) in the pre-
 3 anthropogenic modern ocean (PRE, model results for 0 ka, a: DP, c: DO) and during the LGM
 4 (model results for 21 ka, b: DP, d: DO, Tab. C4). The contour plots shown here and in Figures
 5 9 and 11 are based on concentrations calculated in simulation STD for each of the 24 ocean
 6 boxes (indicated as grid points).

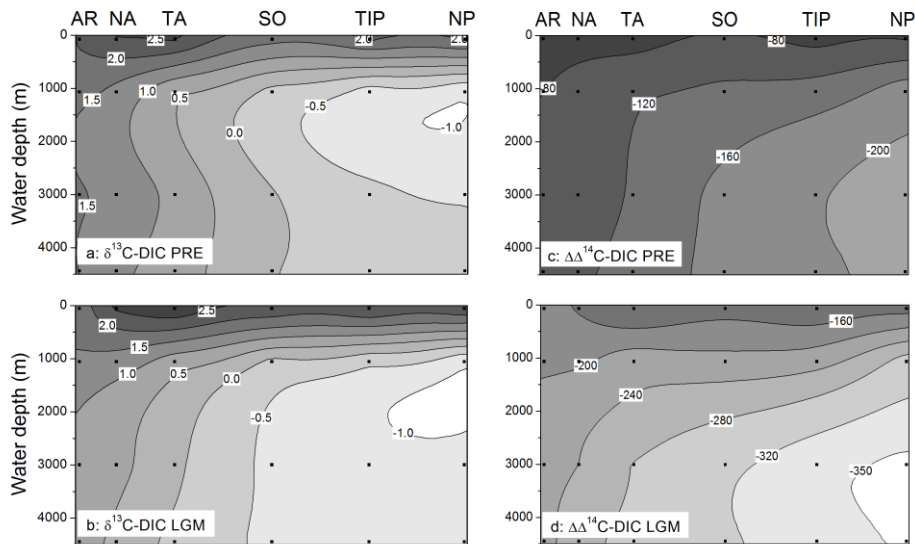
7
 8



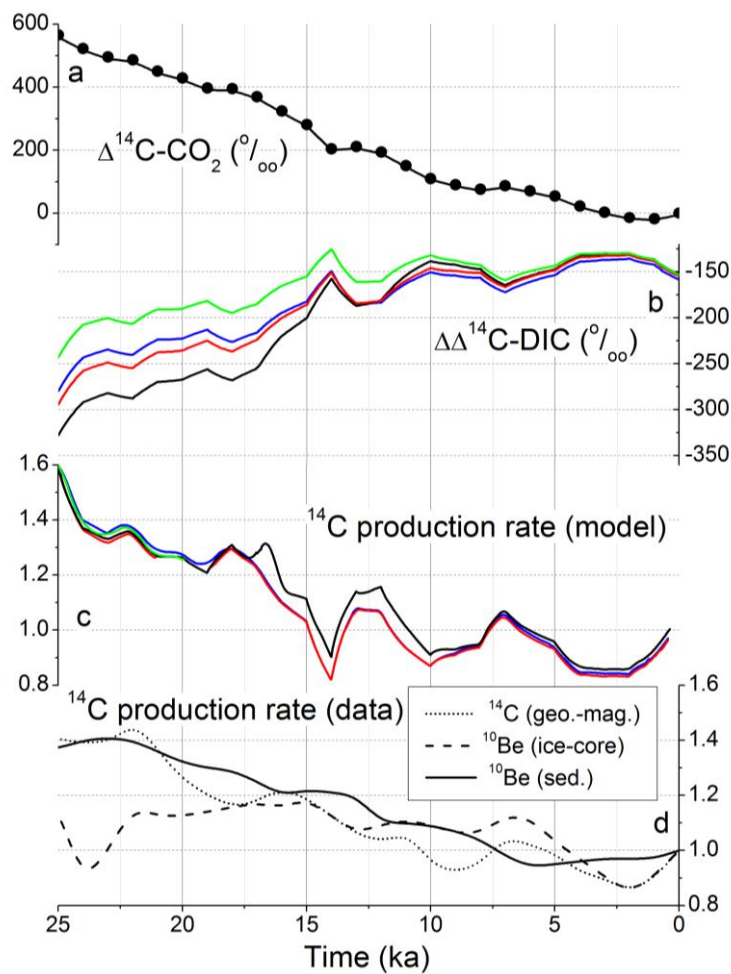
1
 2 Figure 9. Concentrations of dissolved inorganic carbon (DIC in μM) and carbonate ions
 3 (CO_3^{2-} in $\mu\text{mol kg}^{-1}$) in the pre-anthropogenic modern ocean (PRE, model results for 0 ka, a:
 4 DIC, c: CO_3^{2-}) and during the LGM (model results for 21 ka, b: DIC, d: CO_3^{2-} , Tab. C4). See
 5 legend of Fig. 8 for further information.
 6



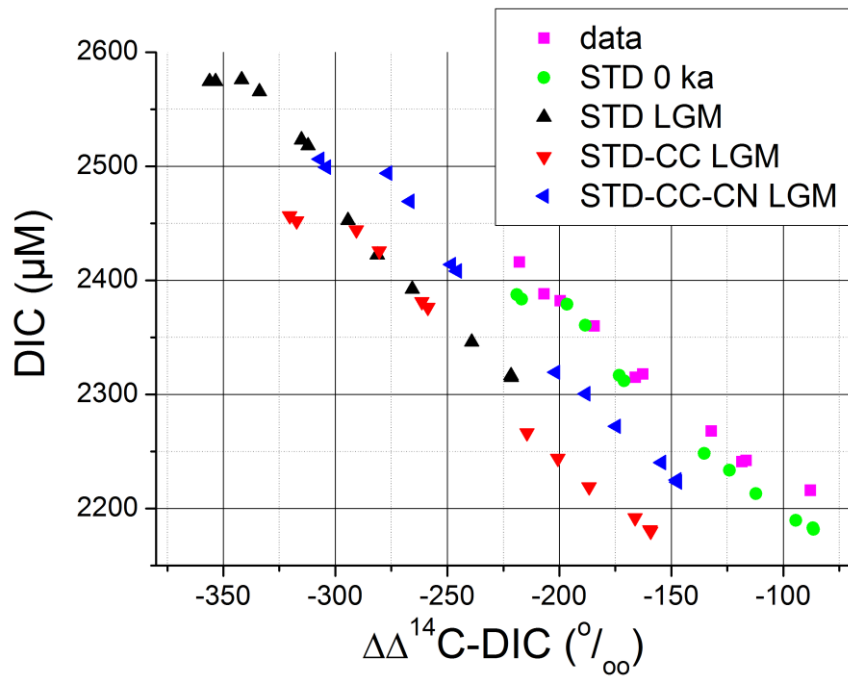
1
 2 Figure 10. Global mean carbonate ion concentrations (a) and pH values (b) below 2000 m
 3 water depth for simulations STD (black line), STD-CC (red line), and STD-CC-CN (blues
 4 line).
 5



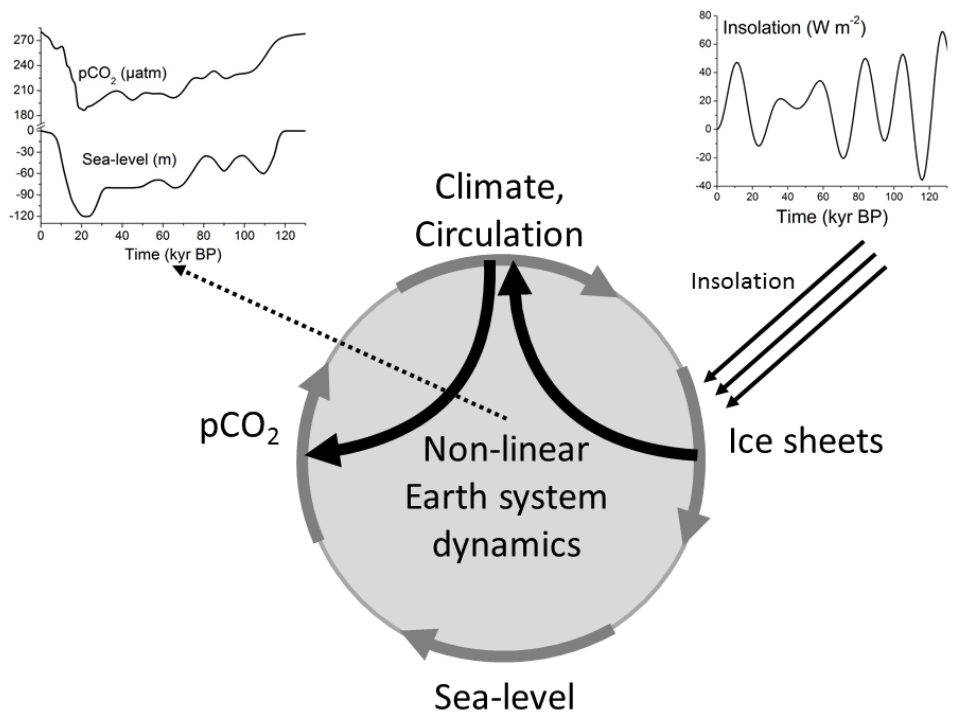
1
 2 Figure 11. Isotopic composition of dissolved inorganic carbon (DIC) in the global ocean. $\delta^{13}\text{C}$
 3 of dissolved inorganic carbon ($\delta^{13}\text{C-DIC}$ in ‰) and radiocarbon composition of dissolved
 4 inorganic carbon ($\Delta\Delta^{14}\text{C-DIC}$ in ‰) in the pre-anthropogenic modern ocean (PRE, model
 5 results for 0 ka, a: $\delta^{13}\text{C-DIC}$, c: $\Delta\Delta^{14}\text{C-DIC}$) and during the LGM (model results for 21 ka, b:
 6 $\delta^{13}\text{C-DIC}$, d: $\Delta\Delta^{14}\text{C-DIC}$, Tab. C4). $\Delta\Delta^{14}\text{C-DIC}$ values represent the difference between the
 7 atmospheric value (0 ‰ for the pre- anthropogenic modern atmosphere, +446 ‰ for the
 8 LGM atmosphere) and seawater $\Delta^{14}\text{C-DIC}$. See legend of Fig. 8 for further information.
 9



1
 2 Figure 12. Radiocarbon values and production rates. (a) Atmospheric $\Delta^{14}\text{C-CO}_2$; dots are
 3 IntCal13 data (Reimer et al., 2013) while the black line shows the values applied in the model
 4 runs, (b) Marine $\Delta\Delta^{14}\text{C-DIC}$ values calculated as difference between radiocarbon in seawater
 5 DIC and atmospheric CO_2 . The results of simulations STD-CC-CN, STD-CC, and STD are
 6 indicated as blue, red and black lines, respectively. The green line indicates the results
 7 obtained in a steady-state simulation under Holocene boundary conditions where all variables
 8 except atmospheric $\Delta^{14}\text{C-CO}_2$ and radiocarbon production rate were kept constant over
 9 time.(c) Production rates of radiocarbon in the atmosphere calculated in the model runs and
 10 normalized to the pre- anthropogenic modern value ($1.64 \text{ atoms cm}^2 \text{ s}^{-1}$); (d) ^{14}C production
 11 rates calculated from the geo-magnetic record (Laj et al., 2002), ^{10}Be production rate as
 12 reconstructed from Greenland ice core data (Muscheler et al., 2005; Reimer et al., 2013), ^{10}Be
 13 production rate as reconstructed from sediment data (Frank et al., 1997); all rates are
 14 normalized to their pre- anthropogenic modern values

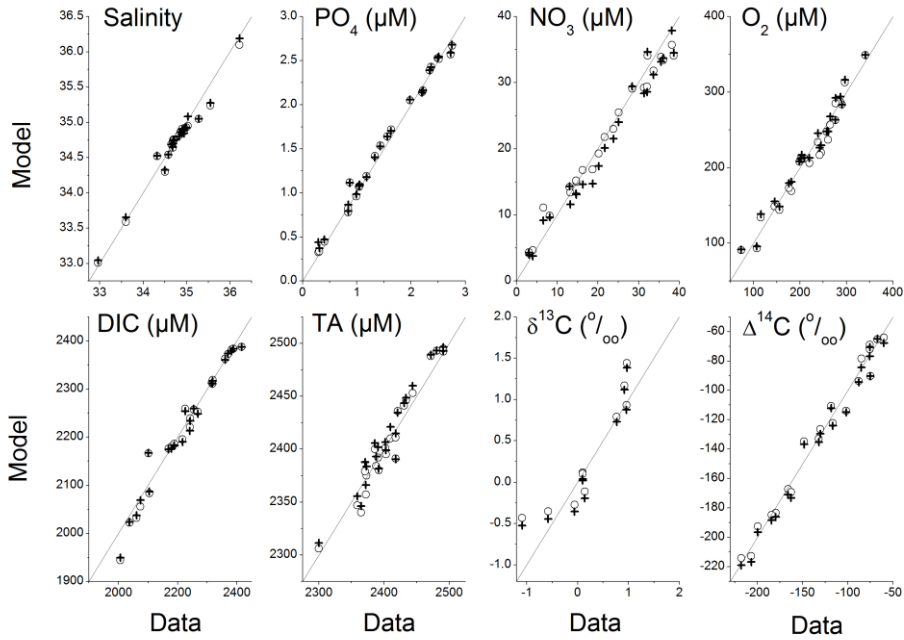


1
 2 Figure 13. DIC versus difference between radiocarbon in seawater DIC and atmospheric CO₂
 3 (ΔΔ¹⁴C-DIC) at >2000 m water depth. Data are mean values for deep water and bottom water
 4 boxes derived from water column measurements. Model results are shown for the standard
 5 case (STD), for constant circulation (STD-CC), and constant values for circulation and
 6 nutrient utilization (STD-CC-CN). LGM refers to model results at 21 kyr BP.
 7



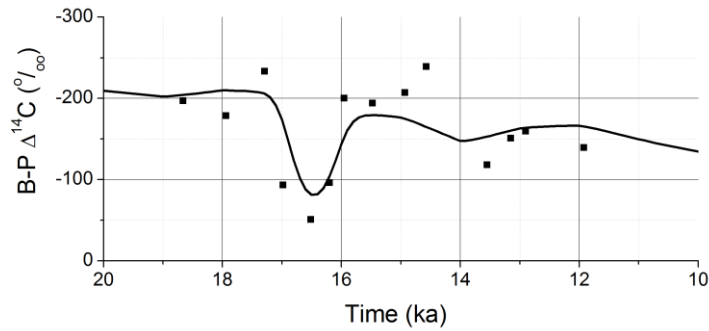
1
2
3
4
5
6
7
8
9
10
11
12
13
14
15

Fig. 14. Key elements of the 100 kyr cycle. Summer insolation at high northern latitudes (June insolation at 60°N, diagram in the upper right corner, (Berger and Loutre, 1991)) affects the growth and melting of continental ice sheets and thereby eustatic sea-level change. The glacial draw-down of atmospheric pCO₂ and its deglacial rise are supported by sea-level change. The cycle is closed by atmospheric pCO₂ affecting global climate and thereby the volume of continental ice sheets. It is accelerated and further strengthened by additional positive feedbacks: Ice sheets affect the Earth's albedo and climate while changes in ocean and atmosphere circulation support the glacial pCO₂ draw-down and are largely responsible for the rapid deglacial rise in atmospheric pCO₂. The records of atmospheric pCO₂ and eustatic sea-level change (diagrams in the upper left corner, (Monnin et al., 2001; Petit et al., 1999; Monnin et al., 2004; Waelbroeck et al., 2002; Stanford et al., 2011) reflect the internal non-linear dynamics of the Earth system and its response to external insolation forcing.



1
2 Fig. A1. Tracer concentrations in ocean boxes: Model versus data. Open circles indicate
3 concentrations applied as initial values at 130 ka (Tab. A1 and A2). Crosses are
4 concentrations obtained at the end of simulation STD at 0 ka after the completion of a full
5 glacial cycle. Lines indicate the 1:1 relationship, e.g. the best fit to the data. $\delta^{13}\text{C}$ data at
6 <2000 m water depth are excluded from the model-data comparison since they are affected by
7 anthropogenic CO_2 .

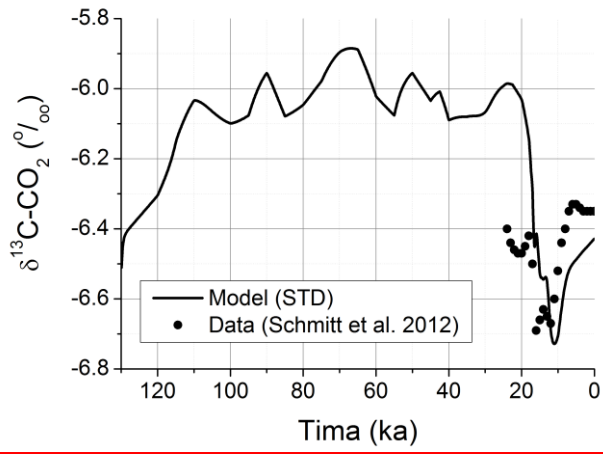
8



1
 2 Fig. A2. Deglacial benthic – pelagic radiocarbon record in the North Pacific: Model (line)
 3 versus data (squares). The $\Delta^{14}\text{C}$ -DIC difference between deep water and surface water boxes
 4 in the North Pacific is compared to data ($\Delta^{14}\text{C}$ difference between benthic and pelagic
 5 foraminifera, B-P $\Delta^{14}\text{C}$) from core MD02-2489 taken at the Alaskan Margin at 3.6 km water
 6 depth (Rae et al., 2014). The vertical mixing across 100 m and 2000 m water depth was
 7 enhanced by a factor of 10 at 16.5 ka (Fig. 4d) to reproduce the radiocarbon data.

8
 9

1



2

3 Fig. A3: Stable carbon isotopic composition of atmospheric CO₂. Model results versus ice-
4 core data (Schmitt et al., 2012). The model results were obtained in the standard simulation
5 STD without any tuning of the ¹³C-CO₂ fluxes across the seawater-atmosphere interface.

6